Investigation of the CP properties of VBF Higgs production in hadronic final states of $H \rightarrow \tau\tau$ decays with the ATLAS detector

Dissertation

zur Erlangung des mathematisch-naturwissenschaftlichen
Doktorgrades
„Doctor of Philosophy“
der Georg-August-Universität Göttingen

im Promotionsstudiengang Physik
der Georg-August University School of Science (GAUSS)

vorgelegt von

Serhat Ördek

aus Celle

Göttingen, 2021

Betreuungsausschuss

Prof. Dr. Stanley Lai
Prof. Dr. Steffen Schumann
Prof. Dr. Ariane Frey

Mitglieder der Prüfungskommission:

Referent:	Prof. Dr. Stanley Lai II. Physikalisches Institut, Georg-August-Universität Göttingen
Koreferent:	Prof. Dr. Arnulf Quadt II. Physikalisches Institut, Georg-August-Universität Göttingen

Weitere Mitglieder der Prüfungskommission:

Prof. Dr. Ariane Frey
II. Physikalisches Institut, Georg-August-Universität Göttingen

Prof. Dr. Jens Niemeyer
Institut für Astrophysik, Georg-August-Universität Göttingen

Prof. Dr. Karl-Henning Rehren
Institut für Theoretische Physik, Georg-August-Universität Göttingen

Prof. Dr. Steffen Schumann
Institut für Theoretische Physik, Georg-August-Universität Göttingen

Tag der mündlichen Prüfung: 28.01.2021

Referenz: II.Physik-UniGö-Diss-2021/01

Investigation of the CP properties of VBF Higgs production in hadronic final states of $H \rightarrow \tau\tau$ decays with the ATLAS detector

Abstract

A test of CP invariance of the VBF Higgs production process is presented in the $\tau\tau$ final state. For this, a profile likelihood fit using a matrix-element observable method is employed to test whether a CP-odd component is present in the coupling. The analysis is carried out using 36.1 fb^{-1} of proton-proton collision data recorded at a centre-of-mass energy of 13 TeV with the ATLAS detector at the LHC. It constrains the value of the CP violation inducing parameter $\tilde{d}$ to $[-0.090, 0.035]$ at the 68% confidence level. This result is compatible with the Standard Model expectation of $\tilde{d} = 0$ and no CP violation. Particular emphasis is put on the final state including two hadronically-decaying τ leptons.

Additionally, a measurement of the efficiencies of τ-lepton triggers is presented. These triggers are necessary to collect the data on which the measurement of $\tilde{d}$ is based. Lastly, an ongoing measurement of Higgs-boson production cross-sections in the $\tau\tau$ final state using 139 fb^{-1} of data is discussed, including an improved method of estimating background contributions in the final state with two hadronically-decaying τ leptons.

Contents

CHAPTER 1

Introduction

The Higgs boson was the last particle in the Standard Model (SM) to be discovered experimentally, which happened in 2012 [1, 2]. With this, all SM particles have been discovered, and the focus of the ATLAS physics program is shifted towards understanding the shortcomings of the SM. One of these shortcomings is the extent of baryon-antibaryon asymmetry predicted by the SM, which is too low to explain the observed asymmetry [3–7]. One of the Sakharov conditions for producing such an asymmetry is the presence of processes that are not invariant under charge conjugation (C) and its combination with parity (CP) [8]. This strongly suggests the presence of CP-violating processes that are not part of the SM.

As the only CP-violating SM process, the quark mixing [9, 10] and weak decay, is in the electroweak sector, it is natural to probe other electroweak processes as well. For this reason, this thesis focuses on an analysis that probes the Higgs boson couplings to electroweak bosons (HVV couplings) for CP-odd contributions, using $H \to \tau\tau$ events [11]. To that end, the analysis is restricted to events with two jets, which enhances the contribution of vector-boson fusion (VBF) Higgs production events, featuring the desired HVV vertex.

The other analysis covered in this thesis is the measurement of Higgs-boson Simplified Template Cross-Sections (STXS), the standardized cross-section measurement strategy in all Higgs decay channels within the ATLAS collaboration. The STXS framework was devised in order to effectively decorrelate deviations of Higgs-boson production cross-sections from the SM prediction in different phase-space regions. This allows to compare predictions from different beyond-Standard-Model (BSM) theories to experimental results in a more straightforward way.

The thesis is ordered as follows. Chapter 2 summarizes the theoretical concepts behind the Standard Model of particle physics, while Chapter 3 describes which aspects of it are investigated throughout the thesis. Chapter 4 gives an overview of the experimental setup at CERN that makes all the presented studies possible. In Chapter 5, the methods employed to reconstruct particles and other objects from charge and energy deposits in the detector are described. The efficiency measurement of τ-lepton triggers will be discussed in Chapter 6. This measurement is one of the pre-requisites for conducting a test of CP violation (CPV) in fully hadronic final states of VBF $H \to \tau\tau$ events, which is the topic of Chapter 7. Chapter 8 covers the ongoing efforts to improve the background estimation in fully hadronic $H \to \tau\tau$ events using the full ATLAS dataset recorded from 2015 to 2018. Finally, Chapter 9 gives an outlook for future direct measurements of CPV in Higgs-boson couplings.

CHAPTER 2

The Standard Model

The Standard Model of particle physics represents our current understanding of elementary particles and their interactions. It is known to be incomplete, as it makes no statement on the gravitational force and is missing a dark matter candidate, but it has been very successful in predicting phenomena that were later experimentally observed with very high precision. This chapter gives an overview of the structure and mathematical foundations of the SM, as well as the phenomenological implications these have for the Higgs boson and the τ lepton, the two particle types that are covered most thoroughly in this thesis.

2.1 Gauge Symmetries

Mathematically, the SM [12–14] is a quantum field theory (QFT) which characterizes matter with fermionic spin-1/2 spinor fields and interactions with integer-spin bosonic fields. The physical particles arise from excitations of these fields. The starting point for a QFT is the Lagrangian $\mathcal{L}$ of the model, which is constructed by calculating the difference between kinetic energy T and potential energy V:

$$\mathcal{L} = T - V \ .$$

By integrating $\mathcal{L}$ over time, the action is constructed. This quantity is used to derive equations of motion for the fields by applying the variation principle. In particle physics, this allows to examine the kinematic properties of particles and their interactions by deriving Feynman rules.

This section introduces the different components of the SM Lagrangian and how gauge symmetries can be utilized to construct models of interacting particles starting from a sterile theory.

2.1.1 Electroweak theory

The Lagrange density $\mathcal{L}$ of a free spin-1/2 particle $\psi(x)$ with mass m is:

$$\mathcal{L} = \bar{\psi}\left(i\gamma^\mu\partial_\mu - m\right)\psi \tag{2.1}$$

with the Dirac matrices γ^μ where $\mu \in \{0,1,2,3\}$ and the Einstein summation is applied, i. e. repeated indices are always summed over. This theory only contains a single type of fermion with mass m that does not partake in any interactions.

A convenient way to introduce interactions to this theory is to require the Lagrangian to be invariant under a group of transformations of ψ, called gauge transformations. It is easily verified that $\mathcal{L}$ is already symmetric under global $U(1)$ gauge transformations, meaning that $\psi \to e^{-ig'C}\psi$ will not change the value of $\mathcal{L}$, for any $C \in \mathbb{R}$ and the coupling constant $g' > 0$. However, making C dependent on the space-time coordinate x, also called promoting the global gauge transformation into a local one, breaks this symmetry:

$$\mathcal{L}(e^{-ig'C(x)}\psi) = \mathcal{L}(\psi) + g'\bar{\psi}\gamma^\mu\psi\partial_\mu C(x)\ .$$

To recover the $U(1)$ symmetry, an additional field B_μ, called a gauge field, is introduced to the theory. This field is chosen to transform as

$$B_\mu(x) \to B_\mu(x) + \partial_\mu C(x)\ .$$

under the gauge transformation to restore the symmetry.

This field enters the Lagrangian by expanding the partial derivative ∂_μ, to construct the covariant derivative

$$D_\mu = \partial_\mu + ig'B_\mu\ .$$

With this, the expanded Lagrangian has regained its $U(1)$ symmetry, since the derivatives in $C(x)$ cancel when transforming ψ and B_μ simultaneously. This time, however, it is a local symmetry. To achieve this, a term of the form $\bar{\psi}\gamma^\mu B_\mu\psi$ had to be introduced to the theory, meaning that the fermion ψ can interact with the gauge boson B. But for B_μ to be a realistic field, it needs to have a free dynamic term. This term takes the form $F_{\mu\nu}F^{\mu\nu}$ with $F_{\mu\nu} = \partial_\mu B_\nu - \partial_\nu B_\mu$.
Applying the variation principle to the thus constructed Lagrangian reproduces

the Maxwell equations. The $U(1)$ symmetric model containing one fermion can therefore be interpreted as the quantum theory of electrodynamics.

This procedure can be generalized to other symmetry groups, such as $SU(2)$. In this case, the object ψ in Eq. (2.1) is reinterpreted as a doublet of two fermion fields of the same mass m, which is equivalent to adding the free Lagrangians of two fermion fields. The main differences compared to the $U(1)$ case are that $SU(2)$ has more than one generator, and that it is a non-Abelian group. Since it has three generators, the covariant derivative contains more terms and more gauge fields, one for each generator:

$$(D_\mu \psi)_i = \partial_\mu \psi_i - i(g W_\mu^a T^a)_{ij} \psi_j \ . \tag{2.2}$$

Here, $g > 0$ is the coupling constant of the $SU(2)$ group, W_μ^a are three gauge fields ($a \in \{1, 2, 3\}$) and $T^a = \frac{1}{2}\sigma^a$ with the Pauli matrices σ^a, which are the generators of $SU(2)$. The dynamic terms of each gauge field W^a again take the form $F_{\mu\nu}^a F^{\mu\nu,a}$, but due to the group being non-Abelian, the tensor $F_{\mu\nu}^a$ has an additional term:

$$F_{\mu\nu}^a = \partial_\mu W_\nu^a - \partial_\nu W_\mu^a + g \epsilon_{abc} W_\mu^b W_\nu^c \ . \tag{2.3}$$

The last term contains the Levi-Civita tensor ϵ_{abc} because these are the structure constants of $SU(2)$. It leads to the presence of terms of higher than quadratic order in the gauge fields, which represent interactions of the gauge fields among each other.

This $SU(2)$ theory describes the weak nuclear interaction, albeit with a few caveats. The described theory alone cannot account for the observed non-zero masses of the three corresponding gauge bosons W^-, Z and W^+. Also, the two components of the ψ doublet cannot have different masses, unlike the known $SU(2)$ doublets. The procedure to mitigate these inconsistencies in modern theories is discussed in Sec. 2.2.

2.1.2 QCD

Reusing this procedure with the gauge group $SU(3)$, one can describe the strong nuclear force. This time the object ψ in Eq. (2.1) has three components, representing three colours of quarks of the same flavour, all with the same mass m. The global $SU(3)$ transformations U acting on ψ are of the form

$$U = \mathrm{e}^{i\alpha_S \sum\limits_{a=1}^{8} C_a \lambda_a} \ ,$$

with a coupling strength parameter $\alpha_S > 0$, $C_a \in \mathbb{R}$ and the eight Gell-Mann matrices λ_a, which are the generators of the $SU(3)$ group. Making the C_a space-time-dependent breaks the global symmetry in the same way as it did in the other examples, and again this can be solved by introducing one gauge field for each generator of the gauge group into the theory via the covariant derivative:

$$(D_\mu \psi)_a = \partial_\mu \psi_a - i(\alpha_S G^i_\mu S_i)_{ab} \psi_b \ .$$

This has the same structure as Eq. (2.2), but this time there are eight gauge fields G^a_μ, and the group generators are represented through $S_a = \frac{1}{2}\lambda_a$. Choosing the gauge fields to transform as

$$G^a_\mu \to G^a_\mu + \partial_\mu C_a + 2\alpha_S f_{abc} C_b G^c_\mu$$

makes the Lagrangian invariant under local gauge transformations. This is analogous to the $U(1)$ example except for the last term, which contains the $SU(3)$ structure constants f_{abc} and arises from the fact that it is a non-Abelian gauge group. The presence of these terms implies gluon self-interactions. The free term of the G_μ fields has the same structure as in Eq. (2.3). The only differences are the structure constant and coupling constants.

The fields G_μ in this model represent the eight gluons of QCD, the bosons that allow to transition from one colour state of the ψ triplet to another.

2.2 Electroweak Symmetry Breaking

As described in Sec. 2.1, adding mass terms of gauge fields to the Lagrangian of a theory makes it inconsistent, as the terms break the symmetry that the gauge fields were introduced to restore. Thus, the procedure outlined in Sec. 2.1 to introduce particle interactions to a quantum field theory can only describe the real world if there are no massive gauge bosons. This is in conflict with the observation of massive W and Z bosons by the UA2 and UA1 collaborations at CERN [15–18]. This section presents the Higgs mechanism, a solution to this apparent contradiction.

2.2.1 Masses of Bosons

Approaches to solve the problem of massive gauge bosons (before observing it) were first introduced in 1964 [19–21]. The first step is assuming the presence of an $SU(2)$ complex spin-0 doublet

$$\phi = \begin{pmatrix} \phi^+ \\ \phi^0 \end{pmatrix} = \frac{1}{\sqrt{2}} \begin{pmatrix} \phi_1 + i\phi_2 \\ \phi_3 + i\phi_4 \end{pmatrix} \ .$$

The Lagrangian of this field is

$$\mathcal{L} = (\partial_\mu \phi)^\dagger (\partial^\mu \phi) - V(\phi) \ , \tag{2.4}$$

with the Higgs potential

$$V(\phi) = \mu^2\phi^\dagger\phi + \lambda(\phi^\dagger\phi)^2 \,. \tag{2.5}$$

It can be easily verified that this Lagrangian $\mathcal{L}$ is invariant under global $SU(2)$ transformations of ϕ and $U(1)$ transformations of its components ϕ^+ and ϕ^0, which is known as $SU(2) \times U(1)$ symmetry.

In the case $\mu^2 < 0$, the potential has an infinite number of minima. Every field configuration that satisfies

$$\phi^\dagger\phi = \frac{1}{2}(\phi_1^2 + \phi_2^2 + \phi_3^2 + \phi_4^2) = -\frac{\mu^2}{2\lambda} = \frac{v^2}{2}$$

minimizes the potential and thus is a ground state of the system. The quantity v that is introduced here is called the vacuum expectation value of ϕ. In the considered case $\mu^2 < 0$, spontaneous symmetry breaking occurs, as the system will gravitate towards one of the ground states and, expanded around this specific ground state, it will not exhibit the $SU(2) \times U(1)$ symmetry that it has when expanded around the origin. This can be seen in Fig. 2.1, where the potential is symmetric around the origin but not around any of the minima of the potential.

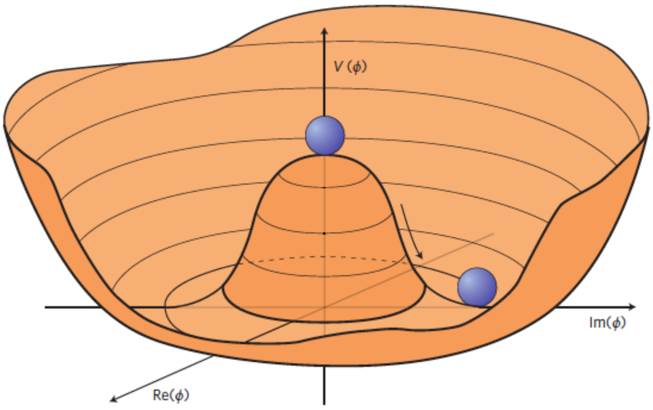

Figure 2.1: Graphic representation of the Higgs potential in the case of $\mu^2 < 0$.

The ground state of ϕ is chosen to be

$$\phi_0 = \frac{1}{\sqrt{2}}\begin{pmatrix}0\\ v\end{pmatrix} \,.$$

This choice is based on the photon being observed to be massless even when the W and Z bosons are massive, meaning that one symmetry of the potential must remain unbroken despite a non-trivial ϕ_0. The state ϕ_0 is invariant under the application of

$$Q = T^3 + \frac{Y}{2} \; .$$

This equation connects the electric charge Q of a particle to its hypercharge Y and the third component T^3 of its weak isospin. It also shows how the symmetry group of the Lagrangian transforms when inserting ϕ_0:

$$SU(2) \times U(1)_Y \xrightarrow{\phi_0} U(1)_Q \; ,$$

reducing the number of group degrees of freedom from four to one.

Expanded around ϕ_0, the doublet ϕ takes the form

$$\phi = \frac{1}{\sqrt{2}} \begin{pmatrix} \phi_1 + i\phi_2 \\ v + H + i\phi_4 \end{pmatrix} \; .$$

Using the $SU(2) \times U(1)$ gauge freedom, the contributions from ϕ_1, ϕ_2 and ϕ_4 can be removed, so that

$$\phi = \frac{1}{\sqrt{2}} \begin{pmatrix} 0 \\ v + H \end{pmatrix}$$

with the physical Higgs field H. This choice is called the unitary gauge.

With the same procedure as in Sec. 2.1, interactions to gauge bosons can be introduced to this model by imposing local gauge symmetry. Since both $SU(2)$ and $U(1)$ symmetry are required, the covariant derivative takes the form

$$D_\mu = \partial_\mu + igW_\mu^a T^a + ig' B_\mu \; .$$

With this, it follows that

$$\begin{aligned}(D_\mu \phi)^\dagger (D^\mu \phi) = {} & \frac{1}{2} (\partial_\mu H)^\dagger (\partial^\mu H) + \frac{1}{8} g^2 (W_\mu^1 + iW_\mu^2)(W^{1\mu} - iW^{2\mu})(v + H)^2 \\ & + \frac{1}{8} (gW_\mu^3 + g' B_\mu)(gW^{3\mu} - g' B^\mu)(v + H)^2 \; .\end{aligned}$$

This term from the Lagrangian in Eq. (2.4) contains terms proportional to v^2:

$$\mathcal{L}_m = \frac{v^2}{8} \left(g^2 (W_\mu^1 + iW_\mu^2)(W^{1\mu} - iW^{2\mu}) + (gW_\mu^3 + g' B_\mu)(gW^{3\mu} - g' B^\mu) \right) \; . \tag{2.6}$$

This expression contains mass terms of gauge fields of the form $\frac{1}{2} m^2 F_\mu F^\mu$. Using the expressions

$$W^\pm = \frac{1}{\sqrt{2}} \left(W^1 \mp iW^2 \right) \qquad Z = \frac{gW^3 - g' B}{\sqrt{g^2 + g'^2}} \qquad A = \frac{g' W^3 + gB}{\sqrt{g^2 + g'^2}} \; ,$$

Eq. (2.6) can be rewritten to make these appear explicitly:

$$\mathcal{L}_m = \frac{1}{2}\left(\frac{vg}{2}\right)^2 \left(W_\mu^- W^{-\mu} + W_\mu^+ W^{+\mu}\right) + \frac{1}{2}\left(\frac{v\sqrt{g^2+g'^2}}{2}\right)^2 Z_\mu Z^\mu \, .$$

This shows that, by assuming the existence of a complex scalar $SU(2)$ doublet with a non-vanishing vacuum expectation value v and allowing it to couple to the $SU(2)$ and $U(1)$ gauge fields, mass terms for those fields can be incorporated without breaking the imposed gauge symmetries. The mass that the W bosons gain through the Higgs mechanism is $m_W = \frac{vg}{2}$ and the mass of the Z boson is $m_Z = \frac{v\sqrt{g^2+g'^2}}{2}$. The field A still has no mass term and is identified with the photon.

The terms of $(D_\mu\phi)^\dagger(D^\mu\phi)$ proportional to H or H^2 give rise to couplings between the Higgs boson and the gauge bosons. The terms containing the states W^+ and W^- are

$$\frac{1}{2}g^2 v W_\mu^- W^{+\mu} H + \frac{1}{4}g^2 W_\mu^- W^{+\mu} H^2 \, . \tag{2.7}$$

Therefore, the coupling strength g_{HWW} of the HWW vertex is

$$g_{HWW} = \frac{1}{2}g^2 v = g m_W$$

Similarly, the coupling strength of the HZZ vertex is $g_{HZZ} = m_Z\sqrt{g^2+g'^2}$. Coupling terms for A do not appear, which is another example of the coupling strength of the Higgs boson to gauge bosons being proportional to the mass of the bosons.

After expanding ϕ around ϕ_0, the form of its potential in Eq. (2.5) also changes:

$$V(H) = \frac{\mu^2}{2}(v+H)^2 + \frac{\lambda}{4}(v+H)^4 \, .$$

With $\mu^2 = -\lambda v^2$, this becomes

$$V(H) = \lambda v^2 H^2 + \lambda v H^3 + \frac{\lambda}{4}H^4 \, .$$

The first term represents a mass term of H with the mass $m_H^2 = 2\lambda v^2$. The second and third term are self-coupling terms of the Higgs boson.

The gluon introduced in Sec. 2.1.2 is the gauge boson of the $SU(3)$ symmetry, which is not broken in the SM. As such, the gluon remains massless. This concludes the introduction of the SM bosons. Their properties are summarized in Tab. 2.1.

Table 2.1: Summary of the properties of the bosons predicted by the SM. Mass values taken from Ref. [22].

Particle	Symbol	Charge	Spin	Mass [GeV/c^2]	Interaction
$W^\pm$	$W^\pm$	±1	1	80.4	Weak
Z	Z	0	1	91.2	Weak
Photon	γ	0	1	0	Electromagnetic
Gluon	g	0	1	0	Strong
Higgs	H	0	0	125.1	-

2.2.2 Masses of Fermions

A similar theoretical issue also exists regarding mass terms for the SM fermions. The mass term for a spin-$\frac{1}{2}$ particle ψ with mass m_f has the form $-m_f\bar{\psi}\psi$. The SM $SU(2)$ symmetry, however, does not apply to the full spinors, but only to the left-handed part $\psi_L = \frac{1}{2}(1-\gamma^5)\psi$. The left-handed fermions are grouped in doublets $\psi_L = \begin{pmatrix}\psi_u \\ \psi_d\end{pmatrix}_L$, which are transformed as described in Sec. 2.1.1. Right-handed projections $\psi_R = \frac{1}{2}(1+\gamma^5)\psi$ remain as $SU(2)$ singlets and are not affected by SM $SU(2)$ gauge transformations. Since $\psi_R + \psi_L = \psi$, the mass term of ψ can be decomposed as:

$$-m_f\bar{\psi}\psi = -m_f(\bar{\psi}_R\psi_L + \bar{\psi}_L\psi_R) \ .$$

Here it becomes apparent that the presence of a mass term would break gauge invariance.

Much like in Sec. 2.2.1, this can be remedied by inserting the scalar $SU(2)$ doublet ϕ into the model. Since ϕ is an $SU(2)$ doublet like ψ_L, they transform in the same way. This also means that gauge-invariant terms can be constructed by combining ψ_L and ϕ. One such combination is:

$$\mathcal{L}_f = -g_{\psi_d}\left(\bar{\psi}_L\phi\psi_{dR} + h.c.\right) \ .$$

Inserting $\phi = \frac{1}{\sqrt{2}}\begin{pmatrix}0 \\ v+H\end{pmatrix}$ as before leads to

$$\mathcal{L}_f = -\frac{g_{\psi_d}}{\sqrt{2}}v\left(\bar{\psi}_{dL}\psi_{dR} + \bar{\psi}_{dR}\psi_{dL}\right) - \frac{g_{\psi_d}}{\sqrt{2}}H\left(\bar{\psi}_{dL}\psi_{dR} + \bar{\psi}_{dR}\psi_{dL}\right) \ . \tag{2.8}$$

The left term has the structure of a mass term for the lower component ψ_d of the $SU(2)$ doublet (also called down-type fermion) ψ_L, while the right one introduces a coupling between the fermion and Higgs field. The parameter g_{ψ_d} is called the Yukawa coupling of ψ_d. It modifies the strength of the coupling to the Higgs boson as well as the mass of the fermion.

For up-type fermions, a gauge-invariant construction of a mass term can be achieved in a very similar fashion. The gauge-invariant expression to start from is

$$g_{\psi_u}\left(\bar{\psi}_L \phi^\dagger \psi_{uR} + h.c.\right)$$

and the calculation results in an expression of the same structure as Eq. (2.8). In both cases, the relation between the Yukawa coupling and the fermion mass is

$$g_f = \sqrt{2}\frac{m_f}{v}\ . \tag{2.9}$$

The Yukawa couplings are proportional to the fermion masses.

The SM fermions are grouped in two fermion classes and three generations, the members of which differ only in their masses. A generation of the lepton class consists of a charged lepton, which can interact electromagnetically and weakly, and a neutrino, which can only interact weakly. The SM leptons and their properties are listed in Tab. 2.2.

The second class of fermions are the quarks. These can interact strongly, weakly and electromagnetically. Due to their colour charge and the size of the QCD coupling constant, they do not appear as free particles in nature, but form compounds known as hadrons. The two types of hadrons are the mesons comprising a quark and an anti-quark, and the baryons consisting of three quarks. The six SM quarks are listed in Tab. 2.3.

Table 2.2: Properties of the SM leptons [22].

Particle	Symbol	Charge	Spin	Mass [MeV/c^2]
Electron Neutrino	ν_e	0	1/2	0.511
Electron	e	-1	1/2	$< 1.1 \cdot 10^{-6}$
Muon Neutrino	ν_μ	0	1/2	106
Muon	μ	-1	1/2	$< 1.1 \cdot 10^{-6}$
Tau Neutrino	ν_τ	0	1/2	1777
Tau Lepton	τ	-1	1/2	$< 1.1 \cdot 10^{-6}$

Table 2.3: Properties of the SM quarks [22].

Particle	Symbol	Charge	Spin	Mass [GeV/c^2]
Up	u	2/3	1/2	0.0022
Down	d	-1/3	1/2	0.0047
Charm	c	2/3	1/2	1.27
Strange	s	-1/3	1/2	0.093
Top	t	2/3	1/2	173
Bottom	b	-1/3	1/2	4.18

2.3 Properties of Higgs Bosons

This section describes some of the observed Higgs-boson properties that are the most relevant for the studies described throughout this thesis. These are the main production and decay processes of the SM Higgs boson in high-energy proton collisions as well as its spin and CP properties.

2.3.1 Production and Decay

The leading-order Feynman diagrams of the four most prevalent production processes are shown in Fig. 2.2. Their respective cross-sections as a function of the proton-proton centre-of-mass energy $\sqrt{s}$ can be seen in Fig. 2.3a, and the values at $\sqrt{s} = 13$ TeV and $m_H = 125$ GeV are listed in Tab. 2.4. The gluon-gluon fusion (ggF) process has the highest cross-section. As shown in Fig. 2.2a, it is initiated by two gluons which, via a virtual-quark loop, produce a Higgs boson. Due to the Yukawa coupling scaling with the quark mass, see Eq. 2.9, the cross-section contribution from a particular type q of quark is proportional to m_q^2. Therefore, the main contribution comes from virtual top quarks.

Vector-boson fusion (VBF) has the second largest cross-section, and this process is very interesting experimentally due to its unique signature. As can be seen in Fig. 2.2b, it produces two jets in addition to a Higgs boson. These are likely to have a large momentum and propagate close to the direction of the proton beams. This also makes it unlikely to find more jets in the central detector region, since no other particles with colour charge are produced. Since few other processes produce such event topologies, VBF Higgs production is more easily separated from background processes than ggF.

The third most prevalent Higgs-boson production process is the associated production with a vector boson (VH), also called Higgs-strahlung, depicted in Fig. 2.2c.

a) Gluon-gluon fusion (ggF) **b)** Vector-boson fusion (VBF)

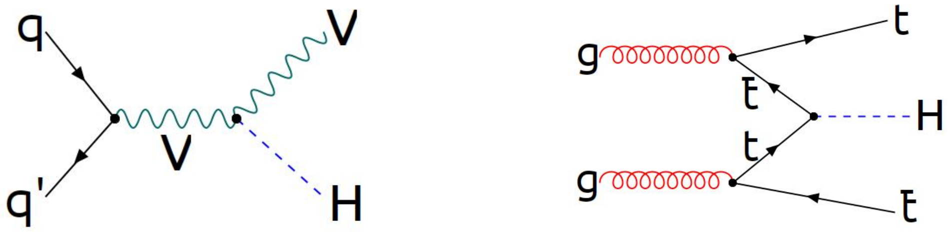

c) Associated production with vector boson (VH) **d)** Associated production with top quarks (ttH)

Figure 2.2: Leading-order (LO) Feynman diagrams of the dominant Higgs-boson production processes in proton collisions at $\sqrt{s} = 13$ TeV.

This process is only possible for $V = W, Z$ but not for photons or gluons, since these are massless and do not couple to the Higgs boson.

The associated production with a pair of top quarks (ttH) is depicted in Fig. 2.2d.

The Higgs boson is not a stable particle, and can thus only be detected by reconstructing its decay products. Due to its coupling to all massive SM particles, it has many decay channels. The most important decay for this thesis is the $H \to \tau\tau$ channel. At leading perturbative order, the analytic expression for the partial decay width of a Higgs boson into a pair of τ leptons is:

$$\Gamma(H \to \tau\tau) = \frac{g^2 m_H m_\tau^2}{32\pi m_W^2} \left(1 - \frac{4m_\tau^2}{m_H^2}\right)^{\frac{3}{2}} .$$

Based on the partial widths for all Higgs-boson decay channels, the branching ratio for each channel can be calculated. These calculations at the highest available precision have been conducted using HDECAY [24] and PROPHECY4F [25]. The results as a function of the Higgs-boson mass are summarized in Fig. 2.3b.

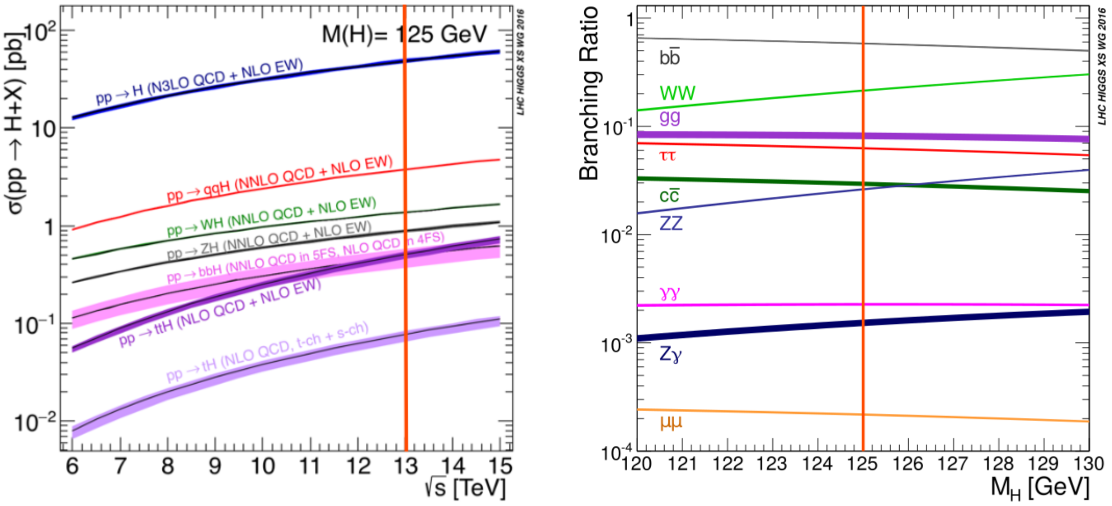

(a)

(b)

Figure 2.3: (a): Production cross-section of the Higgs boson in proton-proton scattering for various production mechanisms as a function of the centre-of-mass energy $\sqrt{s}$. (b): Higgs-boson branching ratios as a function of the Higgs-boson mass. The energy of $\sqrt{s} = 13$ TeV and the observed Higgs-boson mass of 125 GeV have been marked with vertical orange lines [23].

The currently most precise calculation of the $H \to \tau\tau$ branching ratio based on PROPHECY4F and HDECAY yields:

$$\mathrm{BR}(H \to \tau\tau) = 0.0627 \pm 0.0014\ .$$

2.3.2 Spin and CP properties

The SM predicts the Higgs boson to be a spin-0 scalar particle with even parity. Since the Landau-Yang theorem [47, 48] forbids decays of massive spin-1 particles to two photons, but the $H \to \gamma\gamma$ decay channel has been observed, it follows that the observed Higgs boson is not a spin-1 particle.

To distinguish between other spin hypotheses, the ATLAS collaboration examined Higgs-boson events in different bosonic final states [49]. The measurement strongly supports the SM prediction of a CP-even scalar, while excluding many other spin hypotheses at over 99% confidence level, as shown in Fig. 2.4. One of the excluded scenarios is the purely CP-odd Higgs boson, but no strong statement

Table 2.4: Production cross-sections of the SM Higgs boson assuming a mass of 125 GeV in proton-proton collisions with a centre-of-mass energy of 13 TeV [26–46].

Process	cross-section [pb]	Order QCD	Order EWK
ggF	$48.58^{+4.6\%}_{-6.7\%}(\text{theory})^{+3.2\%}_{-3.2\%}(\text{PDF} + \alpha_S)$	N^3LO	NLO
VBF	$3.782^{+0.5\%}_{-0.3\%}(\text{theory})^{+2.1\%}_{-2.1\%}(\text{PDF} + \alpha_S)$	NNLO	NLO
WH	$1.380^{+0.7\%}_{-1.5\%}(\text{theory})^{+2.2\%}_{-2.2\%}(\text{PDF} + \alpha_S)$	NNLO	NLO
ZH	$0.8696^{+3.8\%}_{-3.8\%}(\text{theory})^{+2.2\%}_{-2.2\%}(\text{PDF} + \alpha_S)$	NNLO	NLO
ttH	$0.5085^{+5.7\%}_{-9.3\%}(\text{theory})^{+8.8\%}_{-8.8\%}(\text{PDF} + \alpha_S)$	NLO	LO

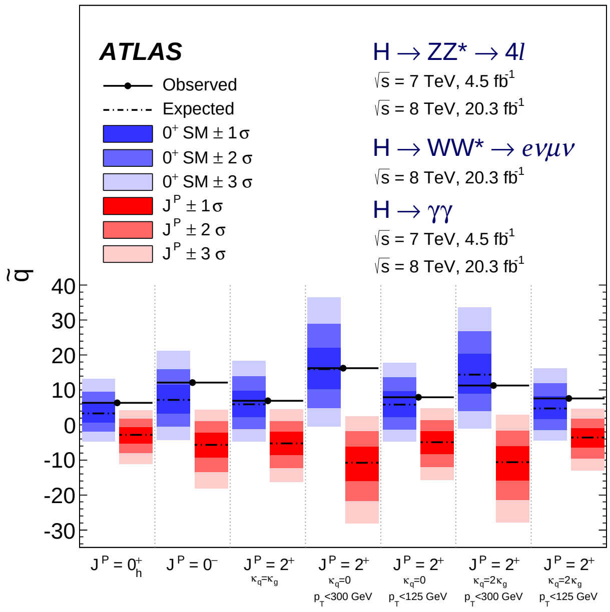

Figure 2.4: Overview of observed test statistic values $\tilde{q}$ to differentiate between the SM Higgs spin/CP prediction and several alternative hypotheses, obtained from measurements in bosonic Higgs-boson final states [49]. The SM expectation is shown in blue, while the alternative hypotheses are marked in red.

is made on the scenario of a mainly CP-even mass eigenstate with a smaller CP-odd contribution. dedicated measurement to test this possibility was performed in 2016 [50], using the Optimal-Observable method described in Sec. 3.4. The result is shown in Fig. 2.5, where the first constraints on the CPV inducing parameter $\tilde{d}$ are shown. The analysis presented in this thesis expands on the method applied to obtain a more sensitive result.

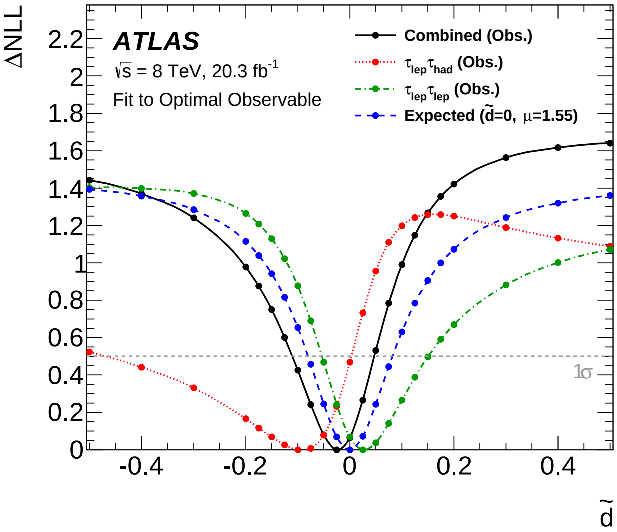

Figure 2.5: Observed (black) and expected (blue) ΔNLL curves for the parameter $\tilde{d}$ that induces CPV in VBF Higgs production, obtained in the $H \to \tau\tau$ final state. The ΔNLL value is a measure of the goodness of the fit of a hypothesis to the observed data, with ΔNLL= 0 marking the best-fitting scenario. The two observed subchannel results for events with two leptonically decaying τ leptons (green) and only one leptonically decaying τ lepton (red) are shown.

2.4 Properties of τ Leptons

Since Higgs bosons are unstable, they are experimentally only accessible through their decay products. In the analyses presented in Chap. 7 and Chap. 8, Higgs-boson decays into τ leptons are investigated. This section provides an overview of their phenomenological properties.

With a mass of

$$m_\tau = 1776.86 \pm 0.12 \text{ MeV} ,$$

τ leptons are the heaviest of the three types of charged SM leptons [22]. They can only decay by emitting a virtual W boson and producing a τ neutrino, which cannot be directly observed. The W boson can decay leptonically into an electron or muon and the corresponding neutrino, but it can also decay into an up and a down quark, more rarely also a strange quark.

In τ-lepton decays to quarks, these further hadronize to produce colour-neutral mesons, primarily pions. In most cases, the resulting mesons include either one or three charged particles. Decays to five or more charged mesons are possible but rare. The branching fractions of τ leptons are shown in Fig. 2.6a. The procedure with which ATLAS reconstructs hadronically-decaying τ leptons is described in Sec. 5.4. One important feature in the reconstruction is that τ leptons have a proper decay length of $c\tau = 87.03$ μm, which means that they can traverse a measurably large distance within the detector before decaying. Also, the jet formed by a τ-lepton decay is more collimated than quark- or gluon-initiated jets, as depicted in Fig. 2.6b.

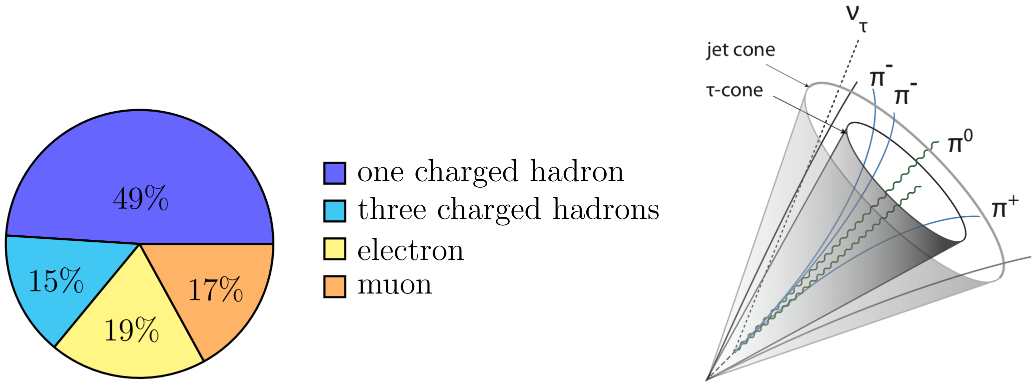

(a) (b)

Figure 2.6: (a): Branching fraction of a τ lepton to experimentally distinguished decay channel classes [22]. (b): Sketch of a τ-lepton decay to a neutrino, three charged and one neutral pion. The drawn cones indicate the larger width of jets initiated by a quark or a gluon instead of a τ lepton, which helps to differentiate these processes.

CHAPTER 3

CP Violation and Anomalous HVV Couplings

In 1932, Carl Anderson discovered particles with the same mass as electrons, but the opposite electric charge [51]. This was the first experimental observation of antimatter as predicted by Dirac's equation [52], with the same properties as its matter counterpart, except for reversed additive quantum numbers. CP symmetry states that a physical system evolves in the same way when containing matter as when containing antimatter (charge conjugation, C) and being mirrored (parity, P). It also implies that, whenever matter is created or destroyed, the same thing must occur to the same amount of antimatter. This is in conflict with the fact that almost no antimatter has been observed in the universe.

The main topic of this thesis is a test of CP violation in the coupling of the Higgs boson to vector bosons, also referred to as "HVV couplings." This chapter covers the CP-violating processes within the SM and explains why more such processes are expected outside of the SM and how CP conservation in particle interactions can be tested.

3.1 CP Violation in the Standard Model

The only interaction that is known to break CP symmetry in the SM is the weak force. In 1964, CPV was observed in the decay of neutral kaons [53]. This showed that CPV is possible in weak interactions of quarks. To incorporate this property into the theory, the Cabibbo-Kobayashi-Maskawa (CKM) matrix was introduced [9, 10]. This section covers the theoretical description of CPV in the SM and its implications for the asymmetry between baryons and antibaryons in the universe.

The introduction of CPV was combined with the observation that the mass eigenstates q of the quarks, i.e. the physical particles, are not the same as the weak eigenstates q', which are the states that couple to W bosons. If these are not the same, a unitary matrix V can be introduced to describe the mixing of mass eigenstates and weak eigenstates as follows:

$$\begin{pmatrix} d' \\ s' \\ b' \end{pmatrix} = \begin{pmatrix} V_{ud} & V_{us} & V_{ub} \\ V_{cd} & V_{cs} & V_{cb} \\ V_{td} & V_{ts} & V_{tb} \end{pmatrix} \begin{pmatrix} d \\ s \\ b \end{pmatrix} .$$

This matrix V is known as the CKM matrix, and in the Wolfenstein parametrization the entries take the following form [54]:

$$V = \begin{pmatrix} 1-\lambda^2/2 & \lambda & A\lambda^3(\rho - i\eta) \\ -\lambda & 1-\lambda^2/2 & A\lambda^2 \\ A\lambda^3(1-\rho-i\eta) & -A\lambda^2 & 1 \end{pmatrix} .$$

The latest measurements for the four parameters yield [22]:

$$\lambda = 0.22650 \pm 0.00048 \ , \quad A = 0.790^{+0.017}_{-0.012} \ , \quad \rho = 0.141^{+0.016}_{-0.017} \ , \quad \eta = 0.357 \pm 0.011 \ .$$

The source of CPV in a theory including quark mixing with the CKM matrix is the parameter η, since it causes the quark states in W exchanges to have different complex phases. Due to interference between the contributions from different quark flavours to electroweak loop diagrams, the presence of different complex phases can lead to a discrepancy between the rates of particle and anti-particle reactions and thus violate CP symmetry.

Since this is the only mechanism in the SM that is known to break CP conservation, the impact it has on the baryon-antibaryon asymmetry of the universe has been studied in great detail [3–7]. It was concluded that the amount of asymmetry

$$\frac{n_B - n_{\bar{B}}}{n_\gamma} \approx \frac{n_B}{n_\gamma}$$

generated through the CKM matrix is below 10^{-19}, meaning roughly that for every 10^{19} antibaryons produced, there are $10^{19}+1$ baryons produced. But compared to the observed value of $6 \cdot 10^{-10}$ from measurements of the cosmic microwave background conducted in Ref. [55], the baryon asymmetry from the CKM matrix is negligible. This is one of the main reasons why it is expected that CP-violating processes beyond the SM exist.

3.2 Effective Field Theories

The Effective Field Theory (EFT) framework [56] was devised to probe new physics without assuming a specific extension of the SM. This framework does not introduce any specific BSM particles, but adds new Lorentz-invariant operators to the SM Lagrangian that consist of combinations of the SM fields. Each one of these operators has a prefactor f, known as Wilson coefficient, and a power of the hypothetical energy scale Λ corresponding to the mass of the lightest BSM particle. Thus, Lagrangians of EFT models have the following structure:

$$\mathcal{L}_{\text{EFT}} = \mathcal{L}_{\text{SM}} + \sum_i \frac{f_i^5}{\Lambda} \mathcal{O}_i^5 + \sum_i \frac{f_i^6}{\Lambda^2} \mathcal{O}_i^6 + \ldots$$

The superscript of the operators $\mathcal{O}_i$ indicates their mass dimension. Since Lagrangians are of mass dimension 4, all dimension-5 operators are suppressed by $1/\Lambda$, while dimension-6 are suppressed by $1/\Lambda^2$ etc. As Λ is typically assumed to be of the order of 1 TeV or greater since current experimental results show no sign of new particles up to this scale, this serves as a way to regulate the contribution from the more complicated higher-order operators, making EFT models theoretically and computationally more feasible. The Wilson coefficients are a way to access these operators experimentally. Finding the value of any of the f_i to be incompatible with zero would be a sign of BSM physics.

The lowest-order CP-odd EFT operators that contribute to HVV couplings are of dimension 6. No such operators with mass dimension 7 can be constructed, and as contributions from dimension-8 operators are much more strongly suppressed, only the dimension-6 operators will be considered. The main goal of this thesis is to measure the Wilson coefficients of such dimension-6 operators, since their interference with the CP-even SM HVV operators defined in Eq. (2.7) can lead to different rates between VBF with quarks or anti-quarks in the initial state.

3.3 Parametrization of Anomalous HVV Couplings

There are 76 Lorentz-invariant possibilities to combine SM fields into dimension-6 operators. When taking the SM equations of motion of the fields into account, it becomes apparent that some of these operators are linearly dependent, and only 59 independent operators remain. Which set of 59 operators to use is up to preference. Depending on the focus of an analysis, one specific choice of operators can simplify the calculations compared to other choices. Therefore, different EFT bases have been used in different contexts. The one used for the VBF $H \to \tau\tau$ CP analysis is described in the following.

A big simplification regarding the basis choice for the presented analysis is that its scope is limited to CP-odd extensions of the HVV couplings. Out of the 59 independent operators of dimension-6 EFTs, only 3 contribute to these. Since the analysis is not sensitive to any other operators, the Wilson coefficients of these operators are assumed to be equal to zero, making their corresponding terms in the Lagrangian irrelevant in the context of this thesis.

The simplified EFT Lagrangian for the $H \to \tau\tau$ analysis, including the remaining three operators, can be written as [57]:

$$\mathcal{L}_{eff} = \mathcal{L}_{SM} + \frac{f_{\tilde{B}B}}{\Lambda^2}\mathcal{O}_{\tilde{B}B} + \frac{f_{\tilde{W}W}}{\Lambda^2}\mathcal{O}_{\tilde{W}W} + \frac{f_{\tilde{B}}}{\Lambda^2}\mathcal{O}_{\tilde{B}} \, .$$

In terms of SM fields, the three dimension-6 operators are defined as:

$$\mathcal{O}_{\tilde{B}B} = \Phi^\dagger \hat{\tilde{B}}_{\mu\nu}\hat{B}^{\mu\nu}\Phi \qquad \mathcal{O}_{\tilde{W}W} = \Phi^\dagger \hat{\tilde{W}}_{\mu\nu}\hat{W}^{\mu\nu}\Phi \qquad \mathcal{O}_{\tilde{B}} = (D_\mu\Phi)^\dagger \hat{\tilde{B}}^{\mu\nu} D_\nu \Phi \, .$$

Here, $\hat{B}_{\mu\nu} = i\frac{g'}{2}B_{\mu\nu}$ and $\hat{W}_{\mu\nu} = \frac{i}{2}g\sigma^a W^a_{\mu\nu}$ with the Pauli matrices σ^a. The covariant derivative in the $SU(2) \times U(1)$ theory is $D_\mu = \partial_\mu + \frac{i}{2}g'B_\mu + i\frac{g}{2}\sigma^a W^a_\mu$, and the dual field strength tensors $\tilde{V}_{\mu\nu}$ is defined as $\tilde{V}_{\mu\nu} = \epsilon_{\mu\nu\rho\sigma}V^{\rho\sigma}$ with the antisymmetric Levi-Civita tensor ϵ and $V^{\rho\sigma}$ as defined in Sec. 2.1.

The operator $\mathcal{O}_{\tilde{B}}$, in addition to HVV couplings, also contributes to CP-odd triple gauge-boson couplings, which have already been experimentally accessible at the LEP collider. The L3 [58] and OPAL [59] collaborations have strongly constrained these couplings and with them the Wilson coefficient $f_{\tilde{B}}$. For this reason, the operator $\mathcal{O}_{\tilde{B}}$ is omitted in the following.

The remaining two operators can be rewritten after electroweak symmetry breaking in the mass basis of the W, Z and γ bosons:

$$\mathcal{L}_{eff} = \mathcal{L}_{SM} + \tilde{g}_{HAA}H\tilde{A}_{\mu\nu}A^{\mu\nu} + \tilde{g}_{HAZ}H\tilde{A}_{\mu\nu}Z^{\mu\nu} + \tilde{g}_{HZZ}H\tilde{Z}_{\mu\nu}Z^{\mu\nu} + \tilde{g}_{HWW}H\tilde{W}^{+}_{\mu\nu}W^{\mu\nu}_{-} \, .$$

Of the four anomalous coupling strengths $\tilde{g}_{HVV}$, only two are independent. Therefore, they can be expressed in terms of two dimensionless parameters $\tilde{d}$ and $\tilde{d}_B$:

$$\begin{aligned}
\tilde{g}_{HAA} &= \frac{g}{2m_W}(\tilde{d}\sin^2\theta_W + \tilde{d}_B\cos^2\theta_W) \qquad & \tilde{g}_{HAZ} &= \frac{g}{2m_W}\sin 2\theta_W(\tilde{d} - \tilde{d}_B) \\
\tilde{g}_{HZZ} &= \frac{g}{2m_W}(\tilde{d}\cos^2\theta_W + \tilde{d}_B\sin^2\theta_W) & \tilde{g}_{HWW} &= \frac{g}{m_W}\tilde{d} \, ,
\end{aligned}$$

with the weak mixing angle $\theta_W = \arctan(\frac{g'}{g})$. Relating $\tilde{d}$ and $\tilde{d}_B$ to the Wilson coefficients yields

$$\tilde{d} = -\frac{m_W^2}{\Lambda^2}f_{\tilde{W}W} \qquad\qquad \tilde{d}_B = -\frac{m_W^2}{\Lambda^2}\tan^2\theta_W f_{\tilde{B}B} \, .$$

This makes it apparent that $\tilde{d}$ and $\tilde{d}_B$ quantify the specific contributions of different vector bosons to the CP-odd HVV coupling, which are difficult to distinguish from one another in an experiment. Therefore, the choice to simplify the parametrization of CP-odd HVV couplings further by assuming $\tilde{d}_B = \tilde{d}$ is adopted. This results in the following simplified expressions for the anomalous HVV couplings:

$$\tilde{g}_{HAA} = \tilde{g}_{HZZ} = \frac{1}{2}\tilde{g}_{HWW} = \frac{g}{2m_W}\tilde{d} \quad \text{and} \quad \tilde{g}_{HAZ} = 0 \,. \tag{3.1}$$

Hence, this EFT ansatz allows to characterize CP-odd contributions to HVV couplings with only the parameter $\tilde{d}$.

3.4 The Optimal-Observable Method

This section describes the Optimal-Observable method [60–63] employed to probe the value of $\tilde{d}$ experimentally, under the aforementioned assumptions.

The strengths of the anomalous couplings in Eq. 3.1 are all proportional to $\tilde{d}$. This implies that the matrix element $\mathcal{M}$ of VBF Higgs production including anomalous couplings can be decomposed as follows into the SM contribution $\mathcal{M}_{\mathrm{SM}}$ and the CP-odd contribution $\mathcal{M}_{\mathrm{CP-odd}}$:

$$\mathcal{M} = \mathcal{M}_{\mathrm{SM}} + \tilde{d}\mathcal{M}_{\mathrm{CP-odd}} \,.$$

Squaring this equation yields an expression proportional to the differential production cross-section:

$$|\mathcal{M}|^2 = |\mathcal{M}_{\mathrm{SM}}|^2 + 2\tilde{d}\Re(\mathcal{M}^*_{\mathrm{SM}}\mathcal{M}_{\text{CP-odd}}) + \tilde{d}^2|\mathcal{M}_{\text{CP-odd}}|^2 \,. \tag{3.2}$$

The first and third contribution are both CP-even, but the interference term between CP-odd and CP-even matrix elements is CP-odd, making it a source of CPV not accounted for in the SM. Since it is CP-odd, integrating the interference term over a CP-even part of the phase-space will yield zero, i.e. it has no influence on the total VBF cross-section. The third term, however, is CP-even and will therefore lead to an increase of the total Higgs-boson production cross-section proportional to $\tilde{d}^2$. This offers a possibility to probe $\tilde{d}$ through the observed number of Higgs-boson events, which is however not exploited in this thesis for reasons discussed in Sec. 3.5.

Instead, the focus is placed on the interference term. The first-order Optimal Observable O_{opt} is defined as:

$$O_{\mathrm{opt}} = \frac{\Re(\mathcal{M}^*_{\mathrm{SM}}\mathcal{M}_{\text{CP-odd}})}{|\mathcal{M}_{\mathrm{SM}}|^2} \,.$$

With this definition, O_{opt} combines the information of the seven-dimensional VBF phase-space into a single variable, making it very sensitive to the properties of the HVV vertex. It is calculated using the dependence of the matrix elements on the four-momenta of the involved particles: the initial-state partons that emit the vector bosons, the final-state quarks after this emission, and the Higgs boson. But in data, these are not directly accessible and must therefore be approximated. Instead of the two final-state quarks, the two jets with the highest transverse momentum, also called "tagging jets," are used. The Higgs-boson four-momentum is estimated from its decay products with the Missing Mass Calculator [64]. The initial-state parton momenta, being part of the colliding beams of protons with four-momenta p_B, are known to be of the form

$$p_i = x_{1/2} p_B \ ,$$

with the momentum fraction $x_{1/2}$ of the proton that is carried by the matrix-element parton. This can be reconstructed from the mass m and rapidity $y = \frac{1}{2} \ln \left(\frac{E+p_\parallel}{E-p_\parallel} \right)$ of the summed four-momenta of the final-state tagging jets and reconstructed Higgs boson:

$$x_{1/2} = \frac{m_{\text{final}}}{\sqrt{s}} \mathrm{e}^{\pm y_{\text{final}}} \ .$$

The quantity $p_\parallel$ of a particle is the projection of its momentum three-vector on the proton-beam direction.

The matrix elements are evaluated at leading order from these inputs using HAWK [33] to obtain the value of O_{opt}. But the matrix element also depends on the flavour of the incoming and outgoing partons, which can also not be determined experimentally. Instead, the matrix elements for all possible parton-flavour combinations are calculated and added up, weighted with the product of the corresponding CT10 [65] parton distribution function (PDF) values of the initial-state partons.

Example O_{opt} distributions in VBF $H \to \tau\tau$ events are shown in Fig. 3.1. This figure illustrates the analysis strategy for the test of CP conservation. By comparing the shape of the O_{opt} distribution in data to the predictions for different $\tilde{d}$ values, one can find the $\tilde{d}$ value that best describes the observation. Finding this measured $\tilde{d}$ value to be incompatible with zero would be a sign of CPV.

The predictions of the distribution in the case of $\tilde{d} \neq 0$ are obtained with an event-level reweighting algorithm. For this, CP-odd and CP-even matrix elements are calculated for each event at truth level, directly accessing the four-momenta of the matrix-element partons and the Higgs boson. The matrix elements are calculated at LO for events with two and three final-state partons to construct

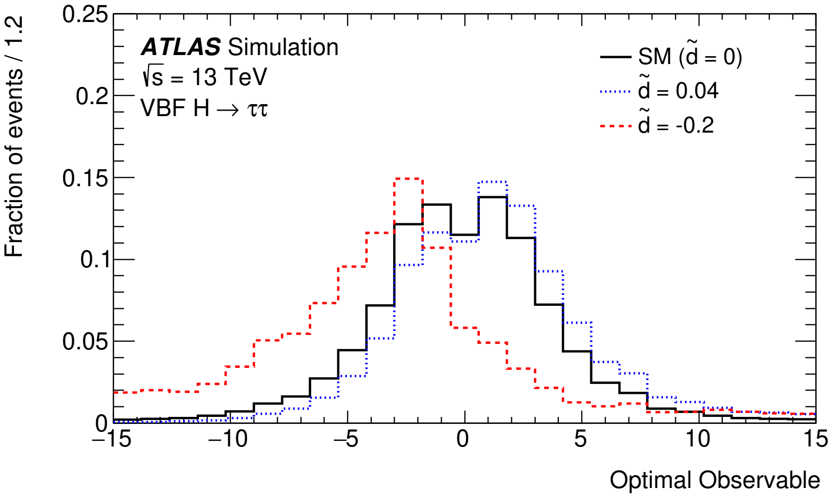

Figure 3.1: Distribution of O_{opt} in VBF $H \to \tau\tau$ events assuming different HVV coupling scenarios in the Higgs-boson production vertex. A non-zero value of $\tilde{d}$ shifts the observed mean of O_{opt} [11].

weights

$$w = \frac{|\mathcal{M}|^2}{|\mathcal{M}_{\text{SM}}|^2} = 1 + 2\tilde{d}\frac{\Re(\mathcal{M}^*_{\text{SM}}\mathcal{M}_{\text{CP-odd}})}{|\mathcal{M}_{\text{SM}}|^2} + \tilde{d}^2\frac{|\mathcal{M}_{\text{CP-odd}}|^2}{|\mathcal{M}_{\text{SM}}|^2}\ .$$

Applying these weights to the events of a sample of simulated SM VBF Higgs-boson production events replaces their SM cross-section with the cross-section of arbitrary hypotheses with $\tilde{d} \neq 0$. This makes it possible to make predictions of data distributions in the presence of anomalous couplings without having to generate signal samples of such hypotheses.

The reweighting method was validated using MadGraph5_aMC@NLO [66]. For this, a SM VBF sample and several non-SM VBF samples were created at NLO precision in QCD. For the non-SM samples, different $\tilde{d}$ hypotheses were assumed. To test the validity of the reweighting, the weights were applied to the SM sample. Afterwards, distributions of different variables were compared between the reweighted SM and a BSM sample generated with the same $\tilde{d}$ value as the weights applied to the SM sample. Such a test of the O_{opt} distribution is shown in Fig. 3.2, and the two samples are well compatible over the whole O_{opt} range, showing that the reweighting algorithm can be used in order to avoid generating additional samples.

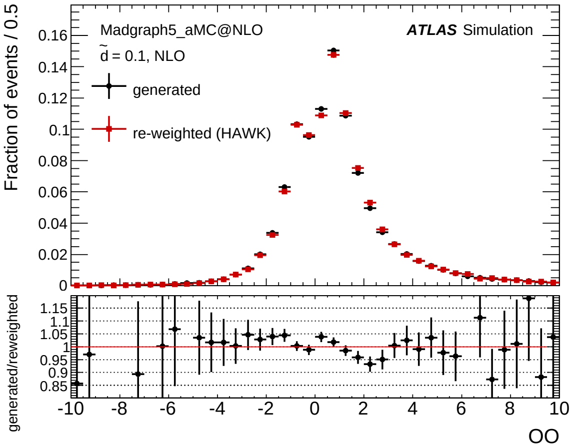

Figure 3.2: Distribution of the Optimal Observable OO in a VBF sample generated with $\tilde{d} = 0.1$ (red) and a SM sample that was reweighted to $\tilde{d} = 0.1$ (black) [50].

The dependence of O_{opt} on $\tilde{d}$ can be investigated by calculating its mean value:

$$\langle O_{\text{opt}} \rangle = \frac{\int O_{\text{opt}}(\mathrm{d}\sigma_{\text{SM}} + \tilde{d}\ \mathrm{d}\sigma_{\text{CP-odd}} + \tilde{d}^2\ \mathrm{d}\sigma_{\text{CP-even}})}{\int (\mathrm{d}\sigma_{\text{SM}} + \tilde{d}\ \mathrm{d}\sigma_{\text{CP-odd}} + \tilde{d}^2\ \mathrm{d}\sigma_{\text{CP-even}})} \,.$$

The separation of the differential cross-section into three parts is based on the three parts of the squared matrix element $|\mathcal{M}|^2$ in Eq. (3.2), since these quantities are proportional. As O_{opt} is a CP-odd observable, its mean will vanish when integrated over a CP-even cross-section term. Similarly, the integral over the CP-odd cross-section term will vanish if it has no CP-odd prefactor. Thus, the expression can be simplified to

$$\langle O_{\text{opt}} \rangle = \frac{\tilde{d} \int O_{\text{opt}}\ \mathrm{d}\sigma_{\text{CP-odd}}}{\int \mathrm{d}\sigma_{\text{SM}} + \tilde{d}^2 \int \mathrm{d}\sigma_{\text{CP-even}}} \,.$$

This shows that, for small $\tilde{d}$ values, the mean value of O_{opt} rises linearly, while for larger $\tilde{d}$ values, the $\tilde{d}^2$ term in the denominator becomes dominant and the mean value decreases with $1/\tilde{d}$. As the dependence of $\langle O_{\text{opt}} \rangle$ is linear around $\tilde{d} = 0$, the O_{opt} distribution changes strongly for varying values of $\tilde{d}$ close to zero, while the change is smaller for high $\tilde{d}$ values.

3.5 Model Dependence of CP Tests

This section discusses the implicit assumptions that go into a test of CP conservation using the Optimal-Observable method, and what can be done to reduce the model dependence.

Firstly, to conduct a pure test of CP conservation, the estimate of the total observed signal yield should be independent from the measurement of the best-fit value of the CPV inducing parameter $\tilde{d}$. The reason is that there can be contributions to the differential cross-section from CP-even EFT operators, which would have the same form as in Eq. (3.2). In the case of a CP-even contribution, the interference term as well as the last term would be CP-even, which means that they impact the total production cross-section. As this effect cannot be fully disentangled from the cross-section change introduced by $\tilde{d} \neq 0$, this information should not be used for a test of CPV. The shape of the O_{opt} distribution can be used instead, since its mean will not be shifted in the presence of CP-even anomalous couplings. The disadvantage is that a pure shape analysis is not as sensitive as an analysis that takes the total signal event yield into account, since not all the information in the data is used.

It is also worth noting that the qq' initial state of VBF is not a C eigenstate. Therefore, a CP-odd observable which gives a non-zero expectation value only in case of CPV in VBF cannot be constructed [67]. The probability distribution of the qq' state is, however, P-invariant. This means that, when ignoring the experimentally inaccessible spin configurations of the involved particles, it is also invariant under the "naive time reversal" operator T_N as defined in Ref. [68]. This operator transforms a single-particle state $|\phi(p,s)\rangle$ of momentum p and spin s into

$$T_N|\phi(p,s)\rangle = |\phi(-p,-s)\rangle \ ,$$

whereas

$$P|\phi(p,s)\rangle = \eta_\phi|\phi(-p,s)\rangle \ ,$$

with the intrinsic parity η_ϕ of the field. As an alternative to a CP-odd observable, one can define a T_N-odd observable, such as O_{opt}, instead to perform a CP test, when no CP-odd observables can be constructed.

This difference becomes important in the presence of BSM particles with masses below the EFT scale Λ of new physics that enter the VBF process via loop corrections. Such on-shell loop corrections are also referred to as rescattering. With rescattering, the VBF transition amplitude can incur contributions that are not T_N-symmetric, which can shift the mean value of O_{opt} without necessarily violating CP conservation.

To conclude, measuring a significantly asymmetric O_{opt} distribution would imply either rescattering or CPV in VBF. Both of these are BSM phenomena, but in order to claim an observation of CPV based on an O_{opt} measurement, the absence of rescattering, or only a negligible effect from it, must either be assumed or proven in a separate study. This assumption can be argued to be well-motivated, since no evidence of particles that could cause rescattering has been observed yet.

Despite not being the same as CP-odd observables, T_N-odd observables are also referred to as CP-odd throughout this thesis, since negligible rescattering effects are assumed in the interpretation of the obtained results.

CHAPTER 4

The ATLAS experiment at the LHC

In this chapter, the experimental setup used to produce the data used in the presented analyses is described. An important part of this setup is the Large Hadron Collider (LHC), the largest high-energy particle accelerator in the world, which is located at CERN near Geneva. The collision events produced by the LHC synchrotron are reconstructed with different detectors. In the case of this thesis, data reconstructed with the ATLAS detector are used. The following sections describe the components of these machines, what purpose they fulfill and how they performed in the data-taking period from 2015 to 2018, also referred to as Run 2.

4.1 The LHC Accelerator

The LHC is a collision ring with a 27 km circumference, constructed within a tunnel that is about 100 m underground [69]. Its main purpose is to accelerate particles to very high energies and making them collide. For the data used in this thesis, the accelerated particles were protons, but the LHC also accelerates lead ions.

Its main constituents are two nearly circular beam pipes, containing beams that rotate in opposite directions, and superconducting dipole magnets producing an 8.3 T field to control the beams. The protons are obtained by removing the electrons from hydrogen atoms and injecting them into the LHC at a beam energy of 450 GeV. Before injecting the protons into the LHC, they pass through smaller pre-accelerators. The CERN accelerator complex is depicted in Fig. 4.1. It also

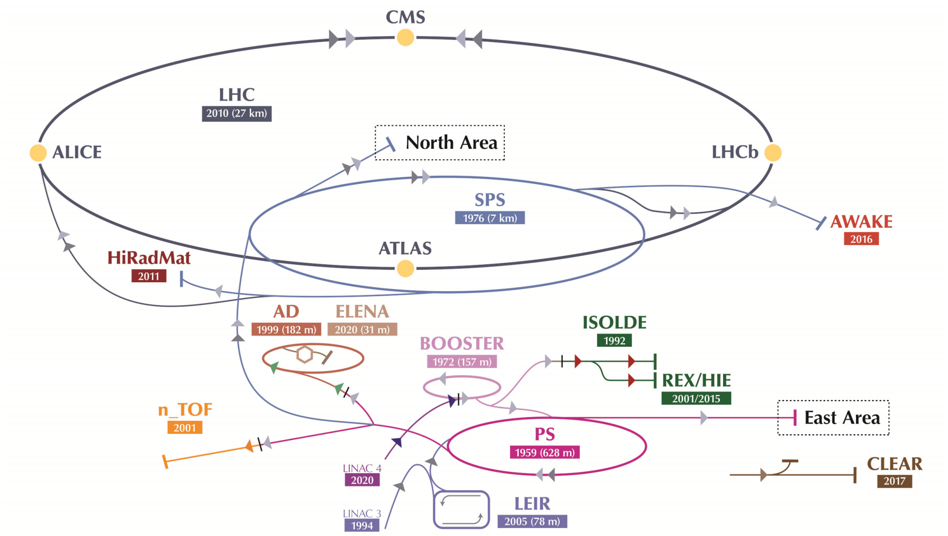

Figure 4.1: Sketch of the CERN accelerator complex, including the LHC, its pre-accelerator chain and the positions of the four largest detectors.

shows the beam-crossing points, where particle detectors have been built to examine the collisions. The most important one for this thesis is the ATLAS detector, designed to discover the Higgs boson, measure the properties of SM particles and find evidence for BSM physics [70].

The luminosity L is a measure of the beam intensity. It connects the cross-section σ of a specific process to its event rate $\frac{\mathrm{d}N}{\mathrm{d}t}$ via

$$\frac{\mathrm{d}N}{\mathrm{d}t} = L\sigma \ .$$

Thus, in order to record as many events as possible, L needs to be maximized. The goal during the construction of the LHC was to reach $L = 10^{34}\ \mathrm{cm}^{-2}\mathrm{s}^{-1}$. This goal was reached in 2016, and even doubled in 2017. To describe the size of a dataset, the time-integrated luminosity is often used. This is a measure of the total number of produced proton-proton interactions, often given in units of fb^{-1}, where $1\ \mathrm{b} = 10^{-28}\ \mathrm{m}^2$. The evolution of the integrated luminosity throughout Run 2 is shown in Fig. 4.2. The full Run-2 dataset that can be used for physics analyses amounts to $139\ \mathrm{fb}^{-1}$.

Increasing the luminosity to large values comes at a cost. If, during the same crossing of proton bunches from the two beams, multiple protons collide, the scattering particles will reach the detector at the same time. This leads to overlapping detector signals, making a correct reconstruction of events more difficult. The number of proton-proton interactions per bunch-crossing is named pile-up μ, and

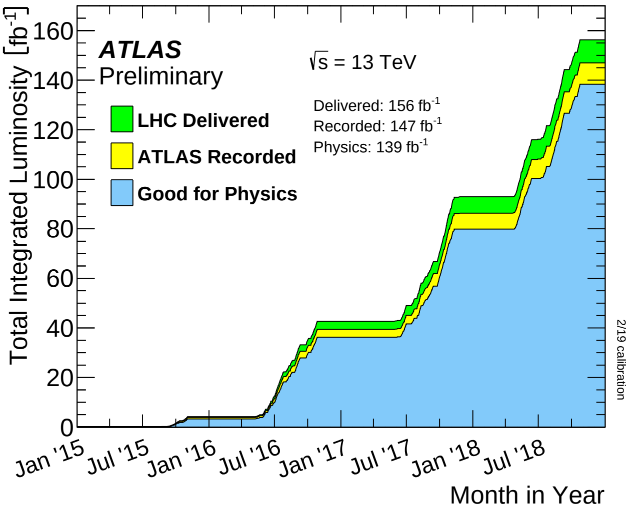

Figure 4.2: Time-integrated luminosity throughout the LHC Run-2 data-taking period [71]. The overall recording efficiency of the ATLAS detector as well as temporary technical problems of subdetectors lead to a slight decrease of data usable for physics analyses with respect to the produced amount.

its distribution in Run 2 is shown in Fig. 4.3.

4.2 The ATLAS Detector

The ATLAS detector [70] is a multi-purpose detector, originally designed to discover the SM Higgs boson, measure its properties and those of other SM particles, and find hints for BSM physics. It has a cylindrical shape with a length of 44 m and a diameter of 25 m, covering almost a 4π solid angle around the interaction point at its centre. The central part of the detector is called barrel, and at its ends, the end-caps are positioned. A picture of the detector is shown in Fig. 4.4.

The ATLAS collaboration uses a right-handed coordinate system, with the z axis pointing in the beam direction. The $x - y$ plane is perpendicular to the z axis, with the x axis pointing to the centre of the LHC and the y axis pointing upwards from the interaction point. More commonly, a spherical coordinate system is used, with the azimuthal angle ϕ describing angles in the $x - y$ plane. The polar angle θ gives the deviation from the beam direction. Instead of directly using θ, the

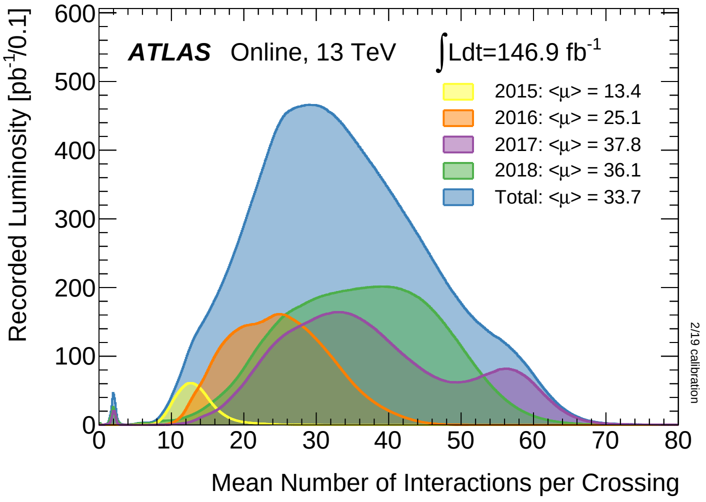

Figure 4.3: Pile-up profile during Run-2 data-taking [71]. The profile of 2017 shows two peaks, since two different proton-bunching schemes were used in that year.

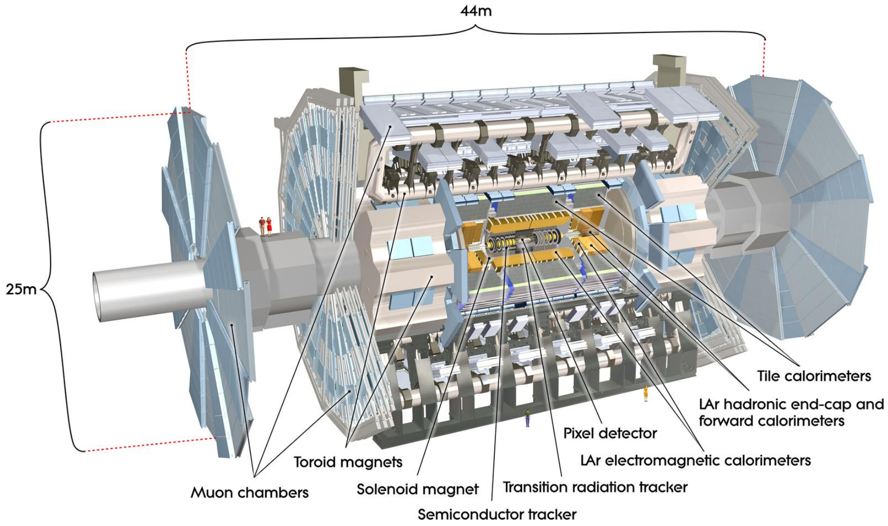

Figure 4.4: Illustration of the ATLAS detector in cut-away view [70].

rapidity y and pseudorapidity η are often used:

$$y = \frac{1}{2} \ln \left(\frac{E - p_z}{E + p_z} \right)$$
$$\eta = - \ln \left(\tan \left(\frac{\theta}{2} \right) \right) ,$$

where p_z is the momentum of a particle in z direction and E is its energy. The difference between the y values of two particles is invariant under Lorentz boosts in z direction. The pseudorapidity η is equivalent to y in the case of massless particles, and a good approximation if $p \gg m$. It is often preferred over the usage of y since it only depends on the polar angle θ, which is easier to measure than E and p_z for highly relativistic particles. To describe angular distances between two particles, it is common to use

$$\Delta R = \sqrt{(\Delta\phi)^2 + (\Delta\eta)^2} .$$

To be able to identify different types of processes, the detector comprises several subsystems that fulfill different tasks: The inner detector (InDet), the electromagnetic calorimeter (ECal), the hadronic calorimeter (HCal), the forward calorimeter (FCal) and the muon spectrometer (MS). The coverage of these subdetectors as well as their energy/momentum resolution for incoming particles are summarized in Tab. 4.1. In the following sections, a brief description of the different parts of the detector, as well as their subcomponents, is given.

Table 4.1: Energy and momentum resolutions of the ATLAS detector's subsystems. The coverage of the detector parts in $|\eta|$ is also given [70, 72–74]. The resolution given for the ECal describes electromagnetic showers, while for the HCal and FCal the resolutions on energies of hadronic showers are given.

Component	Resolution (p_T/E in GeV)	$\lvert\eta\rvert$ range
Inner detector	$\frac{\sigma_{p_\mathrm{T}}}{p_\mathrm{T}} = 0.04\% \cdot p_\mathrm{T} \oplus 2\%$	$[0, 2.5]$
Electromagnetic calorimeter	$\frac{\sigma_E}{E} = \frac{0.1}{\sqrt{E}} \oplus \frac{0.4}{E} \oplus 1\%$	$[0, 3.2]$
Hadronic calorimeter	$\frac{\sigma_E}{E} = \frac{0.5}{\sqrt{E}} \oplus 3\%$	$[0, 3.2]$
Forward calorimeter	$\frac{\sigma_E}{E} = \frac{1}{\sqrt{E}} \oplus 10\%$	$[3.1, 4.9]$
Muon spectrometer	$\frac{\sigma_{p_\mathrm{T}}}{p_\mathrm{T}} = 10\%$ at $p_\mathrm{T} = 1$ TeV	$[0, 2.7]$

4.2.1 Inner Detector

The ATLAS inner detector is closest to the beam pipe, and uses silicon sensors to reconstruct interaction vertices and trajectories of charged particles. It consists of three subsystems: The pixel detector, the semiconductor tracker (SCT) and transition radiation tracker (TRT). These parts are shown in Fig. 4.5. They contain sensors that are ionized by incoming charged particles. This ionization produces an electric signal often named a "hit." Since the InDet is structured in layers, the hits in different detector layers can be used to reconstruct particle tracks.

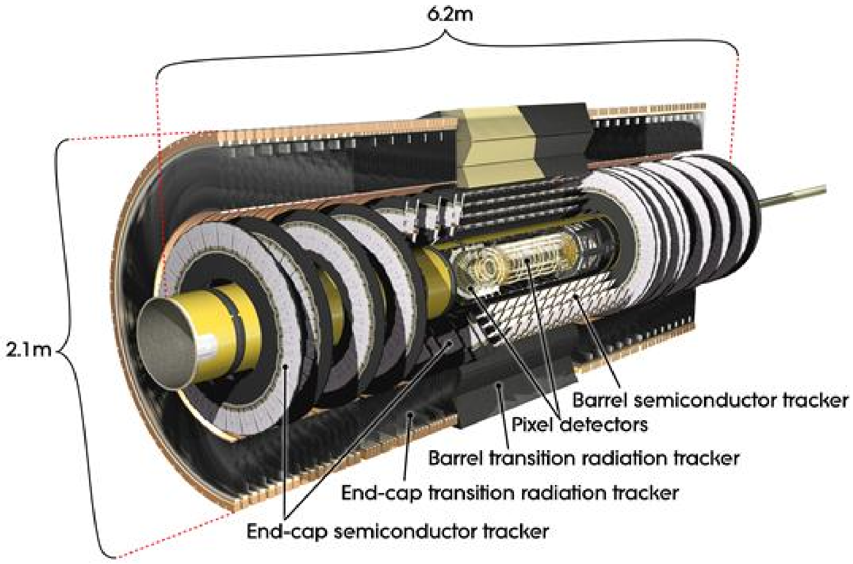

Figure 4.5: Cut-away view of the ATLAS inner detector [70].

To measure the momentum of incoming charged particles, the InDet is immersed in a 2 T solenoid magnetic field that bends their trajectories. From the measured curvature, the ratio q/p of charge and momentum of an incoming particle can be obtained.

The innermost part of the InDet is the pixel detector, containing over 80 million pixels that are 50×400 μm^2 in size. It is designed to give very good spatial resolution of the incoming particles, and consists of three cylindrical layers. Since Run 2, an additional pixel layer named Insertable B-Layer (IBL) was placed closest to the beam pipe, further improving the vertex reconstruction and thus the identification of b quarks and τ leptons which produce secondary vertices when decaying.

The pixel detector is surrounded by the SCT, which is composed of four layers of silicon microstrips. The positional resolution achieved by the SCT is around 20 μm in $r - \phi$ direction and 600 μm in z direction.

The TRT is made of straw tubes which are positioned parallel to the beam pipe in the barrel and orthogonal to it in the end-caps. In addition to providing further tracking information, the signal amplitude of the TRT tubes is sensitive to the Lorentz boost factor γ of incoming particles [75]. Therefore, the TRT hits in the 36 layers a particle traverses on average are separated in low-threshold and high-threshold hits depending on the measured ionization. High-threshold hits are much more likely to originate from ultra-relativistic particles with high γ factor, which helps distinguish electrons from hadrons such as pions. Moreover, the TRT has a positional resolution in $r-\phi$ direction of 13 μm.

4.2.2 Calorimeters

The ATLAS detector relies on three calorimeters for the energy measurement of photons, electrons and hadrons: The ECal, the HCal and the FCal. All of them are sampling calorimeters, meaning that they consist of two types of materials which are layered alternatingly: an active material and a passive absorber material. The calorimeters stop incoming particles by absorbing them in the absorber material and initiating particle showers, while their energy is measured through the signal that the showers leave in the active material. The layout of the calorimeters is shown in Fig. 4.6.

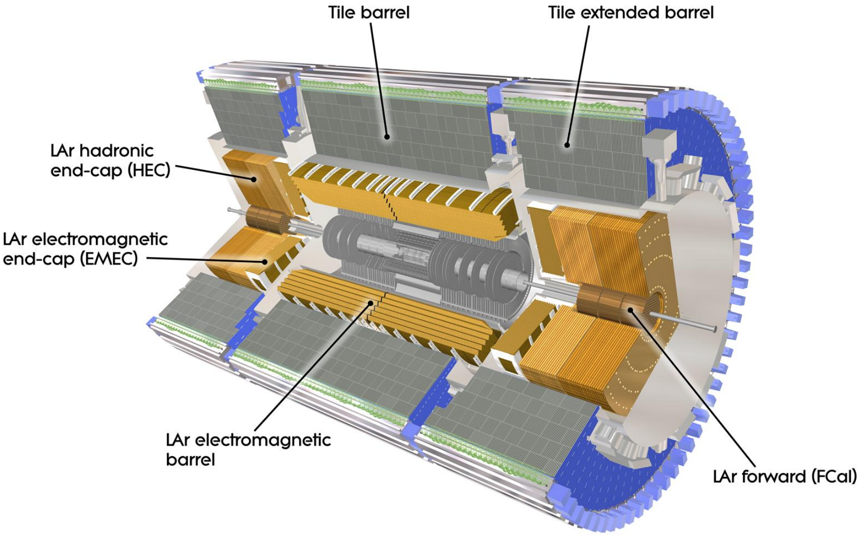

Figure 4.6: Schematic representation of the ATLAS calorimetry system [70].

The ECal has passive layers made of lead, while liquid argon (LAr) is used for the active layers. It is split into a barrel part covering $|\eta|$ values up to 1.475 and two end-caps (EMEC) covering $|\eta| \in [1.375, 3.2]$. The depth of the barrel part is over 22 radiation lengths X_0. This is a material-independent measure of how far a particle can traverse the material before reducing its energy by a factor of 1/e due to electromagnetic interactions with the material. The end-caps are over 24 X_0 deep. The positional resolution is 0.025×0.1 in $\Delta\eta \times \Delta\phi$ in the barrel and 0.025×0.025 for the EMEC. To correct for particles starting showering before the first lead layer, a presampler LAr layer is installed inside of the ECal.

The HCal is built around the ECal. Its barrel part, covering $|\eta| < 1.7$, has steel absorber layers and scintillator tiles as active material. The hadronic end-cap calorimeter (HEC) covers the range $|\eta| \in [1.5, 3.2]$ and uses copper as absorber and LAr as active material. The HCal has a granularity of 0.1×0.1 for $|\eta| < 2.5$ and 0.2×0.2 for larger $|\eta|$ values.

The FCal is built very closely around the beam pipe, to cover forward-scattered particles with $|\eta| \in [3.1, 4.9]$. It has three absorber layers. The first one is made of copper, which is well-suited for absorbing electromagnetically interacting particles. The other two are made of tungsten, intended for hadrons. The active material of the FCal is LAr.

4.2.3 Muon Spectrometer

Muons leave tracks in the InDet, but pass through the calorimeters while retaining most of their energy, since they are minimally ionizing particles. To identify muon tracks, the muon spectrometer is built around the calorimeters, with 4 T toroid magnets to bend the muon trajectories. The MS consists of four subdetectors, as shown in Fig. 4.7.

For high-precision spatial resolution, the Monitored Drift Tube (MDT) chambers are used in the range $|\eta| < 2.7$. The tubes in these chambers contain a gas that is ionized by traversing muons, achieving a spatial resolution of about 35 μm. In the innermost MS layer, the MDTs only cover $|\eta| < 2.0$. Cathode-Strip Chambers (CSC) are used instead for $2.0 < |\eta| < 2.7$. These have better time resolution and rate capability, but the spatial resolution is slightly reduced.

In addition to these very precise subdetectors, the MS also contains two subdetectors designed to process muon signals as quickly as possible. The Resistive Plate Chambers (RPC) cover the area $|\eta| < 1.05$, the Thin Gap Chambers (TGC) $1.05 < |\eta| < 2.4$, and they can deliver track information within a few tens of nanoseconds.

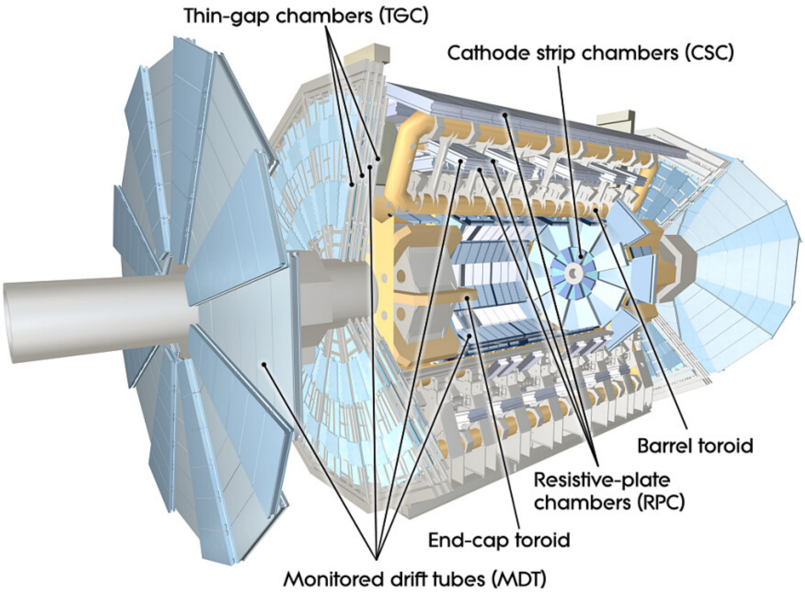

Figure 4.7: Muon system of the ATLAS detector [70].

4.2.4 Trigger System

The LHC operates at a nominal collision rate of 40 MHz. This high rate makes it impossible to store all collision events for physics analyses. Therefore, the trigger system was introduced. This system comprises a variety of fast algorithms searching for specific properties in the events, to decide whether to keep or discard the event information permanently.

In Run 2, this system was split into the hardware-based Level-1 (L1) trigger and the software-based Higher-Level Trigger (HLT) [76]. Any event that does not pass both of these levels is discarded. The L1 trigger has the goal to reduce the accepted event rate from 40 MHz to 100 kHz. The HLT examines the remaining events and reduces the event rate to a manageable 1 kHz which are then recorded for further analysis.

To process events as quickly as possible, the L1 does not use information from the InDet, since the reconstruction of tracks from hits is too computationally intensive. In order for events to pass the L1 trigger, they must exhibit either large energy deposits in the calorimeters or distinct tracks in the RPCs and TPCs. The detector parts that show these features are identified as regions of interest (ROIs), which are then used as inputs for the HLT algorithms to further classify the event. There are different groups of HLT algorithms designed to detect the presence of specific objects in an event. The HLT tests events for signatures of electrons, photons, muons, hadronic τ-lepton decays, jets, b-quark-induced jets, missing transverse momentum, and decays of hadrons containing b or c quarks. An event is discarded by the trigger system if none of these signatures is found. The algorithms that identify hadronically-decaying τ leptons are described in more detail in Sec. 6.1, since they are used to select the events analyzed in Chap. 7 and 8.

4.3 Simulation of Proton-Proton Collisions

In order to compare the predictions of the SM and other theories to observed data distributions, proton-proton collisions are commonly simulated assuming certain interaction properties for the involved particles. This section outlines the procedure applied to generate Monte-Carlo (MC) simulated collision events.

4.3.1 Description of Protons

In the SM, protons are described as particle compounds of three valence quarks: two u quarks and a d quark. But due to the valence quarks strongly interacting with each other, other particles, such as gluons or s quarks, are transiently produced. Therefore, the interacting particles in proton-proton collisions are not necessarily u or d quarks.

This phenomenon is quantified with parton distribution functions (PDFs), which give the probability f_a to find a parton of the species a in an interacting proton. The PDFs depend on the fraction x of the total proton energy carried by the parton as well as the energy scale μ that quantifies the order of magnitude of momentum transferred during the investigated interaction. Example collections of PDFs for all parton species, named PDF sets, are shown in Fig. 4.8. While for high x values, the valence quarks have the highest PDF values, they become less important as x decreases. It is also worth noting that with increasing energy scale μ, the PDF values of the gluons increase considerably.

These PDFs can be used to calculate cross-sections σ in proton-proton collisions as combinations of partonic cross-sections σ_{ij}:

$$\sigma = \sum_{i,j} \int_0^1 \mathrm{d}x_1 \int_0^1 \mathrm{d}x_2 f_i(x_1, \mu_F) f_j(x_2, \mu_F) \sigma_{ij} \ . \tag{4.1}$$

This equation is based on the factorization theorem, stating that low-momentum and high-momentum interactions can be calculated separately [78]. This implies that the low-momentum interactions within the proton can be described through the PDFs independently from the high-momentum scattering described with σ_{ij}.

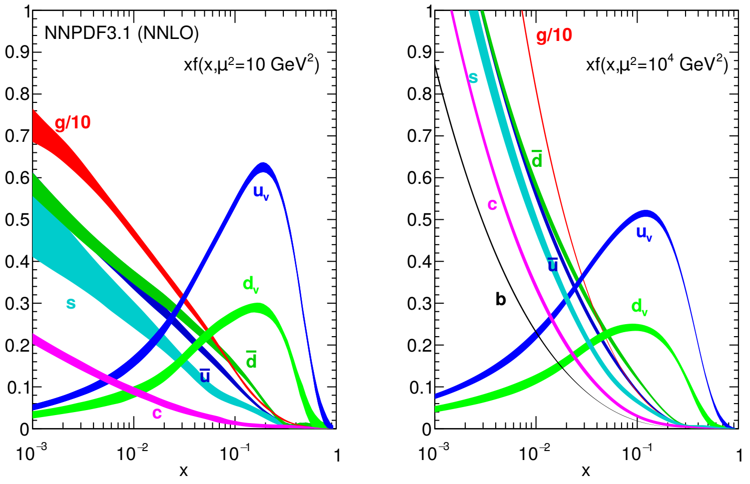

Figure 4.8: Values of the NNPDF set for different partons in the case of $\mu^2 = 10\ (\mathrm{GeV})^2$ (left) and $\mu^2 = 10^4\ (\mathrm{GeV})^2$ (right) [77].

To achieve this separation, an energy scale μ_F named factorization scale must be introduced.

4.3.2 Simulation of Parton Interactions

The coupling strength α_S introduced in Sec. 2.1 is often treated as effectively energy-dependent. This is due to the regularization and renormalization of the SM, which are conducted to remove unphysical divergent cross-sections. The divergent parts can be absorbed into the SM coupling strengths, which gain a dependence on the renormalization scale μ_R that was introduced to the theory for this procedure.

After introducing μ_R, the partonic cross-section encoded in the expression σ_{ij} in Eq. (4.1) can be evaluated perturbatively in α_S. Depending on the number of orders of α_S that are included in this calculation, starting from the lowest possible order, it is referred to as a leading-order (one order of α_S), next-to-leading order (2 orders), next-to-next-to-leading order (3 orders) etc. To obtain the σ_{ij}, the transition amplitudes are calculated. Afterwards, events with the according distribution of particles are generated using MC simulation. Events at this stage of simulation are named "parton-level" or "generator-level" events.

In addition to the products of the hard scattering process, or also as part of them, proton-proton collisions will in most cases produce partons that are not bound in colour-neutral states. These will, if they have a sufficiently high momentum, split into more colour-charged particles via the modes $q \to qg$, $g \to q\bar{q}$ or $g \to gg$. By splitting into numerous particles, the average energy per particle decreases and a

QCD jet is formed from the parton. In simulation, this typically ends when the particle energies reach values of around 1 GeV [79]. At that point, the particles merge to form colour-neutral bound states. This hadronization step cannot be simulated perturbatively, as α_S is large at low energy scales. Instead, different simplified models are devised to describe it, and are implemented in programs known as parton showers. These models come with a number of parameters that were measured in dedicated experiments, and complete sets of values for these parameters are known as "tunes." The generation of hadrons from remnants of the colliding protons is named "underlying event" and, like the hadronization of final-state partons of the hard scattering process, is simulated using parton showering programs. A summary of all steps in the simulation chain up to this point is shown in Fig. 4.9.

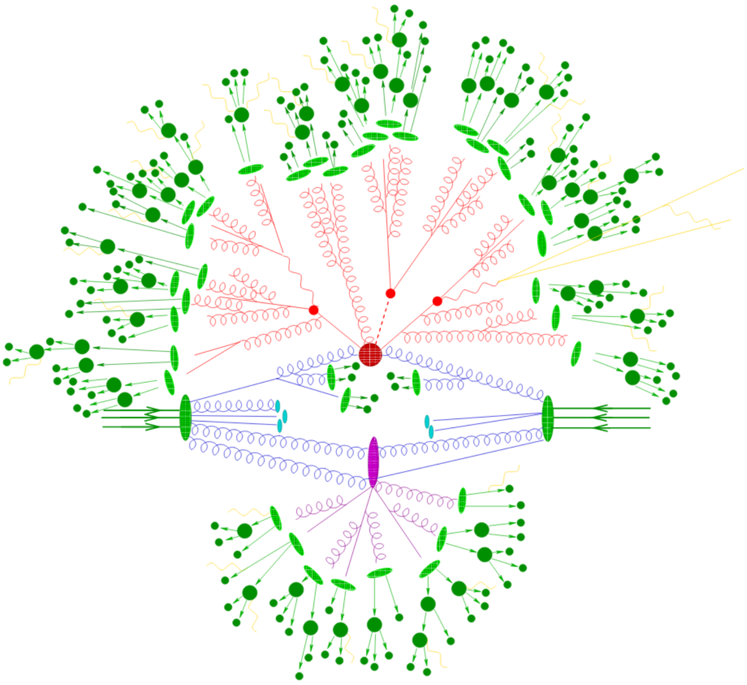

Figure 4.9: Pictorial representation of a simulated proton-proton collision event. The hard interactions are marked by red blobs, while hadronization and decay of the resulting hadrons are marked in dark and light green. The remnants of the beam are marked in light blue, and the underlying event activity is marked in purple. Photon radiation is marked in yellow [80].

The effects of pile-up collisions that arise in the investigated bunch-crossing ("in-time pile-up") and the previous and following bunch-crossings ("out-of-time pile-up") are included in the simulation by overlaying simulated minimum-bias events which do not contain the signatures of a hard scattering process to the simulated events of the desired process. To make the simulated collisions more comparable with the ones produced by the LHC, a detector simulation [81] based on the program GEANT4 [82] is performed. Using a model of the detector geometry, the detector response on the MC-generated events is simulated. Fully simulated events before the detector simulation step are named "truth-level" events, while after it they are named "reconstruction-level" events. Only events at reconstruction level are directly comparable to data.

CHAPTER 5

Object Reconstruction

This chapter describes the methods used within the ATLAS collaboration to identify different types of particles based on ionization in the InDet and MS and energy deposits in the calorimeters, which is necessary to classify collision events and reconstruct the underlying interactions. These methods are based on combining InDet tracks, MS tracks and calorimeter energy clusters. The InDet tracks are reconstructed from hits in the pixel detector, the SCT and the TRT. Pattern reconstruction algorithms are employed to combine hits to tracks, and multiple tracks sharing a common origin are used to reconstruct vertices [83, 84]. Calorimeter energy clusters are constructed with a topological grouping of individual calorimeter cells where incoming particles deposited energy using a pattern recognition algorithm [85].

5.1 Electrons and Photons

Electrons are reconstructed in the central region $|\eta| < 2.47$ by matching InDet tracks to clusters in the ECal, which is done by comparing their η and ϕ values [86]. If matching pairs of tracks and clusters are found, the electron energy is taken from the cluster, while the direction is taken from the InDet information, to use the most exact information.

To identify electrons among the thus reconstructed candidates, a likelihood-based discriminator is defined. This discriminator has numerous input variables, to separate electrons from light-flavour jets initiated by u, d or s quarks, photons or heavy-flavour jets initiated by c and b quarks. Some of the most relevant variables are the signal in the TRT, the transverse impact parameter of the electron's associated track with respect to the beam line and the shower profile in the ECal. The transverse impact parameter is the projection on the transverse plane of the distance between the track and the beam line at their point of closest approach. Three cuts of varying strictness are applied on this likelihood-based electron identifier to define the loose, medium and tight identification working points. The analyses described in Chap. 7 and 8 both use electrons passing the medium identification.

To separate prompt electrons from those produced from decays of heavy-flavour quarks or within jets, isolation criteria are applied, since the former tend to have little detector activity around the candidate. Calorimeter-based and track-based isolation criteria are defined, measuring either the deposited energy around the ECal cluster of the electron or the summed p_T of tracks around the electron track, checking the detector region up to $\Delta R = 0.2$ to the cluster barycentre and the track. The barycentre of a calorimetric cluster is defined as the average direction of all clustered cells weighted by the deposited energy measured in them.

The FCLoose isolation working point, applied in Chap. 8, is defined by requiring that the energy in the ECal isolation region, subtracting the electron cluster, be below 20% of the estimated p_T of the electron, and additionally that the sum of the p_T of all tracks with $\Delta R < 0.2$ be below 15% of the electron p_T. The gradient isolation working point used for the electrons in the analysis in Chap. 7 has varying isolation energy thresholds to achieve an efficiency of 90% for 25 GeV electrons that rises linearly to 99% for electrons with 60 GeV.

Since photons share similar signatures in the ECal as electrons, the reconstruction of electrons and photons are conducted in parallel [87]. Separate reconstruction algorithms for converted and unconverted photons are applied, where converted means that the photons split into an electron-positron pair before reaching the ECal. While unconverted photons are reconstructed as ECal clusters for which no matching tracks are found, the converted photons require two matching oppositely-charged tracks originating from the same vertex.

5.2 Muons

Muons are reconstructed from tracks in the InDet and the MS [88]. Additionally, calorimeter information is used in the region $|\eta| < 0.1$ where the read-out cables of the InDet require a gap in the MS.

Different types of reconstructed muons are distinguished. The most relevant ones for the analyses presented in this thesis are the combined muons, which are reconstructed from InDet tracks and MS tracks that could be matched to one another due to similar η and ϕ values. Other types are defined for cases where either the track quality is not sufficient in the MS or InDet due to a low number of hits, or in $|\eta| < 0.1$ using energy deposits in the calorimeters that match InDet tracks and are compatible with minimally ionizing particles.

The identification of muons among these reconstructed candidates is based on three variables:

- significance of q/p, which compares the two independent measurements of the matched InDet and MS tracks: $\left|\frac{(q/p)_{\mathrm{InDet}}-(q/p)_{\mathrm{MS}}}{\sqrt{\sigma^2_{\mathrm{InDet}}+\sigma^2_{\mathrm{MS}}}}\right|$, where the subscript InDet/MS describes the detector subsystem in which the q/p measurement was conducted and σ is the uncertainty on each of the two measurements.
- ρ', the absolute value of the difference between the transverse momentum[1] p_{T} in the InDet and MS, divided by the value measured from the combined track.
- normalized χ^2 of the combined track fit described in Ref. [89].

Loose, medium and tight identification criteria for muons are defined by placing requirements of varying strictness on these three variables.

Similarly to the electrons, isolation criteria are defined to distinguish muons produced within QCD jets from promptly produced muons. The FixedCutTightTrackOnly working point, used in Chap. 6 and 8, requires $p_{\mathrm{T}}^{\mathrm{varcone30}}/p_{\mathrm{T}}^{\mu} < 0.06$. The variable $p_{\mathrm{T}}^{\mathrm{varcone30}}$ is the sum of p_{T} of tracks with $p_{\mathrm{T}} > 1$ GeV in a cone of size $\Delta R = \min(10\ \mathrm{GeV}/p_{\mathrm{T}}^{\mu}, 0.3)$. The gradient isolation working point, used in Chap. 7, has varying requirements for the energy found around the muon calorimeter deposit and the sum of p_{T} of tracks around the muon to ensure an isolation efficiency that rises linearly from 90% for 25 GeV muons to 99% for 60 GeV muons.

5.3 Jets

Jets induced by colour-charged particles leave energy in both the ECal, HCal and FCal, and their charged constituents additionally produce tracks in the InDet. To form jets from the topological clusters in the calorimeters, the anti-k_t algorithm [90, 91] is used with the radius parameter $R = 0.4$. Before applying the anti-k_t algorithm, the “particle flow” algorithm is used for the jets measured in Chap. 8. Such particle-flow jets do not include the calorimeter energy clusters that can be associated to InDet tracks in the calculation of the total energy. Instead, the momentum measurements of the tracks is utilized for these, reducing

---

[1] The transverse momentum p_{T} of a particle is the projection of its momentum on the $x - y$ plane which is perpendicular to the beam axis.

the uncertainty on the part of the total jet energy that originates from charged particles.

Since the ECal, HCal and FCal are sampling calorimeters, not all the energy of incoming particles is deposited in active detector material. To estimate the total jet energy from its measured fraction, a calibration in multiple steps is applied [92]. The calibration corrects the jet direction by shifting its origin from the centre of the detector to the reconstructed vertex. Then it corrects for effects from pile-up contributions that arise in the investigated bunch-crossing ("in-time pile-up") and the previous and following bunch-crossings ("out-of-time pile-up"). Corrections are also applied to account for a dependence of the measured energy on η and the shower shape, which differs for quark- and gluon-initiated jets and is correlated to the measured energy fraction. Lastly, a comparison between responses measured in multi-jet data events and MC simulated events is conducted to account for insufficiencies in the simulation.

In order to suppress the contribution from pile-up jets to the jets produced in the scattering processes with the largest momentum transfer ("hard" interactions), the jet-vertex tagger (JVT) is used [93]. The JVT combines the information of the corrJVF and R_{pT} variables:

$$\mathrm{corrJVF} = \frac{\sum\limits_j p_{\mathrm{T}}^{\mathrm{trk}_j}(\mathrm{PV}_0)}{\sum\limits_l p_{\mathrm{T}}^{\mathrm{trk}_l}(\mathrm{PV}_0) + \frac{\sum\limits_{n\geq 1}\sum\limits_l p_{\mathrm{T}}^{\mathrm{trk}_l}(\mathrm{PV}_n)}{k \cdot n_{\mathrm{trk}}^{\mathrm{PU}}}} \qquad\qquad R_{pT} = \frac{\sum\limits_l p_{\mathrm{T}}^{\mathrm{trk}_l}(\mathrm{PV}_0)}{p_{\mathrm{T}}^{\mathrm{jet}}}\ .$$

The sums over j and l iterate over tracks associated to PV_0 or PV_n, which are the reconstructed primary vertex candidates in the event. The variable $n_{\mathrm{trk}}^{\mathrm{PU}}$ gives the total number of tracks not associated to PV_0, and $k = 0.01$. These two variables are the inputs for likelihood-based JVT discriminator which helps separate pile-up jets from hard-scattering jets with $20\ \mathrm{GeV} < p_{\mathrm{T}} < 50\ \mathrm{GeV}$, but due to the used track information, it is limited to the central detector area $|\eta| < 2.4$. For jets with $2.5 < |\eta| < 4.5$, an alternative algorithm named forward JVT is utilized [94].

Dedicated multivariate algorithms to identify b-quark-initiated jets (b-jets) among these jets have been developed. The MV2c10 algorithm [95] mostly relies on the relatively long lifetime of hadrons containing b quarks, which leads to a secondary vertex in the detector. This algorithm is used in the analysis described in Chap. 6, while the DL1r identifier [96] is used in Chap. 8. In both analyses, b-jet identification is only used to ensure orthogonality to other analysis channels and is not expected to have a significant impact on the obtained results.

5.4 Hadronic τ-Lepton Decays

Leptonic τ-lepton decays, apart from the neutrinos, leave the signatures of muons or electrons in the detector and are thus reconstructed as such. To identify the jets that originate from hadronic decays of τ leptons, a dedicated set of algorithms has been developed. As these decays contain neutrinos which cannot be directly observed, the focus of the reconstruction algorithms is placed on the remaining decay products, which are denoted with the symbol $\tau_{\text{had-vis}}$ in the following.

5.4.1 Candidate Reconstruction

Candidates for $\tau_{\text{had-vis}}$ objects are based on anti-k_t jets with radius parameter $R = 0.4$ [97]. Unlike the previously described jets, the "local hadronic calibration" [98] (LC) is applied to $\tau_{\text{had-vis}}$ seed jets. They are required to have $p_{\text{T}} > 10$ GeV and $|\eta| < 2.5$, while vetoing the transition region $|\eta| \in [1.37, 1.52]$ between the detector barrel and the end-caps. Selection and calibration algorithms are then applied to these seed jets to increase the purity of true $\tau_{\text{had-vis}}$ objects and adapt the LC energy estimation. True $\tau_{\text{had-vis}}$ objects are identified in the simulation with a geometrical matching of $\tau_{\text{had-vis}}$ candidates at reconstruction and truth level.

The vertex associated to the $\tau_{\text{had-vis}}$ candidate is chosen to be the one with the largest fraction of track momenta with $\Delta R < 0.2$ to its barycentre. Based on this vertex, the impact parameters and directions of the $\tau_{\text{had-vis}}$ are recalculated.

Only the $\tau_{\text{had-vis}}$ candidates that have either one ("1-prong", 1p) or three (3p) tracks with $p_{\text{T}} > 1$ GeV with $\Delta R < 0.2$ to its barycentre, which also fulfill quality criteria on the track impact parameter and number of hits in the pixel and SCT detectors, are kept. The efficiency of this reconstruction procedure, defined as the fraction of true $\tau_{\text{had-vis}}$ objects that are selected, is shown in Fig. 5.1 as a function of the truth-level p_{T} of the $\tau_{\text{had-vis}}$ object.

5.4.2 Calibration and Identification

A boosted regression tree (BRT) is trained to adapt the energy calibration to $\tau_{\text{had-vis}}$ objects [97]. This BRT combines basic calorimeter and InDet information, as well as a technique similar to the previously described particle-flow for charged hadron energy estimation and a simpler calorimeter-based calibration technique, to estimate the total $\tau_{\text{had-vis}}$ energy.

As the last step of the $\tau_{\text{had-vis}}$ object definition, an identification algorithm separates true $\tau_{\text{had-vis}}$ objects from the most prominent background processes that can mimic the described detector signatures. These contributions are often referred to as "fake $\tau_{\text{had-vis}}$ candidates" or simply "fakes."

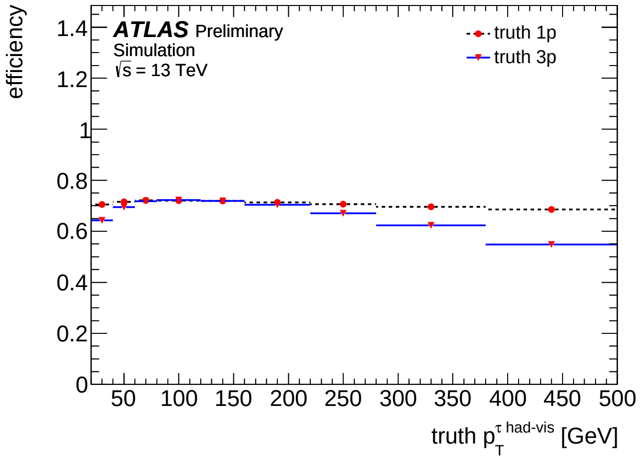

Figure 5.1: Reconstruction efficiency of $\tau_{\text{had-vis}}$, separated in 1p and 3p candidates, as a function of the truth-level p_{T} of the $\tau_{\text{had-vis}}$ object [99].

The main source of fakes are QCD jets initiated by gluons or quarks. To distinguish between these and true $\tau_{\text{had-vis}}$ objects, multivariate techniques called identification (ID) algorithms are applied. At the start of Run 2, a boosted decision tree (BDT) was used, which was later replaced by a recurrent neural network (RNN) [100]. The input variables for these mainly exploit the displaced vertex and the stronger collimation of the τ decay products, which results in charged tracks and calorimeter energy clusters being closer to one another than in the case of QCD jets.

Both methods were trained separately for 1- and 3-prong candidates using simulated $\gamma^* \to \tau\tau$ events. As background sample, di-jet events were used. The training was carried out using only $\tau_{\text{had-vis}}$ candidates with $p_{\text{T}} > 20$ GeV and $|\eta| < 2.5$ while omitting the transition region $|\eta| \in [1.37, 1.52]$ between the barrel and the end-caps. The performance of the resulting discriminators is summarized in Fig. 5.2, which shows the rejection of fake $\tau_{\text{had-vis}}$ candidates in dependence of the efficiency on true $\tau_{\text{had-vis}}$ objects of the two methods. The BDT algorithm was used the analysis presented in Chap. 7, while the RNN ID is applied in Chap. 8. The measurement in Chap. 6 was conducted with BDT as well as RNN ID to study the effect of these on the results.

In the case of 1p $\tau_{\text{had-vis}}$ candidates, a sizable fake contribution from electrons is observed [99]. Therefore, an additional BDT was trained to separate the $\tau_{\text{had-vis}}$ signal obtained in simulated $\gamma^* \to \tau\tau$ events from electrons in $Z \to ee$ samples. The main rejection power comes from the TRT, which obtains much larger signal for electrons than charged pions [75]. A cut on the score of this BDT, corresponding

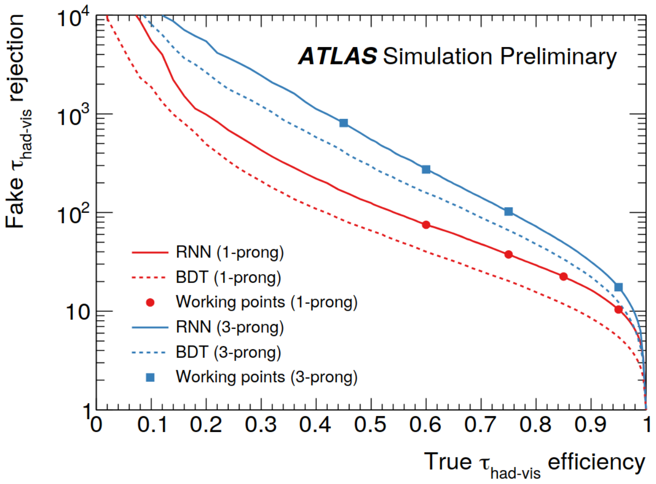

Figure 5.2: Rejection of quark- and gluon-initiated jets as a function of the true $\tau_{\text{had-vis}}$ efficiency [100]. The rejection is defined as the reciprocal value of the efficiency. The marked working points of the ID are named tight, medium, loose and very loose in the order of increasing $\tau_{\text{had-vis}}$ efficiency.

to a signal efficiency of 95%, was applied in Chap. 7, but not in Chap. 6 and 8, since the number of events containing true electrons that pass the event selections is low.

5.4.3 Reconstruction of the Di-τ Final State

To investigate fully hadronic di-τ decays in Chap. 7 and 8, the invariant di-τ mass is estimated by the Missing Mass Calculator (MMC) algorithm [64]. It aims at reconstructing the invariant mass of a particle decaying into two τ leptons. A full reconstruction of the decay requires the estimation of six to eight unknown quantities, depending on the number of leptonic τ decays. But since there are only four equations connecting these, it is impossible to identify them unambiguously.

The MMC uses the probability distribution of the ΔR between the visible τ decay products and the associated neutrino(s) to build a likelihood function for all possible decay topologies. Thus, weights can be assigned to the different decay scenarios and consequently also the mass of the mother particle of the two observed τ leptons. The $E_{\mathrm{T}}^{\mathrm{miss}}$ resolution is also taken into account in the likelihood function to reduce the impact of $E_{\mathrm{T}}^{\mathrm{miss}}$ mismeasurement on the result. By adding up the weights of different decay topologies with the same invariant di-τ mass and finding the mass with the highest sum of corresponding weights, an estimate for the invariant mass is constructed.

5.5 Missing Transverse Momentum

Since neutrinos cannot be observed directly, the conservation of momentum has to be taken into account to be able to estimate their momenta. But this approach can only be employed in the directions transverse to the beam pipe, due to the partonic nature of the colliding protons and the unknown z component of the initial state partons that follows from it.

The missing momentum in x and y direction is calculated as

$$E_i^{\text{miss}} = -\left(p_i^{\text{soft}} + \sum_r p_i^r\right)$$

for $i \in \{x, y\}$, where the sum of momenta of all reconstructed objects r, these being photons, electrons, muons, jets and $\tau_{\text{had-vis}}$, is considered [101]. The contribution p_i^{soft} is the sum of contributions from InDet tracks that could not be assigned to any of these objects.

Instead of E_x^{miss} and E_y^{miss}, the quadratic sum $E_{\text{T}}^{\text{miss}}$, referred to as missing transverse momentum or energy, and the angle ϕ^{miss} are often used:

$$E_{\text{T}}^{\text{miss}} = \sqrt{(E_x^{\text{miss}})^2 + (E_y^{\text{miss}})^2} \qquad \phi^{\text{miss}} = \arctan(E_y^{\text{miss}}/E_x^{\text{miss}}) \ .$$

5.6 Overlap Removal

A geometric overlap between different reconstructed objects can create ambiguity and possible double-counting of energies. Overlap can occur since all reconstruction algorithms apart from electrons and photons run independently. These overlaps are removed after object reconstruction by applying the following rules.

Overlap between different objects is defined using ΔR thresholds. As a first step, jets within $\Delta R = 0.2$ of a $\tau_{\text{had-vis}}$ candidate are removed, since $\tau_{\text{had-vis}}$ candidates are based on jets with further requirements applied. Jets within $\Delta R = 0.4$ of a muon or electron are also removed, since the reconstruction efficiency is higher for leptons than for jets, so the lepton candidate reconstruction is relied upon. Using the same argument, any $\tau_{\text{had-vis}}$ candidates within $\Delta R = 0.2$ of an electron or muon is removed, as well as electrons within $\Delta R = 0.2$ of a muon.

CHAPTER 6

Measurement of τ-Lepton Trigger Efficiencies

A large part of the ATLAS physics program relies on the efficient reconstruction of hadronically-decaying τ leptons. To gain access to events that contain final-state $\tau_{\text{had-vis}}$ objects, τ-lepton trigger algorithms were developed. This chapter covers the method employed to trigger on τ leptons as well as the measurement conducted to estimate the efficiencies of τ-lepton triggers in $Z \to \tau\tau$ events in ATLAS.

Investigating the trigger efficiencies ϵ is useful to locate and quantify the data loss. But the main goal of the analysis is to compare the efficiencies in data and MC simulated events. In case of a mismodelling of the trigger efficiency in the simulation, the trigger requirement leads to a mismatch between data and prediction. To account for this effect, "trigger efficiency scale factors" SF are calculated as:

$$\mathrm{SF} = \frac{\epsilon(\mathrm{Data} - \mathrm{Bkg})}{\epsilon(\mathrm{MC})} \, ,$$

where Bkg represents the background events with fake $\tau_{\text{had-vis}}$ candidates and MC stands for simulated signal events containing true $\tau_{\text{had-vis}}$ objects. These scale factors are intended for use within ATLAS, to be applied as additional event weights to MC events in all analyses that apply τ triggers.

6.1 The ATLAS τ-Lepton Trigger System

As with all other Run-2 trigger algorithms, τ-lepton triggers are separated in L1 and HLT parts, the combinations of which are called trigger chains. The HLT part itself applies several cuts on different properties of $\tau_{\text{had-vis}}$ candidates. A schematic overview of the full sequence of applied cuts is given in Fig. 6.1.

As the reconstruction of tracks takes too long to be used at L1, the L1 τ-trigger items are limited to using calorimeter information. They select narrow energy deposits in the ECal and HCal and apply cuts to the total energy [102]. In some cases, an isolation requirement is also applied, placing an upper threshold on the energy measured in the ECal isolation region. Some L1 items also apply topological requirements such as angular separation or overlap removals between different L1 objects.

The events that pass the L1 requirements are processed by the HLT, which has access to more accurate position and energy measurements. After topological clusters are formed from the calorimeter deposits, the total transverse energy $E_{\text{T}} = E/\cosh(\eta)$ of the $\tau_{\text{had-vis}}$ candidate is estimated either based on a simple pile-up subtraction method or with a BRT, and candidates must pass different cut thresholds. Information from the InDet tracks is only used after this E_{T} cut. Using a fast two-stage track-finding (FTF) algorithm, tracks associated to the calorimeter $\tau_{\text{had-vis}}$ candidate are reconstructed. Candidate events only pass if there are between 1 and 3 tracks in the core region with $\Delta R < 0.2$ to the direction of the calorimeter cluster and at most one track in the isolation region $0.2 < \Delta R < 0.4$.

The remaining events are processed with more time-consuming and accurate algorithms, and the track reconstruction is repeated with a more precise algorithm named "EF" [103] after the "event filter" stage of the three-level trigger system

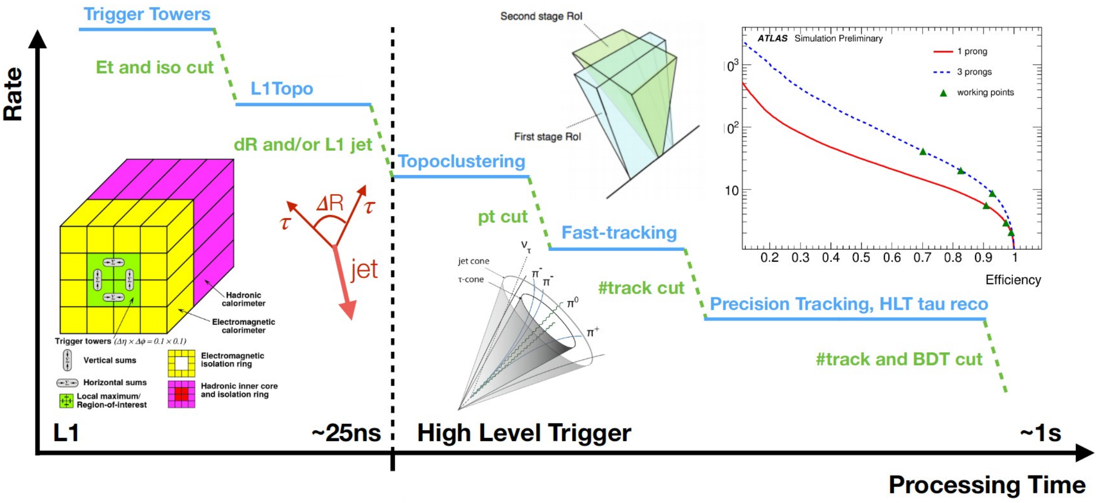

Figure 6.1: Graphical representation of the composition of an ATLAS τ-trigger chain [102].

of Run 1, for which it was originally developed. At the start of Run 2, the candidates were required to also have 1-3 associated core EF tracks and no more than one isolation EF track. These trigger chains were named “tracktwo” triggers. Throughout Run 2, alternative chains named “tracktwoEF” were introduced that omitted the cut on the FTF tracks but kept the EF track requirement.

The last step of the trigger chain is the identification. Following the development in the offline $\tau_{\text{had-vis}}$ reconstruction, a BDT was used for this and later replaced with an RNN. The tracktwo and tracktwoEF triggers use the medium working point of the BDT ID, which consists of two separately trained BDTs for 1-prong and multi-prong candidates, where the multi-prong BDT was used if 2 or 3 core EF tracks were found. This ID method is named “medium1.” The triggers that use the RNN ID skip the cut on FTF tracks and pass events with 0-3 core EF tracks, which is named the “tracktwoMVA” track selection. Additionally, they are the only triggers to utilize the BRT for energy calibration, as it was developed late in Run 2. The RNN is trained separately for the cases of 0, 1 and 2 or 3 core EF tracks, and since for the default triggers only the medium working point of the RNN is used, its application is marked with the expression “mediumRNN.”

The naming scheme of τ-trigger chains summarizes these event processing steps. The names have the form:

$$\text{HLTtauXX\_medium}\{1,\ \text{RNN}\}\text{\_tracktwo(EF, MVA)\_L1TAUYY(I, IM)}\ .$$

The values XX(YY) give the HLT(L1) energy requirement in units of GeV. The “medium” is appended either by “1” or “RNN” depending on the applied ID algorithm, and either “EF” or “MVA” is added to the part “tracktwo” if no cut is placed on the FTF tracks. Finally, the ending “I” or “IM” is added if an isolation criterion is applied to the ECal energy distribution at L1. The “IM” variant is a slightly tighter version of the “I” isolation criterion, which is used to reduce the rate of accepted QCD jets.

6.2 Event Selection

For the measurement of the efficiency of τ-trigger chains, a tag-and-probe strategy is applied. It is based on the assumption that the efficiency of the τ trigger is only dependent on the properties of specific $\tau_{\text{had-vis}}$ candidates and that there are only negligible correlations to the other objects that are present in an event. The ATLAS τ-trigger group conducts two orthogonal analyses to measure the efficiencies of their triggers which are combined into a single efficiency estimate using the “best linear unbiased estimater” (BLUE) method [104]. The first analysis selects $Z \to \tau\tau$ events and is most sensitive to lower-momentum $\tau_{\text{had-vis}}$ candidates, while the second one selects $t\bar{t}$ events with $\tau_{\text{had-vis}}$ candidates in the final state and is more sensitive at higher momenta. The following sections will focus on the $Z \to \tau\tau$ analysis, with the signal process $Z \to \tau\tau \to \mu\tau_{\text{had-vis}}3\nu$ that is illustrated in Fig. 6.2.

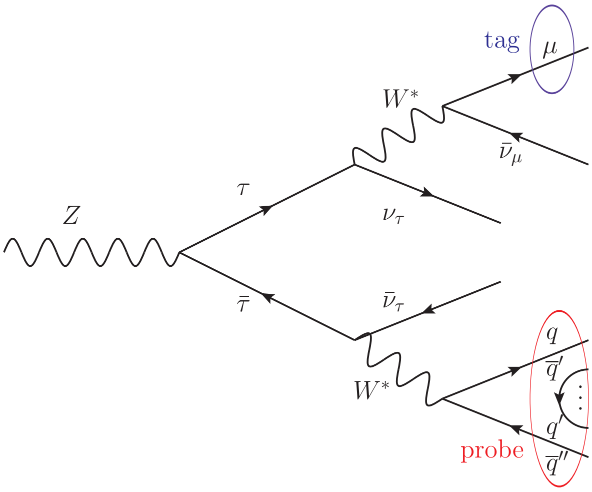

Figure 6.2: Feynman diagram of the $Z \to \tau\tau \to \mu\tau_{\text{had-vis}}3\nu$ decay chain, indicating the tagging muon and the $\tau_{\text{had-vis}}$ candidate that is to be probed.

The purpose of the tag-and-probe selection is to acquire a large and pure set of events containing $\tau_{\text{had-vis}}$ objects without biasing the selection of these objects, thus avoiding cuts that are correlated with the τ-trigger algorithms. Therefore, the events are selected with a muon trigger. Furthermore, the absence of any other "light leptons" (= muons or electrons, symbol ℓ) is required, to increase the contribution from the $Z \to \tau\tau \to \mu\tau_{\text{had-vis}}3\nu$ process.

The analysis is conducted with the 135.7 fb^{-1} recorded by ATLAS in 2016, 2017 and 2018. In order to compare the observed data distributions to the SM prediction, the analysis relies on MC simulated event samples. These samples are summarized in Tab. 6.1.

The event preselection contains cuts on the reconstructed objects that are applied in all analysis regions. These cuts are necessitated by detector acceptance, energy thresholds at trigger level and the requirement of orthogonality to the complementary measurement using $t\bar{t}$ events, and are listed in Tab. 6.2. As the analysis is repeated applying different ID requirements on the $\tau_{\text{had-vis}}$ candidates, no specific ID working point can be given. But in order to give a coherent picture, all results shown in this chapter are obtained applying the loose RNN-based ID criterion unless explicitly stated otherwise.

All events in this analysis are selected by a combination of two muon triggers [118]. The first one targets muons with lower p_{T} and requires a value of

Table 6.1: Summary of simulated event samples used in the τ-trigger efficiency measurement using $Z \to \tau\tau$ events. The label "V+jets" covers both W- and Z-boson production, including the signal, while the label "Top" summarizes sample information for $t\bar{t}$ and single-t production [65, 105–117].

Process	Generator		PDF set		Tune	Order
	ME	PS	ME	PS		
V+jets	Powheg	Pythia 8	CT10	CTEQ6L1	AZNLO	NLO
Top	Powheg	Pythia 8	NNPDF3.0nlo	NNPDF2.3lo	A14	NLO

Table 6.2: Preselection cuts for the $Z \to \tau\tau$ trigger efficiency measurement, applied at all stages of the analysis.

Muons	$\tau_{\text{had-vis}}$	Jets
Medium ID	Varying ID	$N_{\text{b-jets}} = 0$
Trigger matched	$\lvert\eta\rvert < 2.47$	
$\lvert\eta\rvert < 2.5$	$\lvert\eta\rvert \notin [1.35, 1.52]$	
$p_{\text{T}} > 28$ GeV	$p_{\text{T}} > 25$ GeV	

26 GeV at the HLT level. It also imposes an isolation requirement on the muon candidates. The second trigger has a higher p_{T} threshold of 50 GeV and omits the isolation requirement. The reasons for not requiring isolation are that there are fewer background objects that can mimic high-p_{T} muons and that highly energetic muons can emit enough particles to spoil their isolation by themselves. This reduces the efficiency of the isolation requirement at higher energies, and it is therefore not used. An event is required to pass either the 26 GeV or the 50 GeV muon trigger to be included in this analysis.

Distributions of different kinematic variables at preselection, requiring the $\tau_{\text{had-vis}}$ candidate to fulfill the loose RNN-based ID working point, are shown in Fig. 6.3. These show only the distributions observed in data and the predicted contributions from the MC samples listed in Tab. 6.1. Consequently, there is no estimation of the contribution from QCD multi-jet events where both the muon and the $\tau_{\text{had-vis}}$ are faked by QCD jets. Thus, an underestimation of data yields over the prediction is expected at this stage, which can be accounted mostly to the missing QCD estimate. The transverse mass m_{T} shown in Fig. 6.3(a) is defined as

$$m_{\mathrm{T}}(\mu, E_{\mathrm{T}}^{\mathrm{miss}}) = \sqrt{2 p_{\mathrm{T}}(\mu) E_{\mathrm{T}}^{\mathrm{miss}} \left(1 - \cos(\Delta\phi(\mu, E_{\mathrm{T}}^{\mathrm{miss}}))\right)} \, ,$$

and the sum of the azimuthal angles of the muon and the $\tau_{\text{had-vis}}$ with the missing energy shown in Fig. 6.3(c) is calculated as

$$\sum \cos\left(\Delta\phi\right) = \cos(\Delta\phi(\mu, E_{\mathrm{T}}^{\mathrm{miss}})) + \cos(\Delta\phi(\tau_{\text{had-vis}}, E_{\mathrm{T}}^{\mathrm{miss}})) \, .$$

For the $Z \to \tau\tau$ and top-quark samples, a geometrical truth matching is applied as follows: If the reconstructed $\tau_{\text{had-vis}}$ candidate cannot be matched to a truth-level $\tau_{\text{had-vis}}$ object, it is considered a “fake” event (red and orange histograms), otherwise it is counted as a signal event containing a true $\tau_{\text{had-vis}}$ object (blue and teal histograms).

The distributions shown in Fig. 6.3 can be used to separate signal and background contributions and motivate the final event selection for the trigger efficiency measurement. In addition to the shown kinematic distributions, the product of the electric charges of the muon and the $\tau_{\text{had-vis}}$ candidate as well as the isolation of the muon are considered. As the signal process $Z \to \tau\tau$ at leading order should always produce muons and $\tau_{\text{had-vis}}$ candidates of opposite charge, adding this requirement helps increase the relative signal contribution. Non-isolated muons are often produced within QCD jets, while the muons in the signal process are more likely to be isolated.

A signal region (SR) enriched in $Z \to \tau\tau$ events is defined, as well as three control regions (CRs) enriched in either $W \to \mu\nu$ or QCD multi-jet production events, the two largest background contributions. The definitions of the SR, same-sign (SS) CR, the QCD CR and the W+jets CR are shown in Tab. 6.3.

6.3 Background Estimation

The main backgrounds to this measurement are QCD multi-jet production and $W \to \mu\nu$ + jets where a jet is misidentified as $\tau_{\text{had-vis}}$ ($j \to \tau_{\text{had-vis}}$). In a small fraction of events, the selected probe is a light lepton ($\ell \to \tau_{\text{had-vis}}$). A combination of data-driven and simulation-based approaches exploiting the strong charge-correlation between the tag muon and the $\tau_{\text{had-vis}}$ probe is used to model these backgrounds. The background estimation separates events where the muon and the $\tau_{\text{had-vis}}$ candidate have the same charge (“same-sign”, SS) and those where they are of opposite charge (“opposite-sign”, OS). As the signal process is expected to be mainly present in OS events, the signal region (SR) where the τ-trigger efficiency is measured contains only OS events.

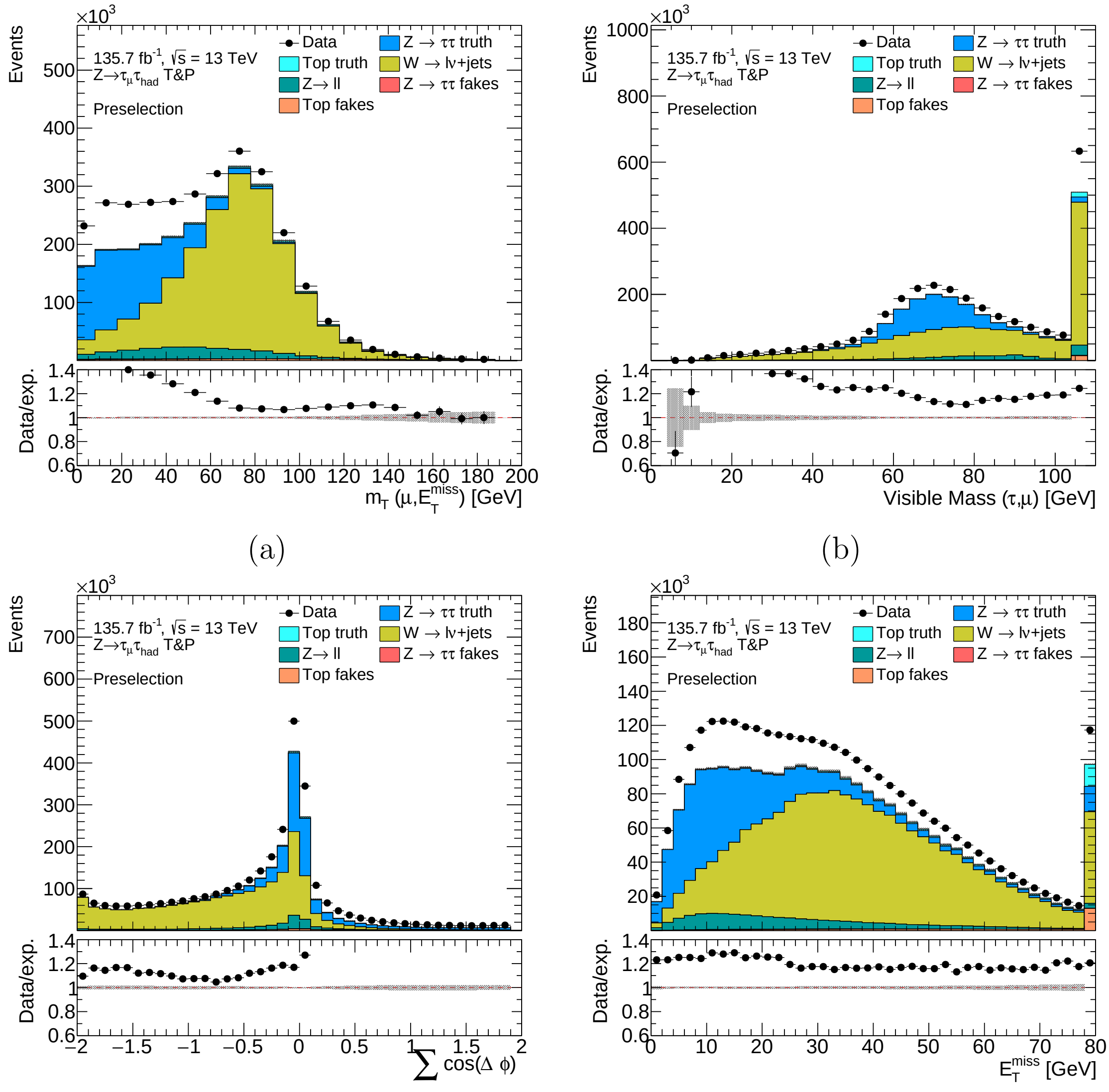

(a) (b)

(c) (d)

Figure 6.3: Distribution of (a) $m_{\mathrm{T}}(\mu, E_{\mathrm{T}}^{\mathrm{miss}})$, (b) $m_{\mathrm{vis}}(\mu, \tau_{\text{had-vis}})$, (c) $\sum \cos(\Delta\phi)$ and (d) $E_{\mathrm{T}}^{\mathrm{miss}}$ after the preselection cuts of the $Z \to \tau\tau$ trigger efficiency measurement. The grey band indicates the statistical uncertainty on the yield prediction.

The full estimate of the background in the SR can be written as

$$N_{\mathrm{OS}}^{\mathrm{fake}} = R_{\mathrm{OS/SS}} N_{\mathrm{Data}}^{\mathrm{SS}} + N_{Z\to\mu\mu}^{\mathrm{OS-SS}} + N_{W\to\mu\nu}^{\mathrm{OS-SS}} + N_{\mathrm{top}}^{\mathrm{OS-SS}} \,,$$

where each term is detailed in the following. The “OS−SS” superscript indicates

Table 6.3: Selection cuts applied after the preselection step to define the signal and control regions of the $Z \to \tau\tau$ trigger efficiency measurement. A dash means that no cut is placed.

Variable	SR	SS CR	QCD CR	W+jets CR
Muon isolation	Yes	Yes	Inverted	Yes
$q(\mu) \cdot q(\tau_{\text{had-vis}})$	-1	$+1$	-1	-1
$m_{\text{T}}(\mu, E_{\text{T}}^{\text{miss}})$ [GeV]	< 50	< 50	< 50	> 60
$m_{\text{vis}}(\mu, \tau_{\text{had-vis}})$ [GeV]	$\in [45, 80]$	$\in [45, 80]$	$\in [45, 80]$	-
$\sum \cos(\Delta\phi)$	> -0.5	> -0.5	> -0.5	-
$E_{\text{T}}^{\text{miss}}$ [GeV]	-	-	-	> 20

the subtraction that is used to determine the charge-asymmetric contribution of the various background processes.

The term $R_{\text{OS/SS}} N_{\text{Data}}^{\text{SS}}$ accounts for the multi-jet background and the charge-symmetric components of the other background processes, such as W+jets, $Z \to \mu\mu$ + jets and processes involving t quarks, mainly $t\bar{t}$ production. It is modelled using data in the SS control region where the charge-product between the tag and the probe is positive and a negligible $Z \to \tau\tau \to \mu\tau_{\text{had-vis}}3\nu$ contamination is found, which is subtracted from the data to construct the final template of the charge-symmetric background estimate. As the expected number of background events depends on the charge-product between the tag and the probe, the normalization of the SS data is corrected by the $R_{\text{OS/SS}}$ factor. This factor is measured in a multi-jet enriched control region defined by inverting the isolation requirement around the tag muon. The $R_{\text{OS/SS}}$ factor is the ratio of the number of events in OS and SS data, and is parametrized using the track multiplicity of the $\tau_{\text{had-vis}}$ candidate and the ID criterion applied to it, as well as the muon p_{T}, and it is independently measured with and without applying τ triggers. Example distributions in the QCD CR are shown in Fig. 6.4, showing the $p_{\text{T}}(\mu)$ distributions needed to calculate the $R_{\text{OS/SS}}$ factors for 1-prong $\tau_{\text{had-vis}}$ candidate events without an applied τ-lepton trigger. The corresponding $p_{\text{T}}(\tau_{\text{had-vis}})$ 1-prong template distribution from the SS CR is shown in Fig. 6.5, along with the 3-prong template distribution.

The "OS−SS" terms account for the charge-asymmetric component of the backgrounds, which are added to the charge-symmetric component included in the $R_{\text{OS/SS}} N_{\text{Data}}^{\text{SS}}$ term. They are estimated as

$$N^{\text{OS}-\text{SS}} = k_W^{\text{OS}} N_{j \to \tau_{\text{had-vis}}}^{\text{OS}} - k_W^{\text{SS}} R_{\text{OS/SS}} N_{j \to \tau_{\text{had-vis}}}^{\text{SS}} + N_{\ell \to \tau_{\text{had-vis}}}^{\text{OS}} - R_{\text{OS/SS}} N_{\ell \to \tau_{\text{had-vis}}}^{\text{SS}} ,$$

where $N^{\text{OS}-\text{SS}} \in \{N_{Z \to \mu\mu}^{\text{OS}-\text{SS}}, N_{W \to \mu\nu}^{\text{OS}-\text{SS}}, N_{\text{top}}^{\text{OS}-\text{SS}}\}$. The k_W corrections account for

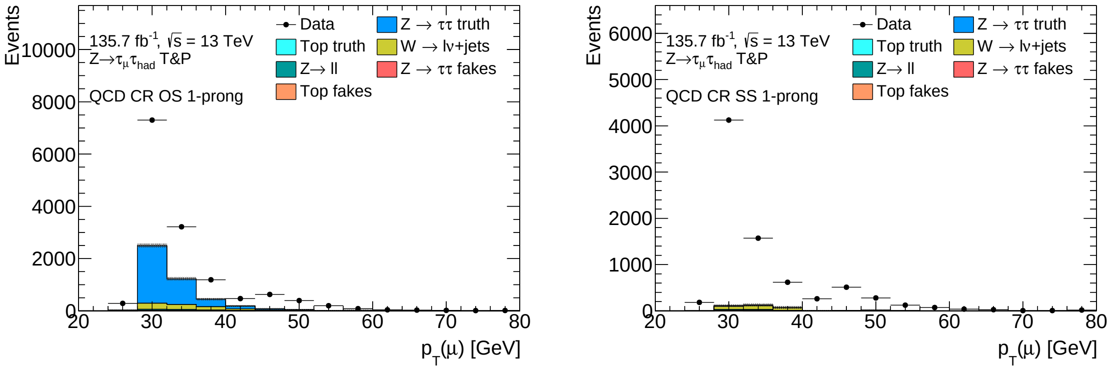

(a) (b)

Figure 6.4: Distribution of $p_{\mathrm{T}}(\mu)$ in the (a) OS and (b) SS QCD CRs for 1-prong $\tau_{\text{had-vis}}$ candidates. The ratio of these distributions is used to extract the factor $R_{\mathrm{OS/SS}}$ which scales the charge-symmetric background template from the SS CR to obtain the SR prediction.

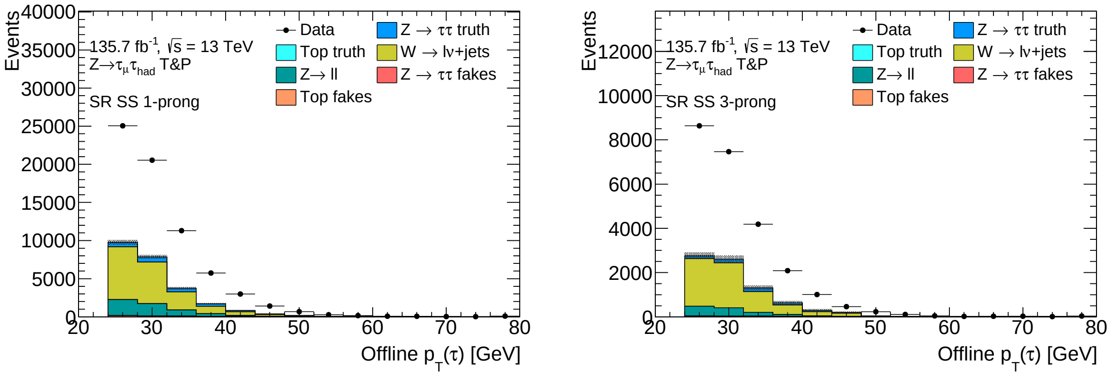

(a) (b)

Figure 6.5: Distribution of $p_{\mathrm{T}}(\tau_{\text{had-vis}})$ in the SS CR for (a) 1-prong and (b) 3-prong candidates. These distributions are used as templates for the estimation of charge-symmetric background contributions in the SR.

possible mismodellings of the fraction of jets that are mislabelled as $\tau_{\text{had-vis}}$ objects ("fake-rate") in simulation, and are measured in the W+jets CR defined in Tab. 6.3. This correction is the ratio between the observed data and the $W \rightarrow \mu\nu$+jets and top-quark production events expected from simulation. As an approximation, all $W \rightarrow \mu\nu$+jets and top-quark production events without truth-matched $\tau_{\text{had-vis}}$ object are treated as $j \to \tau_{\text{had-vis}}$ backgrounds, while all $Z \to \mu\mu$ events are treated as $\ell \to \tau_{\text{had-vis}}$ backgrounds. For the simulated charge-asymmetric component of the $\ell \to \tau_{\text{had-vis}}$ background, no data-driven correction is applied as this contribution is found to be small. The k_W factors are parametrized using the track multiplicity of the $\tau_{\text{had-vis}}$ candidate, the ID criterion applied to it and $p_{\text{T}}(\tau)$ as well as $q(\mu) \cdot q(\tau)$, and is independently measured with and without applying τ triggers. The calculation is illustrated in Fig. 6.6, which shows the $p_{\text{T}}(\tau_{\text{had-vis}})$ distributions used to calculate the k_W factors for OS and SS 3-prong $\tau_{\text{had-vis}}$ candidate events. The obtained k_W and $R_{\text{OS/SS}}$ factors together with their statistical uncertainties are given in Tab. 6.4.

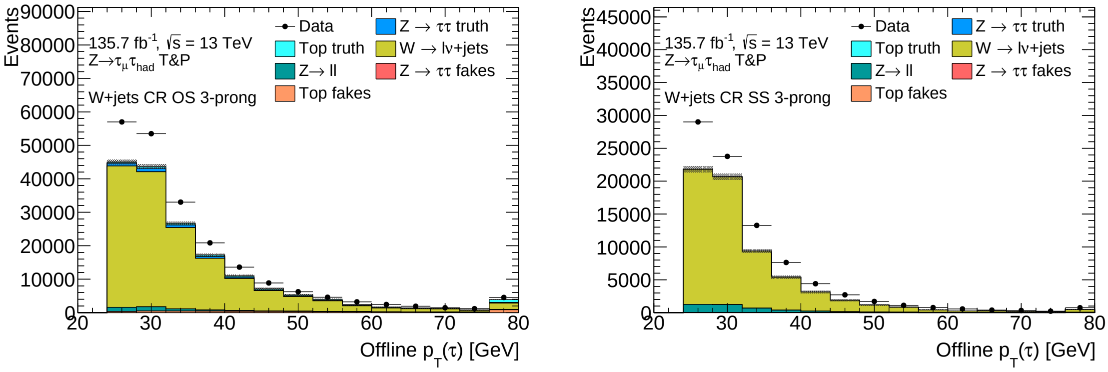

(a)

(b)

Figure 6.6: Distributions of $p_{\text{T}}(\tau_{\text{had-vis}})$ in the (a) OS and (b) SS QCD CRs for 3-prong $\tau_{\text{had-vis}}$ candidates. The factor needed to scale the sum of the W+jets and fake t-quark contribution such that the normalizations of data and MC processes coincide is named k_W.

The contribution from top-quark production events with true $\tau_{\text{had-vis}}$ objects is estimated from simulation, and is also excluded from the top-quark production background contributions and is subtracted from data in all the control regions. The contribution of $Z \to \tau\tau \to \mu\tau_{\text{had-vis}}3\nu$ events where the selected $\tau_{\text{had-vis}}$ probe is a misidentified jet is found to be negligible, and is added to the $Z \to \ell\ell$ contribution in plots of the SR. The resulting modelling is displayed in Fig. 6.7, which shows the $p_{\text{T}}(\tau_{\text{had-vis}})$ distribution in the SR, separated in 1-prong and 3-prong $\tau_{\text{had-vis}}$ candidates.

A discrepancy is found at values of $p_{\text{T}}(\tau_{\text{had-vis}})$ above 50 GeV. This was found to be caused by events with $\Delta\phi(\mu, \tau_{\text{had-vis}}) < 2.4$, as evidenced by the distributions shown in Fig. 6.8.

The low values of $|\Delta\phi(\tau_{\text{had-vis}}, \mu)|$ contain a disagreement between data and

Table 6.4: Overview of the k_W and $R_{\mathrm{OS/SS}}$ factors derived for the SR background estimation. The separating p_T values are $p_\mathrm{T}(\tau_{\text{had-vis}}) = 35$ GeV for k_W and $p_\mathrm{T}(\mu) = 50$ GeV for $R_{\mathrm{OS/SS}}$. The number in parentheses is the statistical uncertainty on the last given digit.

Factor	without τ-lepton trigger				with τ-lepton trigger			
	1-prong		3-prong		1-prong		3-prong	
	low-p_T	high-p_T	low-p_T	high-p_T	low-p_T	high-p_T	low-p_T	high-p_T
$R_{\mathrm{OS/SS}}$	1.23(3)	1.28(5)	1.40(5)	1.37(8)	1.25(4)	1.27(7)	1.43(9)	1.3(1)
k_W^{OS}	1.14(1)	1.12(1)	1.26(1)	1.26(2)	1.15(1)	1.15(1)	1.25(3)	1.32(2)
k_W^{SS}	1.23(1)	1.36(2)	1.29(2)	1.49(4)	1.31(2)	1.43(3)	1.29(5)	1.62(6)

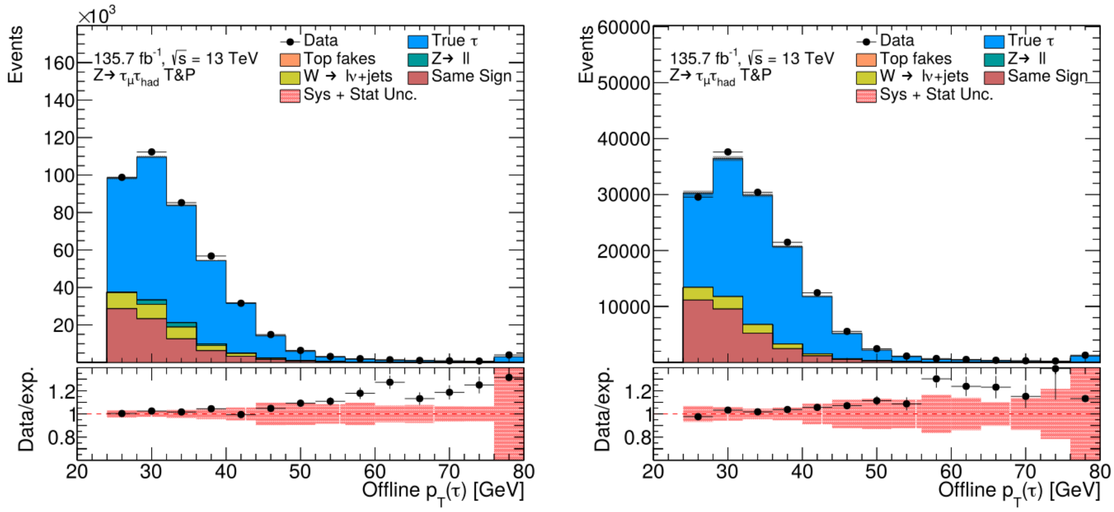

(a)

(b)

Figure 6.7: Distribution of the p_T of the $\tau_{\text{had-vis}}$ candidate in the SR applying the loose RNN-based ID working point, for (a) 1-prong and (b) 3-prong candidates. The red band indicates statistical as well as systematic uncertainties on the predicted distributions.

prediction in Fig. 6.8a, and removing these events leads to a better agreement between data and prediction at high $p_\mathrm{T}(\tau_{\text{had-vis}})$ values. Despite this observation, the cut $\Delta\phi(\mu, \tau_{\text{had-vis}}) > 2.4$ was not applied for the final measurement because the obtained efficiencies were found not to be biased by these events. Therefore,

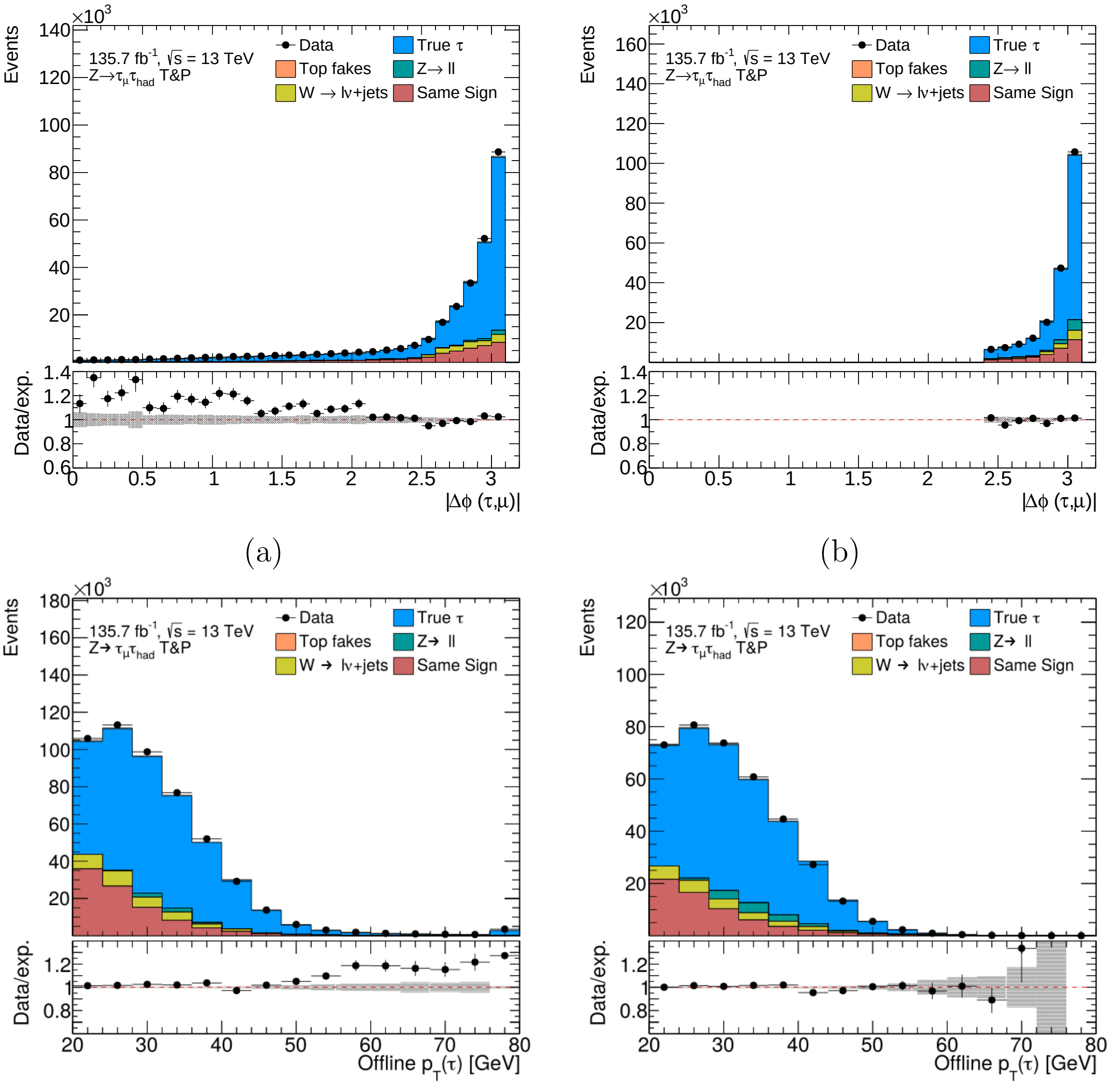

(a) (b)

(c) (d)

Figure 6.8: Comparison of $\sum \cos(\Delta\phi)$ and $p_{\mathrm{T}}(\tau_{\text{had-vis}})$ distributions in the SR for 1-prong $\tau_{\text{had-vis}}$ candidate events for (a & c) the default selection and (b & d) when adding the cuts $\sum \cos(\Delta\phi) > -0.15$ and $|\Delta\phi(\mu, \tau_{\text{had-vis}})| > 2.4$ to the selection, requiring medium RNN-based ID for the $\tau_{\text{had-vis}}$ candidate. The grey band indicates the statistical uncertainty on the prediction.

in order to keep the available dataset as large as possible, the baseline selection was kept.

6.4 Systematic Uncertainties

In this section, the estimation of systematic uncertainties on the estimated event yields and subsequently the trigger efficiencies is discussed. The sources of these uncertainties can be separated into two groups. The first are the uncertainties on the object and event reconstruction as well as the energy calibration of objects, also referred to as experimental uncertainties in the following. The second uncertainty group covers the uncertainties on the applied background estimation techniques.

The impact of systematic uncertainties on the signal processes containing true $\tau_{\text{had-vis}}$ objects on the measured efficiencies was found to be negligible compared to the background estimation uncertainties. Therefore, these uncertainties are not evaluated.

The impact of an uncertainty is quantified by varying the predicted yields according to the given uncertainty and computing the difference between the variation and the nominal result.

6.4.1 Experimental Uncertainties

The experimental uncertainties are estimated separately for the different physics objects utilized in the analysis. Apart from muons and $\tau_{\text{had-vis}}$ candidates, the uncertainties related to jets and $E_{\text{T}}^{\text{miss}}$ must also be taken into account, since a cut on the number of b-tagged jets as well as multiple cuts involving $E_{\text{T}}^{\text{miss}}$ are placed.

Muon-related uncertainties. The efficiencies for trigger selection, offline reconstruction and identification of muon objects are measured in $Z/\gamma^* \to \mu\mu$ and $J/\psi \to \mu\mu$ events [88]. The derived correction factors for MC are varied within their respective uncertainties to assess their impact on the efficiency measurement. Moreover, the muon momentum calibration measurement is also conducted in $Z/\gamma^* \to \mu\mu$ and $J/\psi \to \mu\mu$ events. Based on this measurement, scale and resolution uncertainties are applied. Finally, uncertainties on the isolation efficiency correction factors, derived in $Z \to \mu\mu$ events, are applied.

$\tau_{\text{had-vis}}$-related uncertainties. Uncertainties on the offline identification efficiency for $\tau_{\text{had-vis}}$ candidates and their momentum scale, measured in $Z \to \tau\tau$ events [97], are applied. Additionally, uncertainties on the reconstruction efficiency are considered.

Jet-related uncertainties. Numerous sources of uncertainty are considered for the jet calibration procedure outlined in Sec. 5.3. For the η-intercalibration, a technique with which the calibration derived for central-η jets is extrapolated to high-η jets, five variations are applied. Eight additional variations are applied for the energy scale and energy resolution estimation of jets, respectively. The uncertainty on the pile-up corrections applied during calibration is covered with four variations. To account for the different detector responses for jets initiated by quarks and gluons as well as the limited knowledge of the jet flavour composition, three more variations of the calibration are introduced. The modelling of "punch-through" jets, which pass through the calorimeter system without depositing all their energy, and jets initiated by very high-p_{T} partons requires the inclusion of one additional variation each. The efficiency of the b-jet classification is assigned eleven sources of uncertainty. Finally, one variation each is included for the efficiencies of the JVT and fJVT cuts.

For 2018 data-taking, the calibration of energy deposited in the tile calorimeter was updated [119]. Therefore, an additional systematic variation limited to 2018 data is taken into account.

$E_{\mathrm{T}}^{\mathrm{miss}}$-related uncertainties. The estimation of $E_{\mathrm{T}}^{\mathrm{miss}}$ is separated into hard and soft terms, as described in Sec. 5.5. The variations on the reconstructed objects in the event are propagated into $E_{\mathrm{T}}^{\mathrm{miss}}$ variations through changes of the hard term. The soft term, which contributes exclusively to the $E_{\mathrm{T}}^{\mathrm{miss}}$ measurement, is assigned three sources of uncertainty, measured in events with one Z boson and one jet in the final state [101]. The scale of the soft term projected on the direction of the hard contribution, as well as the resolution of the soft term measured parallel or perpendicular to the direction of the hard contribution are varied.

Pile-up reweighting uncertainties. In order to have compatible pile-up activity in data and simulation, a scaling factor is applied to the number of pile-up interactions observed in data. This is necessary since the current MC simulation of the effect of a given number of pile-up interactions on the event reconstruction is too large. The scaling factor for the number of interactions is varied within its uncertainty to assess the effect on the measurement.

Luminosity-related uncertainties. The uncertainty on the measured integrated luminosity of data included in this analysis is applied as an uncertainty on the measurement, affecting the scaling of the MC simulated events.

6.4.2 Uncertainties on the Background Estimation Method

The assignment of an uncertainty on the estimation of the charge-symmetric background using $R_{\mathrm{OS/SS}}$ and the correction of the charge-asymmetric background using k_W are described in this section.

Two sources of uncertainty regarding the application of k_W factors are considered. The first is the statistical uncertainty on the factor itself, propagated from the uncertainties on the yields in the W+jets CR used to calculate them. The other is an uncertainty on the shape of the $j \to \tau_{\text{had-vis}}$ background contribution. For this, the shapes of the p_{T} distributions of simulated W+jets and t-quark production events are compared to that of data after subtracting all other simulated contributions in the W+jets CR. The resulting ratio is then applied to the signal region contribution of W+jets and top events while keeping the total yield unchanged. This procedure is applied separately for OS and SS events with separately derived shape variations.

Similarly, there are also two sources of uncertainty considered for the $R_{\text{OS/SS}}$ factor. Apart from its statistical uncertainty, a shape variation on the $N^{\text{SS}}_{\text{Data}}$ contribution is applied while keeping its total yield unchanged. The variation is based on the ratio of OS over SS data events in the QCD CR after subtracting all signal contributions expected from simulation.

All described shape variations are independently derived with and without applying a τ trigger, and separately for 1- and 3-prong $\tau_{\text{had-vis}}$ candidates. Like the $R_{\text{OS/SS}}$ and k_W factors themselves, the shape variations are separately derived and applied in a low-p_{T} and a high-p_{T} region. To retain the largest number of events from which to construct the variations, the shape variations are derived using the loose ID criteria but also applied to the medium and tight working points. This is done separately for BDT and RNN ID working points. The impact of the variations on the efficiencies is symmetrized to have a two-sided estimate of the uncertainty. Example p_{T} distribution comparisons illustrating the construction of background shape variations for the 1p k_W factor and the 3p $R_{\text{OS/SS}}$ factor are shown in Fig. 6.9.

Tab. 6.5 reports the observed data and expected signal and background contributions in the SR.

6.5 Efficiency Extraction

In order to estimate the τ-lepton trigger efficiency, a Bayesian approach is used, with an assumed uniform prior probability distribution for efficiencies between 0 and 1. The nominal value of the resulting efficiency ϵ is taken as

$$\epsilon = \frac{N_{\tau_{\text{had-vis}}}(\text{ID \& trigger})}{N_{\tau_{\text{had-vis}}}(\text{ID})} \, .$$

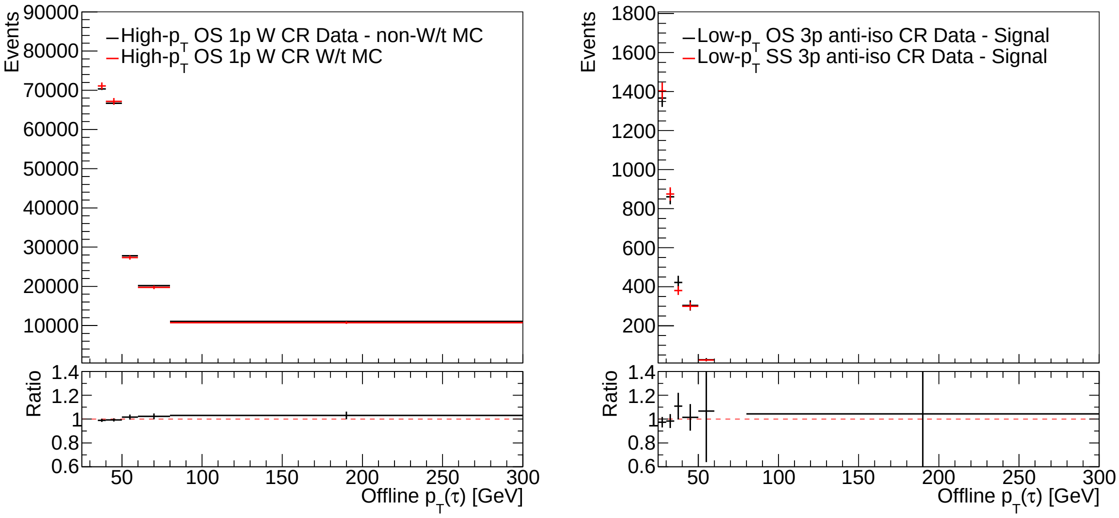

(a) (b)

Figure 6.9: Shape uncertainty construction for (a) the OS k_W factor application for 1-prong $\tau_{\text{had-vis}}$ candidates in the high-p_{T} region ($p_{\text{T}}(\tau_{\text{had-vis}}) > 35$ GeV), and (b) the $R_{\text{OS/SS}}$ factor application for 3-prong $\tau_{\text{had-vis}}$ candidates in the low-p_{T} region ($p_{\text{T}}(\mu) < 50$ GeV). The bottom panels show the ratio between numerator (black) and denominator (red) distributions, which are applied as shape variations. Only statistical uncertainties are shown.

The statistical uncertainty band on ϵ is constructed by determining the shortest interval $[a, b]$ such that

$$\int_a^b P(\epsilon \mid k, N)\, \mathrm{d}\epsilon = 0.683 \,,$$

with the Bayesian posterior probability density P on the efficiency ϵ given k events passing both the trigger and offline ID criteria and N events passing the offline ID criterion.

The efficiency is measured separately in simulation for true hadronically-decaying τ leptons and in data after the subtraction of the estimated backgrounds. The efficiencies are calculated as functions of the p_{T} of the offline $\tau_{\text{had-vis}}$ probe and its track multiplicity. The obtained efficiencies for different versions of the HLT_tau25 trigger, the trigger with the lowest HLT energy threshold, are shown in Fig. 6.10. The measurement for tracktwoEF triggers is restricted to 2018 data, since it was

Table 6.5: Expected and observed yields in the τ-trigger efficiency measurement using $Z \to \tau\tau$ events. Data recorded in 2016, 2017 and 2018 amounting to a total integrated luminosity of 135.7 fb^{-1} are used.

Contribution	Yield (± stat uncert. ± syst uncert.)
$R_{\text{OS/SS}} N^{\text{SS}}_{\text{Data}}$	$110000 \pm 390 \pm 3700$
$W^{\text{OS}-\text{SS}}_{\mu\nu}$	$34660 \pm 1240 \pm 1190$
$Z^{\text{OS}-\text{SS}}_{\mu\mu}$	$5480 \pm 160 \pm 280$
$\text{top}^{\text{OS}-\text{SS}}$	$140 \pm 20 \pm 10$
True $\tau_{\text{had-vis}}$	$401000 \pm 700 \pm 26000$
Total expected	$552000 \pm 1500 \pm 26000$
Data	564261
Data/Exp	1.02
Purity of true $\tau_{\text{had-vis}}$ probes	72.6%

only then introduced and the previously recorded data were not reprocessed emulating these triggers. The same applies to the tracktwoMVA triggers, but they were introduced only after “technical stop 1” (TS1), well within the 2018 data-taking period. Accordingly, only 37.6 fb^{-1} of data can be included in the measurement of their efficiencies. Hence, the efficiency measurement for tracktwo triggers includes the full dataset, but their usage is only recommended before 2018. The tracktwoEF trigger efficiency is derived using the full 2018 dataset but is recommended for use in analyses only for pre-TS1 data. For post-TS1 data, the logical OR between tracktwoEF and tracktwoMVA triggers is recommended. This is done instead of recommending only the use of the tracktwoMVA trigger to ensure consistency in the definition of $\tau_{\text{had-vis}}$ objects, which is important for constructing a background estimate.

The leading, and in almost all cases the only relevant, systematic uncertainty is the shape variation for the $R_{\text{OS/SS}}$ factor. At low p_{T} values, the k_W shape variation can also have a significant impact. All other systematic uncertainties have a negligible impact on the efficiency.

From the efficiency calculation, the SFs intended for correction of simulated events can be obtained. The upward and downward uncertainties on the scale

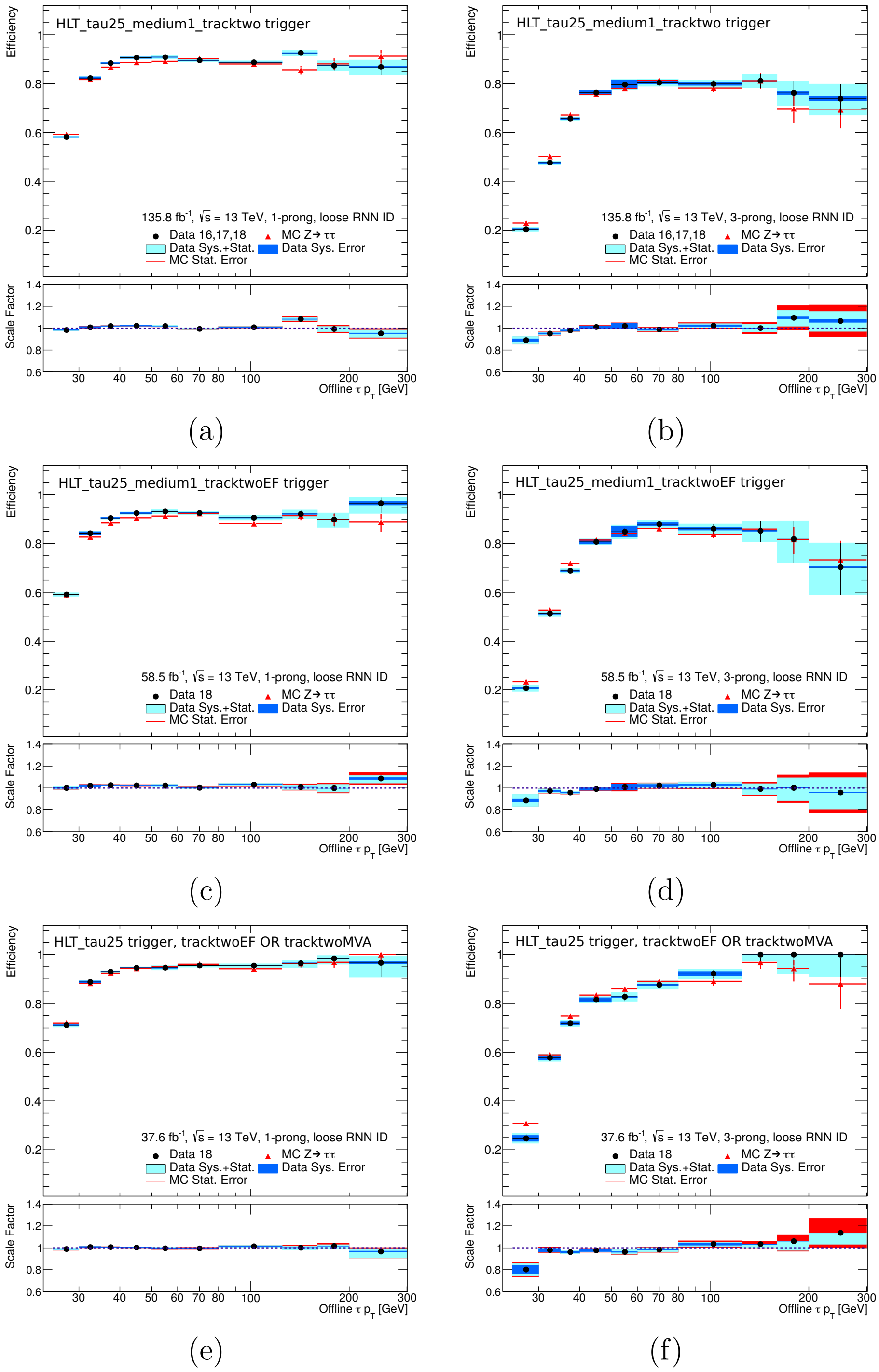

(a) (b)

(c) (d)

(e) (f)

Figure 6.10: Efficiencies on 1- and 3-prong $\tau_{\text{had-vis}}$ objects for three versions of tau25 triggers: The medium1_tracktwo trigger (a & b), the medium1_tracktwoEF trigger (c & d) and the logical OR between the medium1_tracktwoEF and the mediumRNN_tracktwoMVA triggers (e & f). The bottom panels show the "scale factor," the ratio of efficiencies in data and simulation.

factor are given as:

$$\sigma^{\uparrow}_{\mathrm{SF}} = \sqrt{\left(\sigma^{\uparrow}_{\text{Data, stat}}\right)^2 + \left(\sigma^{\uparrow}_{\text{Data, sys}}\right)^2 + \left(\sigma^{\downarrow}_{\text{MC, stat}}\right)^2}$$
$$\sigma^{\downarrow}_{\mathrm{SF}} = \sqrt{\left(\sigma^{\downarrow}_{\text{Data, stat}}\right)^2 + \left(\sigma^{\downarrow}_{\text{Data, sys}}\right)^2 + \left(\sigma^{\uparrow}_{\text{MC, stat}}\right)^2} ,$$

where the arrows indicate the direction of the uncertainty. The usage of the inverse direction of the MC stat uncertainty stems from the fact that it is used as the denominator of the SF, anti-correlating it with the SF.

In most cases, the measured SF is compatible with unity. The region where a discrepancy is most apparent is at low p_T in the 3-prong case for the tau25 trigger. This was found to be primarily due to mismodelling of the L1 selection efficiency. A breakdown of the efficiencies for the individual cuts that comprise the tau25_medium1_tracktwo trigger is shown in Fig. 6.11. This discrepancy can be explained with the distribution of the "tauClus" value of L1TAU ROIs matched to offline $\tau_{\text{had-vis}}$ candidates, which can be seen in Fig. 6.12. This value is the sum of energies measured in the ECal and HCal in the core of the $\tau_{\text{had-vis}}$ candidate energy deposit, and thus describes the energy of the $\tau_{\text{had-vis}}$ candidate reconstructed at L1. The L1TAU12IM item cuts on tauClus > 12 GeV. Fig. 6.12 shows clear modelling problems, especially in the 3-prong case. These modelling problems translate into inconsistencies between efficiencies in data and simulation, and thus into SFs deviating from one.

A final systematic uncertainty was introduced to cover the dependence of the efficiency on the number of pile-up interactions μ. This uncertainty was derived after the derivation of SFs as a function of $p_{\mathrm{T}}(\tau_{\text{had-vis}})$ had been concluded, and the procedure is illustrated in Fig. 6.13. As a first step, the newly derived SFs are applied to the measurement itself, making all deviations between efficiencies in data and MC vanish by construction, when shown as a function of $p_{\mathrm{T}}(\tau_{\text{had-vis}})$. Next, the efficiencies and scale factors are calculated as functions of μ. The resulting residual dependency of the SF on μ after cancelling all $p_{\mathrm{T}}(\tau_{\text{had-vis}})$ dependency is used as a systematic variation.

This procedure was only derived using tau25 triggers and is also used for triggers with higher L1 and HLT energy thresholds. This is done since the μ-dependence mainly comes from the track and ID cuts of the trigger, which do not change between lower- and higher-threshold triggers. Thus, in order to avoid introducing statistical fluctuations, the result obtained using tau25 triggers is also applied to higher-threshold triggers.

A significant deviation from 1 is only seen in the efficiencies of the tracktwo trigger. A reduced μ-dependence for the tracktwoEF and tracktwoMVA triggers recommended to be used in 2018 is expected since these were explicitly designed to

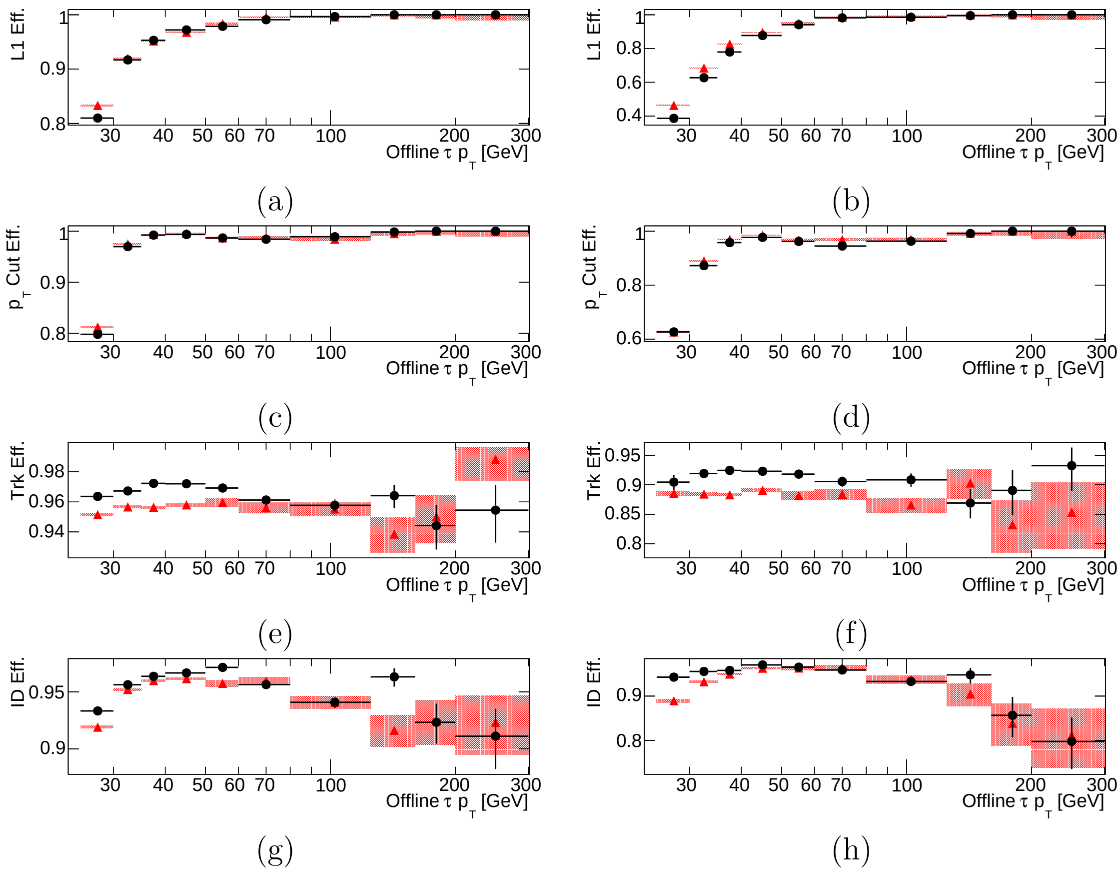

Figure 6.11: Breakdown of the HLTtau25_medium1_tracktwo trigger-chain efficiencies shown in Fig. 6.10 (a) and (b). The efficiencies measured in data are shown using black circles, while the efficiencies in simulated events are indicated using red triangles. Subfigures (a) and (b) show the efficiency of the L1TAU12IM selection. The efficiency of the 25 GeV energy requirement at the HLT is shown in (c) and (d), while the FTF track cut efficiency is shown in (e) and (f). The efficiency of the EF track cut and identification is shown in (g) and (h). As the described cuts are applied successively in the trigger chains, the product of efficiencies shown in the left column corresponds to the 1-prong trigger efficiency shown in Fig. 6.10 (a), while the right column gives the 3-prong efficiencies corresponding to Fig. 6.10 (b).

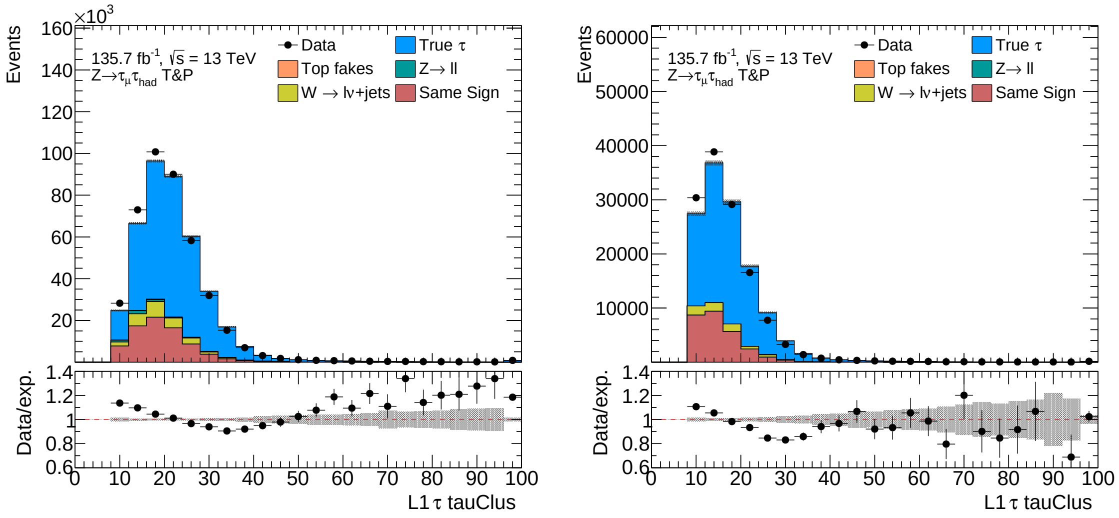

(a)

(b)

Figure 6.12: SR distributions of the L1 tauClus energy distribution for (a) 1-prong and (b) 3-prong $\tau_{\text{had-vis}}$ candidates.

be more robust with respect to pile-up effects. In addition to this, the μ dependence of the SF is negligible in 2016 data, as the spectrum does not often reach values $\mu > 50$ in that year, see Fig. 4.3. As a result, the derived μ variation is only recommended for usage in 2017 data with the tracktwo triggers, using the variation measured in 2016, 2017 and 2018 data.

The obtained trigger efficiencies and scale factors are used within the ATLAS collaboration. All analyses using τ-lepton triggers to select their dataset apply the scale factors as additional event weights to their simulated events containing true $\tau_{\text{had-vis}}$ objects. This is done in order to counteract the difference in τ-trigger efficiency between the simulated and observed events and make them more comparable.

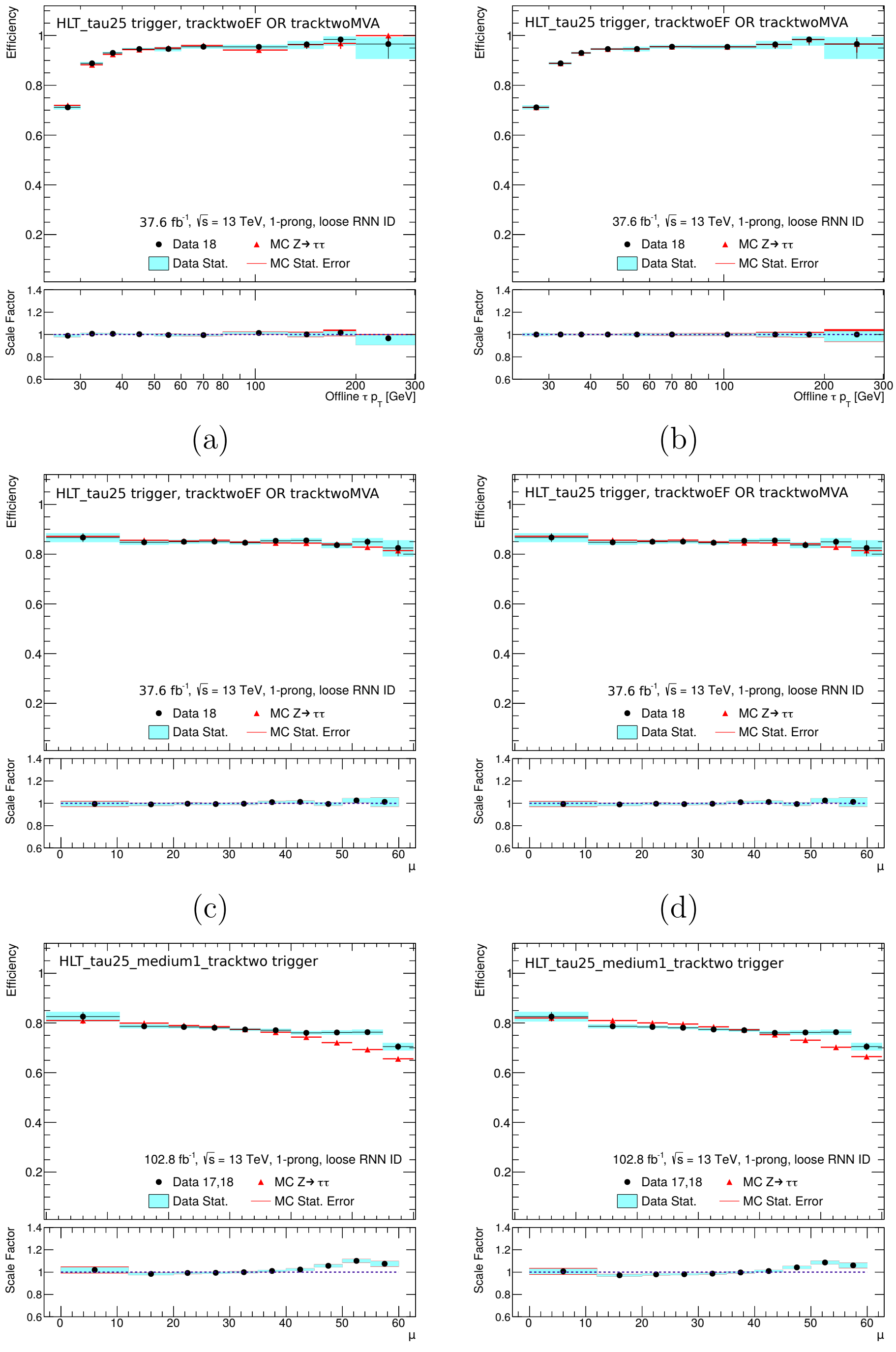

(a) (b) (c) (d) (e) (f)

Figure 6.13: Estimation of the impact of μ on the SFs of tau25 triggers for 1-prong $\tau_{\text{had-vis}}$ objects. Subfigures (a) and (c) show the efficiency for the OR of the medium1_tracktwoEF trigger and the mediumRNN_tracktwoMVA trigger in post-TS1 2018 data, as functions of $p_{\mathrm{T}}(\tau_{\text{had-vis}})$ and μ, respectively. Subfigures (b) and (d) are obtained by repeating the measurement and applying the already determined SFs binned in $p_{\mathrm{T}}(\tau_{\text{had-vis}})$ to true-$\tau_{\text{had-vis}}$ MC events that pass the trigger requirement. Subfigures (e) and (f) show the efficiencies depending on μ without and with applying SFs binned in $p_{\mathrm{T}}(\tau_{\text{had-vis}})$ for the medium1_tracktwo trigger using 2017 and 2018 data.

CHAPTER 7

VBF $H \to \tau\tau$ CP Analysis in the $\tau_{\text{had}}\tau_{\text{had}}$ Final State

This chapter describes a test of CP violation in VBF Higgs-boson production in the $H \to \tau\tau$ decay channel [11]. For this, a direct measurement of the parameter $\tilde{d}$ that introduces CPV to HVV couplings, defined in Sec. 3.3, is performed using the Optimal-Observable method. The analysis is based on the measurement of the Higgs-boson production cross-section in $H \to \tau\tau$ events documented in Ref. [120].

Decays to two τ leptons are classified in four different final states: The $\tau_{\text{lep}}\tau_{\text{lep}}$ same-flavour (SF) channel, the $\tau_{\text{lep}}\tau_{\text{lep}}$ different-flavour (DF) channel, the $\tau_{\text{lep}}\tau_{\text{had}}$ channel and the $\tau_{\text{had}}\tau_{\text{had}}$ channel. The subscript "lep" or "had" specifies whether the τ lepton decays leptonically or hadronically, and the specification same-flavour or different-flavour compares the flavours (electron or muon) of the two final-state leptons in the $\tau_{\text{lep}}\tau_{\text{lep}}$ channel. By combining the branching fractions shown in Fig. 2.6a, the relative branching fractions in Fig. 7.1 are obtained for these four channels.

While the signal processes are the same in the four channels, the background composition varies greatly depending on the investigated decay channel. Therefore, they are treated separately. The following sections detail the analysis of $\tau_{\text{had}}\tau_{\text{had}}$ events and also describe the statistical combination of the four channels.

7.1 Simulated Event Samples

To estimate the contributions of signal and background processes to the observed data, the analysis relies on MC simulated samples. This section gives an overview of the used samples, which is summarized in Tab. 7.1.

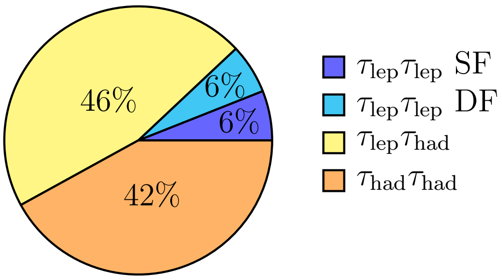

Figure 7.1: Branching fractions of di-τ final states into the four analysis channels of the VBF $H \to \tau\tau$ CP analysis.

Gluon-gluon fusion Higgs-boson production events are generated at NLO accuracy in QCD using the Powheg NNLOPS program [105–107, 121, 122]. The events are reweighted to NNLO precision using the Higgs-boson rapidity spectra of Hj-MiNLO [123–125] and HNNLO [126]. The PDF4LHC15nnlo PDF set [127] is used for the matrix element calculation and the AZNLO tune [111] with the CTEQ6L1 PDF set [110] is used within Pythia 8 [113]. The gluon fusion prediction from the Monte Carlo samples is normalized to the N^{3}LO cross-section in QCD plus electroweak corrections at NLO [26–31].

Vector-boson fusion events are generated at NLO using Powheg [128] and the NNPDF3.0nlo PDF set [114]. For the parton showering and the underlying event modelling, Pythia 8 is used with the CTEQ6L1 PDF set and the AZNLO tune. The events are reweighted to the NNLO cross-section in QCD plus electroweak corrections at NLO [34–36].

Higgs-boson production in association with a vector boson is simulated using Powheg and interfaced with Pythia 8 for the simulation of parton showering and non-perturbative effects. The Powheg prediction is accurate to NLO for the VH plus one jet production. The PDF4LHC15nlo PDF set [127] and the AZNLO tune of Pythia 8 are used. The Monte Carlo prediction is normalized to cross-sections calculated at NNLO in QCD with NLO electroweak corrections [37–40].

The normalization of the ggF, VBF and VH samples accounts for the decay branching ratio calculated with HDECAY [24] and PROPHECY4F [25]. In addition to the described samples, signal events are also generated with Herwig 7 [129, 130] to evaluate the impact of the choice of parton shower on the result.

To simulate the production of Higgs bosons in association with a pair of top quarks at leading order, MadGraph5_aMC@NLO [66] is used together with the NNPDF3.0lo PDF set [114]. For parton showering and the simulation of the underlying event, Pythia 8 is used with the A14 tune [116] and the NNPDF2.3lo PDF set [115]. The total prediction is normalized to the NLO cross-section in

QCD including NLO electroweak corrections [41–46].

The V+jets and di-boson production is simulated with SHERPA [131] using NLO matrix elements for up to two (one for di-boson) additional partons, and LO matrix elements for up to four (three) partons calculated with Comix [132] and OpenLoops [133–135]. They are matched with the SHERPA parton shower [136] using the MEPS@NLO prescription [137–140] with a set of tuned parameters developed by the SHERPA authors. The NNPDF3.0nnlo set of PDFs [114] is used and the V+jets samples are normalized to an NNLO prediction [141]. An additional Z+jets sample generated with MadGraph5_aMC@NLO and PYTHIA 8 was used to evaluate the impact of the choice of parton shower on the predicted yield. The electroweak production of Z with 2 or 3 jets is simulated at LO, but its predicted cross-section has been multiplied by 1.7 to reflect the findings in Ref. [142]. The paper summarizes a differential cross-section measurement of the electroweak Z-boson production process, and the factor 1.7 is the approximate ratio of the result of the analysis and the LO cross-section obtained from SHERPA.

The $t\bar{t}$ and single-top production is simulated at NLO with POWHEG interfaced with PYTHIA 6 [143]. The Perugia2012 tune [144] was used, and the total $t\bar{t}$ prediction is normalized to an NNLO calculation [145]. The decays of bottom and charm hadrons are performed by EvtGen [117].

7.2 Event Selection

For the $\tau_{\text{had}}\tau_{\text{had}}$ channel of the VBF $H \to \tau\tau$ CP analysis, events are required to contain two $\tau_{\text{had-vis}}$ candidates. These need to pass the tight BDT-based ID criterion. To ensure orthogonality to the other analysis channels, which are described in more detail in Ref. [11], events with reconstructed muon or electron candidates are rejected. Moreover, to target VBF production events, the presence of two additional jets with a large separation in η is required. The definition of the inclusive signal region is given in Tab. 7.2. It is based on the VBF signal region selection in Ref. [120].

Only two regions are used for the basic event selection. The cuts on the leading jet in the more inclusive QCD fit region are motivated by the trigger selection. For 2015 data, the di-τ trigger

HLT_tau35_medium1_tracktwo_tau25_medium1_tracktwo_L1TAU20IM_2TAU12IM

is used, which requires a HLT_tau35 and a HLT_tau25 chain to be active in the same event with no overlap between the triggering objects.

Table 7.1: Summary of simulated event samples used in the VBF $H \to \tau\tau$ CP analysis. The symbol l represents all charged leptons, i.e. $l \in \{e, \mu, \tau\}$.

Process	Generator		PDF set		Tune	ME order
	ME	PS	ME	PS		
ggF	Powheg	Pythia 8	PDF4LHC15	CTEQ6L1	AZNLO	N^{3}LO QCD+NLO EWK
VBF	Powheg	Pythia 8	NNPDF3.0	CTEQ6L1	AZNLO	NNLO QCD+NLO EWK
VH	Powheg	Pythia 8	PDF4LHC15	CTEQ6L1	AZNLO	NNLO QCD+NLO EWK
ttH	aMC@NLO	Pythia 8	NNPDF3.0	NNPDF2.3	A14	NLO QCD+NLO EWK
$Z \to ll$	Sherpa		NNPDF3.0		Sherpa	NNLO
$W \to l\nu$	Sherpa		NNPDF3.0		Sherpa	NNLO
EWK $Z \to ll$	Sherpa		NNPDF3.0		Sherpa	LO
EWK $W \to l\nu$	Sherpa		NNPDF3.0		Sherpa	LO
$t\bar{t}$	Powheg	Pythia 6	CT10	CTEQ6L1	Perugia2012	NNLO
Single-top	Powheg	Pythia 6	CT10	CTEQ6L1	Perugia2012	NLO
VV	Sherpa		NNPDF3.0		Sherpa	NLO

Due to the rising instantaneous luminosity, the trigger used in the 2016 data-taking includes a requirement for an additional L1 calorimeter trigger jet with $p_{\mathrm{T}} > 25$ GeV and $|\eta| < 3.2$ (L1_J25). To avoid biases due to turn-on effects of the jet leg of the trigger and to ensure a consistent kinematic selection between the 2015 and 2016 datasets, the leading jet in the event is required to be matched within $\Delta R < 0.4$ with the jet ROI that fulfilled the L1 jet leg of the trigger criteria. In addition, to avoid modelling issues observed in a study similar to the one discussed in Sec. 8.2, the leading jet in the event is required to fulfill offline $p_{\mathrm{T}} > 70$ GeV and $|\eta| < 3.2$ for both 2015 and 2016 data.

Table 7.2: Summary of the event selection for the $\tau_{\text{had}}\tau_{\text{had}}$ channel.

QCD fit region	$N_{\text{leptons}} = 0$, $N_{\tau_{\text{had-vis}}} = 2$ both $\tau_{\text{had-vis}}$: tight BDT ID, OS $p_{\mathrm{T}}(\tau_{\text{had-vis}}) > 40, 30$ GeV both $\tau_{\text{had-vis}}$: 1 or 3 prongs leading jet $p_T > 70$ GeV, $|\eta| < 3.2$ sub-leading jet $p_T > 30$ GeV $E_{\mathrm{T}}^{\text{miss}} > 20$ GeV $0.8 < \Delta R(\tau, \tau) < 2.5$
VBF inclusive region (additional cuts)	$|\Delta\eta(\tau, \tau)| < 1.5$ $m_{jj} > 300$ GeV, $|\Delta\eta(j, j)| > 3$

The two $\tau_{\text{had-vis}}$ candidates are matched to the respective legs of the di-tau trigger using the individual single-τ trigger objects. The offline p_{T} thresholds are chosen such that the selected $\tau_{\text{had-vis}}$ candidate p_{T} lies mostly in the plateau of the respective trigger efficiency curve, beyond the HLT threshold region where the efficiency still rises.

The $E_{\mathrm{T}}^{\text{miss}}$ cut is used to remove signal-free phase-space, as in most $H \to \tau\tau$ events, the produced neutrinos cause a significant $E_{\mathrm{T}}^{\text{miss}}$ to be measured. The cut $\Delta R(\tau, \tau) > 0.8$ is needed to ensure that the jets seeding the $\tau_{\text{had-vis}}$ candidates do not overlap. Since L1TAU ROIs are objects of $\Delta\eta \times \Delta\phi = 0.4 \times 0.4$, these could overlap when loosening this requirement, leading to modelling problems in the simulation. The region with $\Delta R(\tau, \tau) > 2.5$ is excluded since it is dominated by QCD multi-jet events containing jets that fake $\tau_{\text{had-vis}}$ objects.

To define the tighter VBF inclusive region, the cut $|\Delta\eta(\tau, \tau)| < 1.5$ is applied, which removes mostly multi-jet production events, similarly to the $\Delta R(\tau, \tau) > 2.5$ cut. The two last cuts $m_{jj} > 300$ GeV and $|\Delta\eta(j, j)| > 3$ are highly correlated and both increase the relative contribution of VBF events, which characteristically feature two jets with a large difference in η and thus often also a large invariant mass.

7.3 Background Estimation

The MC samples described in Sec. 7.1 are used to estimate all contributions from processes with one or two true final-state $\tau_{\text{had-vis}}$ objects. The contribution from processes with two fake $\tau_{\text{had-vis}}$ candidates, named "Fake" contribution, mainly stems from QCD multi-jet production, but also $W \to qq'$ events. To estimate this contribution, a method named "nOS" (non-opposite sign) was introduced, which inverts the SR criterion $q(\tau_1) \cdot q(\tau_2) = -1$ to construct a region enriched in multi-jet events. Moreover, the track requirement on $\tau_{\text{had-vis}}$ objects is loosened to also accept $\tau_{\text{had-vis}}$ candidates with two associated core tracks. By subtracting all MC contributions in this nOS region from the measured data distribution, a template of the QCD multi-jet contribution is constructed. The event yields in the SR with nOS charge requirement as a function of the MMC-reconstructed di-τ mass, described in Sec. 5.4.3, is shown in Fig. 7.2.

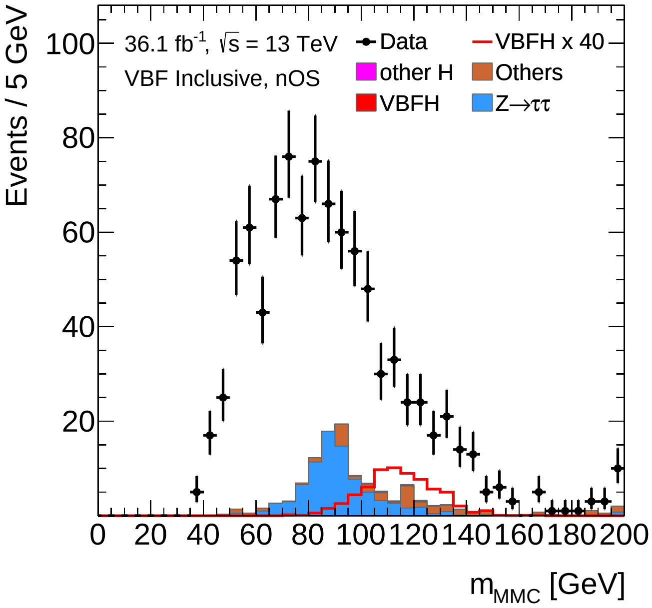

Figure 7.2: Data and MC event distributions in the nOS signal region of the invariant mass $m_{\tau\tau}^{\text{MMC}}$ of the full di-τ system as estimated with the MMC. The difference between data and MC is used as a template to estimate the contribution of QCD multi-jet events in the SR.

In order to validate the modelling of the jet kinematics in the $Z \to \tau\tau$ samples, an analysis region selecting a dataset very pure in $Z \to \ell\ell$ is introduced. The event selection for this validation region is summarized in Tab. 7.3. As the $Z \to \ell\ell$ samples are simulated in the same way as $Z \to \tau\tau$, apart from the Z-boson decay, the modelling of jet-related variables is assumed to be the same in the $Z \to \ell\ell$ region as in the $\tau_{\mathrm{had}}\tau_{\mathrm{had}}$ channel. The modelling of the jet-related variables $C(\tau_1)$, $C(\tau_2)$, m_{jj} and $p_{\mathrm{T}}^{\mathrm{tot}}(E_{\mathrm{T}}^{\mathrm{miss}}, \tau\tau, jj)$, further described in Sec. 7.4, was checked in the validation region. In this study, it was found that the invariant mass m_{jj} of the system of the two jets leading in p_{T} was mismodelled in the simulation. Fig. 7.3 shows the distribution of m_{jj} in the $Z \to \ell\ell$ validation region as well as the ratio between the distributions in data and simulation after scaling the two to the same integral. This shape difference between data and simulation is used as an additional weight on the $Z \to \tau\tau$ contribution to correct for the observed mismodelling in m_{jj}.

Table 7.3: Event selection for the $Z \to \ell\ell$ validation region.

Leptons	Jets
== 2 leptons, OS and SF	>= 2 jets
$p_{\mathrm{T}}(\ell_1) > 40$ GeV, $p_{\mathrm{T}}(\ell_2) > 30$ GeV	$p_{\mathrm{T}}(j_1) > 70$ GeV, $p_{\mathrm{T}}(j_2) > 30$ GeV
$0.8 < \Delta R_{\ell\ell} < 2.5$, $\lvert\Delta\eta_{\ell\ell}\rvert < 1.5$	$\lvert\Delta\eta(j,j)\rvert > 3$, $m_{jj} > 300$ GeV
$m_{\ell\ell} > 80$ GeV, $E_{\mathrm{T}}^{\mathrm{miss}} < 55$ GeV	no b-tagged jet with $p_{\mathrm{T}} > 25$ GeV

While the nOS procedure gives an estimate of the shape of the distribution of the Fake contribution, it is not expected that the overall number of Fake events is the same in nOS and OS events. A scaling factor, r_{QCD}, is applied to account for this difference. This factor is derived in the QCD fit region, using the RooFit toolkit [146]. The maximum-likelihood method is applied to conduct a simultaneous fit of the normalization factors r_{QCD} and r_Z of the Fake template and the $Z \to \tau\tau$ prediction to the $\Delta\eta(\tau, \tau)$ distribution observed in data. The resulting distributions are shown in Fig. 7.4.

The resulting values, with their statistical uncertainties, are $r_{\mathrm{QCD}} = 0.75 \pm 0.02$ and $r_Z = 0.89 \pm 0.02$. The value of r_{QCD} is used as the initial normalization factor for the Fake template in the statistical analysis described in Sec. 7.6. The r_Z factor is not used, since the normalization of the $Z \to \tau\tau$ background is correlated across the four analysis channels. Instead, the starting value $r_Z = 1$ is chosen in all channels.

In the following, separately measured values $r_Z = 0.766$ and $r_{\mathrm{QCD}} = 0.757$ are applied for pre-fit yields and plots, where “pre-fit” describes all results not

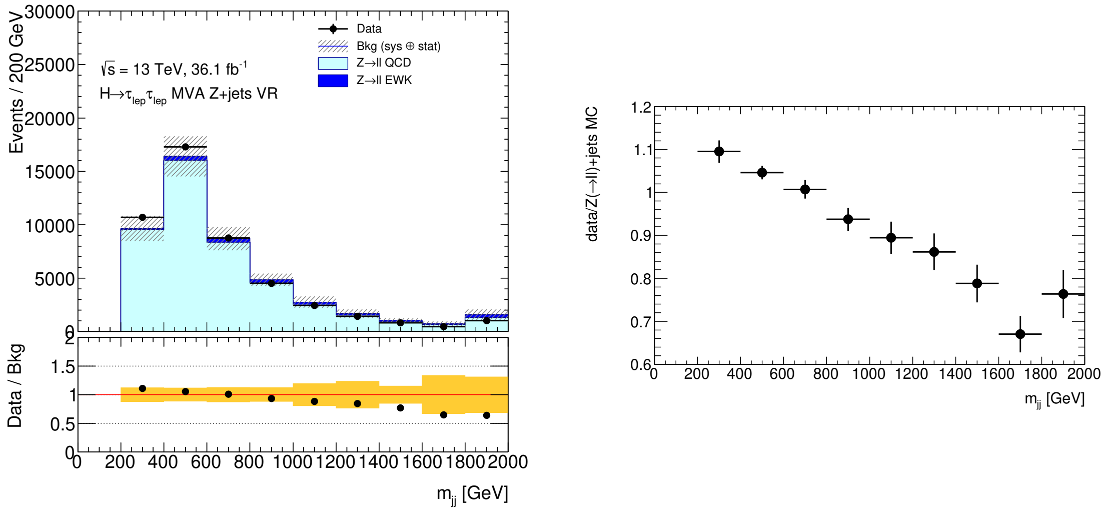

(a) (b)

Figure 7.3: (a) Distribution of m_{jj} in the $Z \rightarrow \ell\ell$ validation region mimicking the event selection of the $\tau_{\mathrm{had}}\tau_{\mathrm{had}}$ channel. (b) Weights for the $Z \rightarrow \tau\tau$ contribution to correct for the observed mismodelling in m_{jj}.

obtained from the profile likelihood fit described in Sec. 7.6. These values are chosen to reproduce the yields of $Z \rightarrow \tau\tau$ and the Fake background obtained from a fit in the low-BDT control region introduced in Sec. 7.4.

7.4 Event Categorization

A BDT for further signal separation is trained in the VBF inclusive region. Its properties as well as the results of the training are presented in this section. The training procedure is documented in Ref. [147].

7.4.1 Properties of the BDT

A BDT is trained with event samples labelled as either signal or background. In order to achieve a separation of the VBF signal, simulated VBF $H \rightarrow \tau\tau$ events were used as signal and the sum of $Z \rightarrow \tau\tau$ and Fake events were used as background. Other background contributions are much less prevalent in the VBF inclusive region and therefore ignored in the BDT training. To distinguish signal and background events, the BDT must be given distributions of variables that differ for signal and background. The distributions of the variables that were

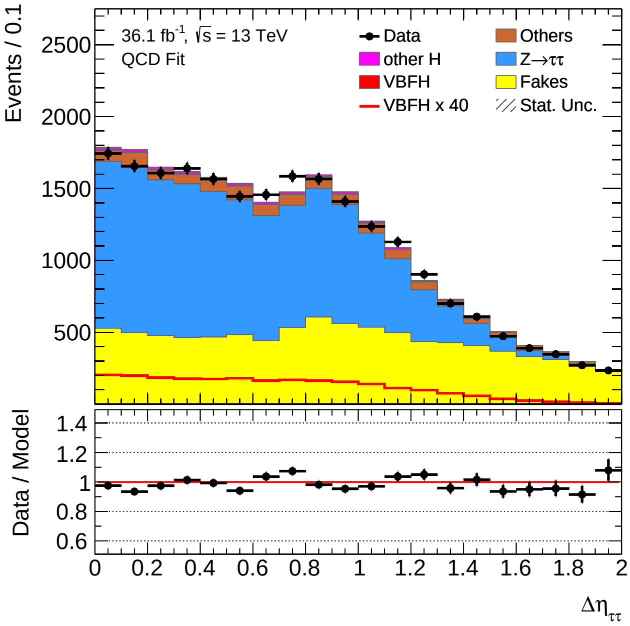

Figure 7.4: Event yields as a function of $\Delta\eta(\tau,\tau)$ in the QCD fit region. The normalization factors r_{QCD} and r_Z of the Fake and $Z \to \tau\tau$ contributions are fitted to the data simultaneously. The usage of $\Delta R(\tau,\tau)$ instead of other variables is motivated by the purity of the Fake contribution at values $\Delta R(\tau,\tau) > 1.5$.

found to achieve the greatest separation in the VBF inclusive region are shown in Fig. 7.5.

The MMC-estimated di-τ mass $m_{\tau\tau}^{\text{MMC}}$ is included to reconstruct the Higgs-boson mass. The centrality variables $C_{jj}(\tau_0)$ and $C_{jj}(\tau_1)$ describe how central the considered $\tau_{\text{had-vis}}$ candidate is with respect to the two leading jets in the event:

$$C_{jj}(\tau_{\text{had-vis}}) = \exp\left[\frac{-4}{(\eta(j_1)-\eta(j_2))^2}\left(\eta(\tau_{\text{had-vis}}) - \frac{\eta(j_1)+\eta(j_2)}{2}\right)^2\right].$$

In order to identify VBF events based on the jet activity in the event, the di-jet invariant mass m_{jj} is included, which typically reaches high values in signal events. For similar reasons, the p_{T} of the combined state of the $\tau_{\text{had-vis}}$ candidates, the jets and the $E_{\text{T}}^{\text{miss}}$ estimation named $p_{\text{T}}^{\text{tot}}$ is included in the BDT. Since additional resolvable jets apart from the two tagging jets are rare in VBF events, C_{jj} is expected to have values close to 0 in signal events. To construct the $E_{\text{T}}^{\text{miss}}$ centrality $C(E_{\text{T}}^{\text{miss}})$, the transverse plane is transformed such that the direction of the

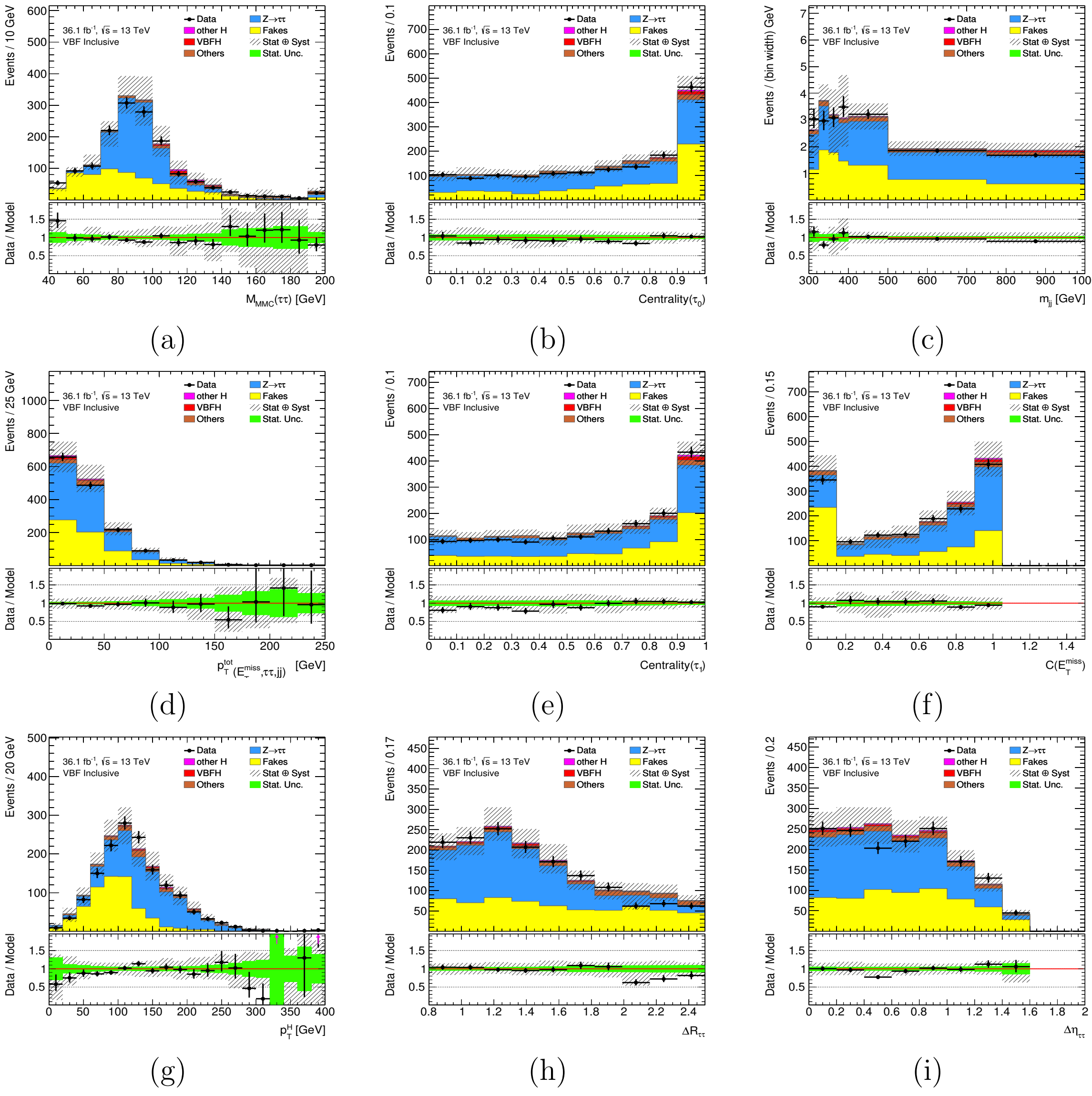

Figure 7.5: Distributions of the BDT input variables in the VBF inclusive region. The hatched band indicates statistical uncertainties and all systematic uncertainties apart from the $Z \to \tau\tau$ scale variations.

$\tau_{\text{had-vis}}$ candidates are orthogonal, and that the smaller ϕ angle between the $\tau_{\text{had-vis}}$ candidates defines the positive quadrant of the transformed plane. Then $C(E_T^{\text{miss}})$ is defined as the sum of the x and y components of the E_T^{miss} unit vector in this transformed plane. If the τ-lepton decays are the only source of E_T^{miss} through the production of neutrinos, ϕ^{miss} should in many cases be in between $\phi(\tau_0)$ and $\phi(\tau_1)$, leading to values of $C(E_{\mathrm{T}}^{\mathrm{miss}})/\sqrt{2}$ close to 1. The $p_{\mathrm{T}}(\tau, \tau, E_{\mathrm{T}}^{\mathrm{miss}})$, also referred to as p_{T}^{H}, is included to further discriminate against the Fake background. While in processes with true $\tau_{\text{had-vis}}$ objects, adding the four-vectors often increases the p_{T} value due to the collimation of the objects, stronger cancellations are expected in Fake events, where the correlation between the $\tau_{\text{had-vis}}$ candidates and the $E_{\mathrm{T}}^{\mathrm{miss}}$ is smaller. For similar reasons, the variables $\Delta\eta(\tau, \tau)$ and $\Delta R(\tau, \tau)$ are included. In processes with true hadronic τ-lepton decays, large values are unlikely, while the expected spectrum is more flat for the Fake background.

In the training algorithm, cuts are applied on the variables that achieve the largest separating power between signal and background. The separating power is quantified using the “Gini impurity”

$$g = \frac{2sb}{(s+b)^2} \, ,$$

which a cut needs to minimize for a maximal separation of signal contribution s and background contribution b. By applying consecutive cuts on individual variables, the given dataset is split into different subsets named “leaves.” If the signal contribution is below 50%, the leaf is labelled background-like, else signal-like. An event from a signal-like leaf receives the tree score +1, background-like events receive the score −1.

This describes the structure of a single decision tree. A BDT is an ensemble of trees that are constructed consecutively through a procedure named “boosting.” The “GradientBoost” algorithm assigns a weight greater than 1 to all misclassified events of a tree, in order to increase their importance in the construction of the next tree [148]. When a pre-set number of trees is reached, the BDT training is concluded. The “BDT score” of an event is the average score of +1 or −1 from the individual trees. In this analysis, a cut is applied to the BDT score in order to define the final signal and control region selection.

A two-fold cross-evaluation scheme is employed for training and evaluation of the BDT performance. All datasets involved in the training are split into two subsets of equal size. By performing two separate trainings on these subsets, two BDTs are constructed. To evaluate the performance of these without being biased by using the same events as in the training, each BDT is tested on the training set of the other one. This procedure is illustrated in Fig. 7.6. The distribution of the BDT score in the VBF inclusive region is shown in Fig. 7.7.

7.4.2 Signal Region Construction

The BDT is used to construct a signal-enriched subregion of the VBF inclusive region, in order to maximize the sensitivity to the CP properties of the signal

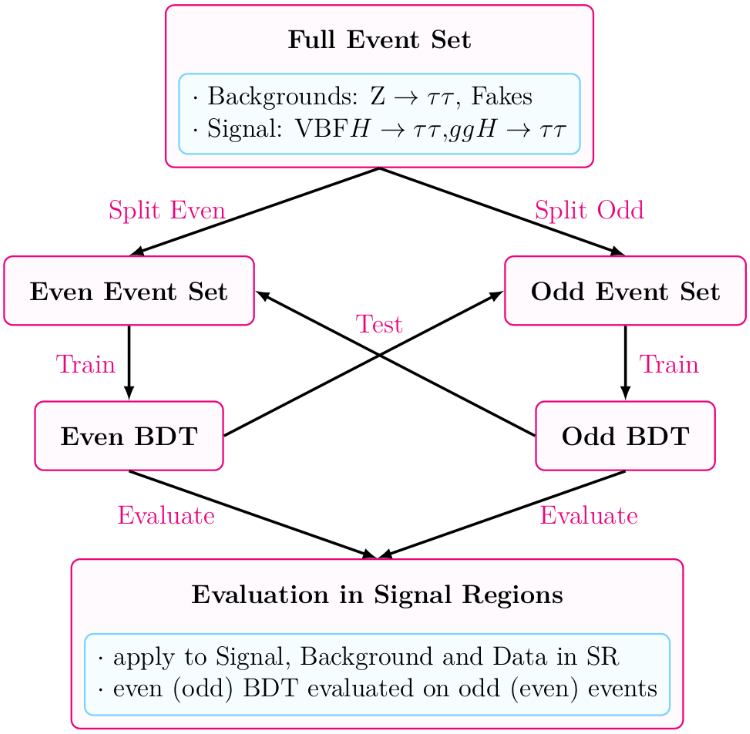

Figure 7.6: Illustration of the cross-evaluation scheme applied for the BDT-based event categorization in the VBF inclusive region. The signal included in the training of the BDT used in this analysis was only VBF $H \to \tau\tau$ [147].

process. In order to find the cut value on the BDT score that maximizes the signal sensitivity, a scan of the Asimov significance

$$Z_0 = \sqrt{2\left((s+b)\ln\left(1+\frac{s}{b}\right) - s\right)}\,,$$

with s and b being the estimated signal and background yields, for all BDT score values in steps of 0.01 is performed. The maximal Z_0 was found when cutting at BDT score > 0.89, but in order to avoid statistical fluctuations in the Fake background estimation, the cut was loosened to 0.87 instead. This is the highest cut value for which all considered systematic variations of the Fake background gave a positive total yield, increasing the stability of the likelihood fit described in Sec. 7.6. The yields in the VBF inclusive region as well as the low-BDT control region (BDT score < 0.87) and the high-BDT signal region (BDT score ≥ 0.87) are summarized in Tab. 7.4.

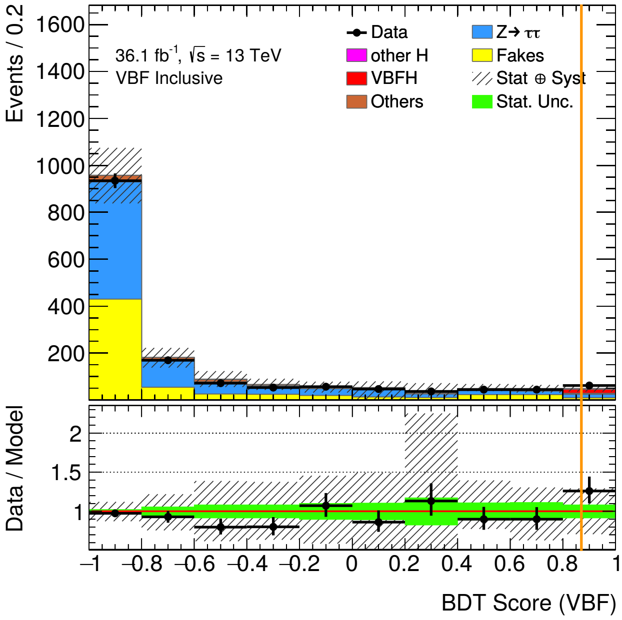

Figure 7.7: BDT score distribution in the VBF inclusive region. The vertical orange line indicates the separation between low-BDT CR and high-BDT SR. The hatched band indicates statistical uncertainties and all systematic uncertainties apart from the $Z \to \tau\tau$ scale variations.

The low-BDT CR is included in the likelihood fit to improve the estimation of the Fake and $Z \to \tau\tau$ backgrounds. The variable that was found to be most suitable for this purpose is the mass $m_{\tau\tau}^{\text{MMC}}$ of the di-τ system. As shown in Fig. 7.8a, it exhibits a peak at around 90 GeV which helps to constrain the normalization of the $Z \to \tau\tau$ background contribution. Moreover, the events with $m_{\tau\tau}^{\text{MMC}} < 60$ GeV are found to be mostly Fake events.

For the test of CP conservation, the Optimal Observable is used in the SR. Fig. 7.8b shows that its distribution is well-modelled in the CR, giving confidence in the simulation.

The Fake background estimation in the SR is statistically very limited, due to only few events in the nOS region passing the BDT score requirement. In order to make the estimate of the Fake contribution more robust, the ID requirement on the Fake template is loosened to the medium BDT-based ID instead of using the default tight ID. Since the yield of the Fake background depends on the ID, this procedure involves scaling the medium ID Fake template to reproduce the overall normalization of the default prediction. This is only done in the high-BDT SR, and only for the Fake template. A comparison of the predicted shapes of the

Table 7.4: Event yields in the $\tau_{\text{had}}\tau_{\text{had}}$ channel for the VBF inclusive region, the low-BDT region and the high-BDT signal region. Normalization factors are applied to the $Z \to \tau\tau$ and Fake backgrounds. Uncertainties are statistical only.

Process	VBF inclusive	Low-BDT CR	High-BDT SR
VBF	28.0 ± 0.3	14.3 ± 0.3	13.74 ± 0.21
Top	43.3 ± 4.3	43.0 ± 4.4	0.36 ± 0.36
W	19.0 ± 4.0	17.7 ± 3.9	1.4 ± 1.0
$Z \to \ell\ell$	1.0 ± 0.7	1.0 ± 0.7	0.0 ± 0.0
$Z \to \tau\tau$	826 ± 19	817 ± 19	9.4 ± 2.3
Fake	630 ± 24	627 ± 24	3.2 ± 1.8
Diboson	13.7 ± 1.3	13.4 ± 1.3	0.27 ± 0.07
(ggF/VH/ttH)	17.0 ± 0.6	14.4 ± 0.5	2.7 ± 0.2
Sum of backgrounds	1550 ± 31	1533 ± 31	17.2 ± 3.1
Data	1516	1479	37
S/B	0.02	0.009	0.75

Optimal Observable distribution for the Fake background depending on the ID working point is shown in Fig. 7.9a. The O_{opt} distribution in the SR, including the shape prediction of the Fake background with the medium ID working point, is shown in Fig. 7.9b.

Before using the high-BDT SR for a test of CP conservation, it must be verified that the BDT score is not correlated with the Optimal Observable, since this would cause a biased measurement in the SR. A possible correlation is tested by comparing the mean values of the O_{opt} distribution in different bins of the BDT score. The result is shown in Fig. 7.10. No significant trend of the mean value with the BDT score is observed. Other effects, such as the shapes of the input variables depending on the CP scenario, can impact the sensitivity of the measurement, but they cannot bias the CP measurement. Therefore, they have not been studied in detail.

7.5 Systematic Uncertainties

The systematic uncertainties for this analysis can be split into three types: experimental uncertainties, theoretical uncertainties and uncertainties on the background

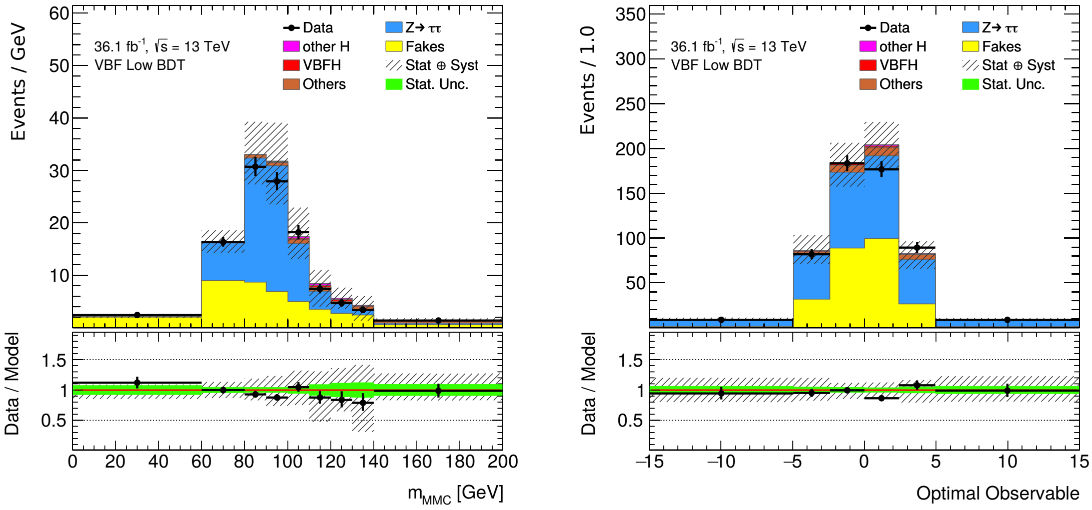

(a) (b)

Figure 7.8: Distribution of (a) $m_{\tau\tau}^{\mathrm{MMC}}$ and (b) the Optimal Observable in the low-BDT control region. The number of entries in each bin is divided by the width of the specific bin. The hatched band indicates statistical uncertainties and all systematic uncertainties apart from the $Z \to \tau\tau$ scale variations.

estimation technique. The experimental uncertainties applied are the same as described in Sec. 6.4, except that muon-related uncertainties are not considered in the $\tau_{\mathrm{had}}\tau_{\mathrm{had}}$ channel and that the uncertainty related to the jet-energy resolution is estimated using a scheme of eleven different variations instead of eight.

7.5.1 Theoretical Uncertainties

Uncertainties on the theory prediction are included for the $H \to \tau\tau$ processes and the main simulated background, $Z \to \tau\tau$. No theoretical uncertainties have been evaluated for the other simulated backgrounds, since their contributions are much smaller than that of $Z \to \tau\tau$.

Theoretical Uncertainties on the Simulation of $H \to \tau\tau$

The theoretical uncertainties on $H \to \tau\tau$ processes can be attributed to three sources. First are the QCD scales μ_R and μ_F, accounting for missing higher orders of QCD corrections. Second are non-perturbative parts of the simulation, such as the underlying event and hadronization. Third are uncertainties on experimentally

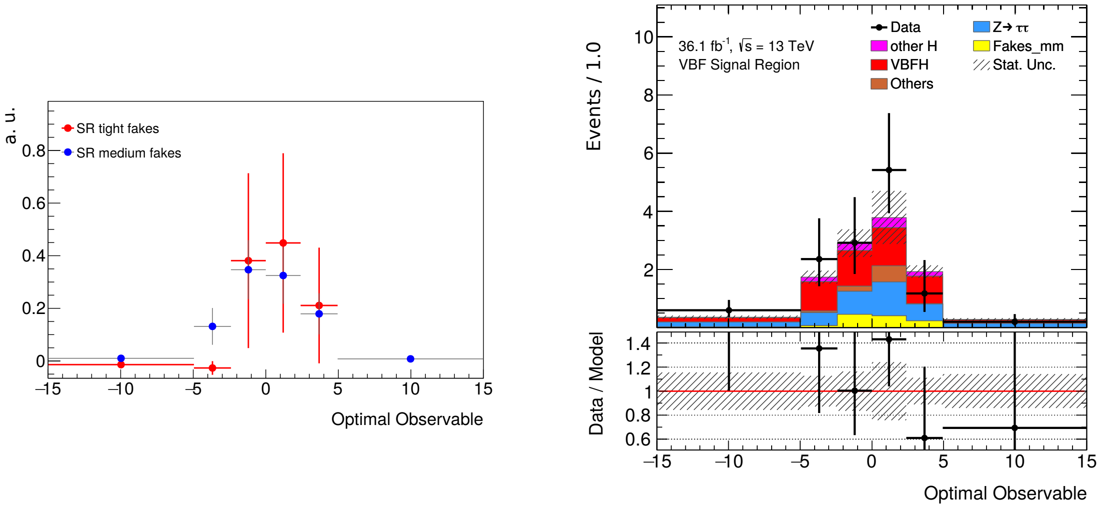

(a)

(b)

Figure 7.9: (a) Comparison of the Fake background prediction using the default tight ID criterion (red) and loosening it to the medium working point (blue). The distributions are both normalized to a total integral of one. The prediction for the rightmost bin is not visible for the tight ID since no event from the nOS region with $O_{\text{opt}} \in [5, 15]$ passes the BDT cut. (b) Distribution of the Optimal Observable in the high-BDT SR. The number of entries in each bin is divided by the width of the respective bin. Only statistical uncertainties are shown in both plots.

measured parameters that are included in the event generation, such as PDFs and α_S.

These impact the total production cross-section of a process, the detector acceptance as well as the shape of the simulated distributions of different variables. The impact on the total cross-section is treated separately, while the acceptance and shape uncertainties on the $m_{\tau\tau}^{\text{MMC}}$ and O_{opt} distributions are correlated for the same source of uncertainty. The cross-section uncertainties, which arise from $H \to \tau\tau$ branching ratio, QCD scale, PDF and α_S uncertainties, are documented in Ref. [23]. These are not taken into account for the VBF signal, since the focus of the analysis is the measurement of $\tilde{d}$. For the reasons described in Sec. 3.5, this measurement is independent of the cross-section and no assumptions on it are taken into account.

The QCD scale uncertainties are estimated by varying the nominal values of μ_R and μ_F by multiplying different combinations of the factors 2 and 0.5 to them, with the restriction $1/2 \leq \mu_R/\mu_F \leq 2$. These variations are compared and in each

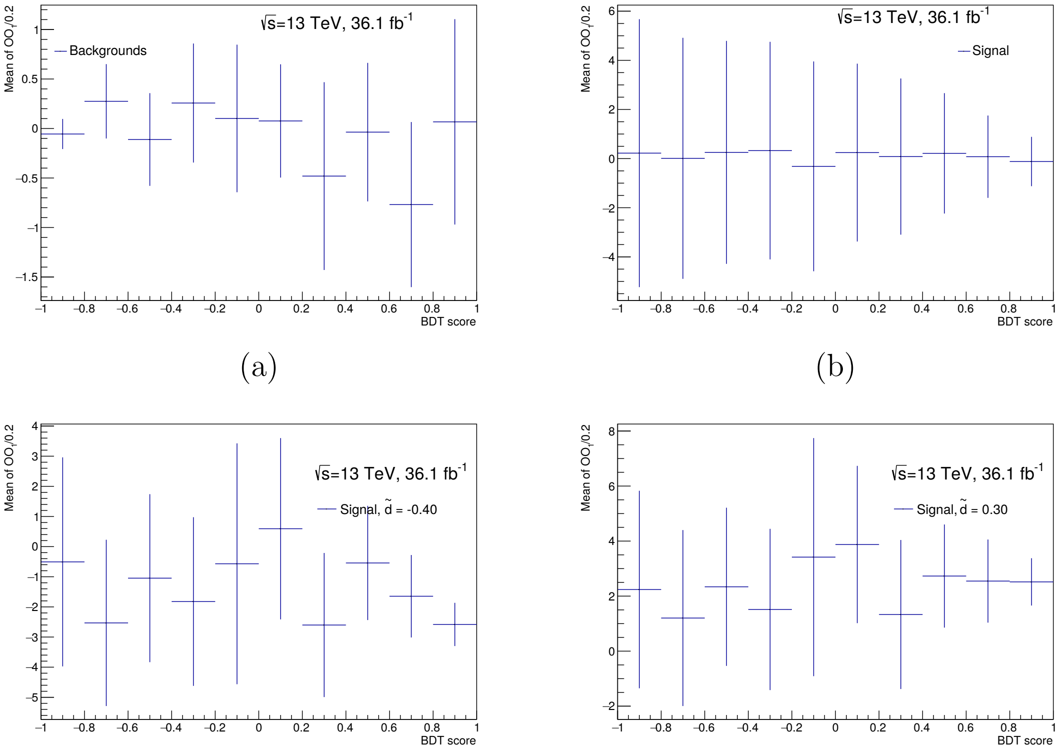

(a) (b)

(c) (d)

Figure 7.10: Mean value of O_{opt} in different bins of the BDT score for (a) the sum of all backgrounds, (b) the SM VBF signal, (c) the VBF signal assuming $\tilde{d} = -0.4$, (d) the VBF signal assuming $\tilde{d} = 0.3$. Only statistical uncertainties are shown.

bin of the final discriminant, the largest discrepancy between the nominal and the varied distribution is kept as the final estimate of the QCD scale uncertainty.

This procedure is applied for all $H \to \tau\tau$ processes except for ggF, since it can lead to an underestimation of uncertainties for this process. Instead, the LHC Higgs Cross-Section Working Group recommends using a set of nine variations that cover the effect of uncertainties on the QCD scales, the population of the VBF phase space, the Higgs-boson p_{T} distribution and the cross-section dependence on the mass of the top quark [149].

The uncertainties related to parton showering and the underlying event simulation are evaluated by comparing the predictions of samples generated with Pythia 8 and Herwig 7. In accordance with Ref. [127], the total PDF uncertainty is estimated from 30 independent variations. Additionally, two α_S variations are included.

Theoretical Uncertainties on the Simulation of $Z \to \tau\tau$

For the $Z \to \tau\tau$ contribution, the QCD scale and PDF uncertainties are evaluated in the same way as for $H \to \tau\tau$. Since the $Z \to \tau\tau$ sample is composed of multiple exclusive jet multiplicity categories, a jet-to-parton matching following the CKKW procedure is conducted [138]. A variation of the introduced scale is applied through a truth-level parametrization in $p_{\text{T}}(Z)$ and the number of jets. The QSF scale for resummation of soft collinear radiation in the parton shower is varied using the same parametrization.

The cross-section of vector-boson fusion or electroweak production of Z bosons is not measured very accurately, and therefore an additional uncertainty is applied on the fraction of Z+jets events produced via this mechanism. To reflect the uncertainty on the m_{jj} reweighting, the full difference between the integral of $Z \to \tau\tau$ with and without weights is applied as an uncertainty. The impact on the shape of the $m_{\tau\tau}^{\text{MMC}}$ and O_{opt} distributions was found to be negligible. The uncertainty on the m_{jj} reweighting is correlated in the low- and high-BDT regions.

To evaluate the uncertainty introduced by the parton shower, an alternative $Z \to \tau\tau$ sample generated with MadGraph5_aMC@NLO and Pythia 8 was used. To reduce the impact of statistical fluctuations, the relative difference between the MadGraph and Sherpa prediction in each bin of the SR O_{opt} distribution is derived in the VBF inclusive selection. The same is done for the uncertainties on the QCD and CKKW scales.

Another set of variations is introduced to cover the possibility that the theoretical uncertainties cause a migration of $Z \to \tau\tau$ between the low-BDT CR and high-BDT SR. This is done in multiple steps. In the first step, the yields after varying any of the theory predictions in both fit regions are calculated. These are then simultaneously scaled such that the sum of yields equals the nominal yield prediction. By correlating the resulting relative yield changes from the last step between the low-BDT CR and the high-BDT SR, the final migration uncertainty is constructed. This procedure is applied independently for each of the introduced theoretical uncertainties. In combined fits of all decay channels, analogously defined migration uncertainties between the decay channels are also included.

7.5.2 Uncertainties on the Background Estimation Method

Two sources of uncertainties are considered for the construction of the nOS Fake template. The first one covers the MC contamination in the nOS control region and the fact that it contains 2-prong $\tau_{\text{had-vis}}$ candidates, for which no central performance measurements are performed in ATLAS. To account for missing efficiency scale factors on the MC subtraction term, the MC contribution is varied within its total statistical uncertainty in the QCD fit region and the relative difference, in bins of $m_{\tau\tau}^{\mathrm{MMC}}$, is applied as an uncertainty on the Fake template in the low- and high-BDT regions.

In addition, an uncertainty to account for the loosened ID criterion applied to the Fake template in the high-BDT SR is constructed by comparing the O_{opt} shape in the VBF inclusive region for the medium and tight BDT ID working points. The comparison is shown in Fig. 7.11, and the resulting ratio between tight and medium O_{opt} distributions is applied as an uncertainty on the SR Fake template.

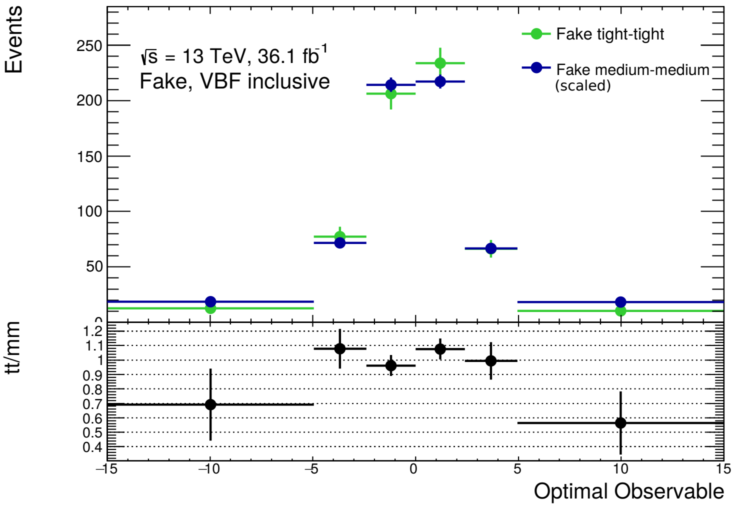

Figure 7.11: Comparison of the shape of the O_{opt} distributions in the VBF inclusive selection, using either the tight (green) or the medium (blue) ID working point. In order to only assess shape differences, the medium-ID distribution is scaled to match the total yield of the tight-ID distribution. The ratio shown in the lower panel is applied as an uncertainty on the shape of the Fake template in the high-BDT SR.

A summary of all included systematic uncertainties is given in Tab. 7.5.

7.6 Template Likelihood Fit

The comparison of the estimated signal and background contributions to the observed data, including the measurement of $\tilde{d}$, is performed via a template likelihood fit. This fit includes not only the $\tau_{\mathrm{had}}\tau_{\mathrm{had}}$ channel, but also three more channels

Table 7.5: Summary of considered systematic sources of uncertainty with the number of variations per source. The column "Type" specifies the number of components that impact the shape (S) or normalization (N) of the input distributions in the $\tau_{\text{had}}\tau_{\text{had}}$ low-BDT CR and high-BDT SR after applying the simplification procedure described in Sec. 7.6.2.

Source	Components	Type
Jets	36	N(28) S(17)
$\tau_{\text{had-vis}}$ candidates	8	N(8) S(3)
$E_{\text{T}}^{\text{miss}}$	3	N(3) S(2)
Theory $H \to \tau\tau$	47	N(18) S(2)
Theory $Z \to \tau\tau$	11	N(10) S(4)
Fake estimate	2	N(1)
Luminosity	1	N(1)
Pile-up reweighting	1	N(1) S(1)

covering leptonic decays of τ leptons, which are described more closely in Ref. [11]. An overview of the maximum-likelihood method as well as its application to the analysis at hand is given in this section.

7.6.1 Likelihood Construction

From the $\tau_{\text{had}}\tau_{\text{had}}$ channel, the distribution of $m_{\tau\tau}^{\text{MMC}}$ in the low-BDT control region and O_{opt} in the high-BDT signal region are used to measure the value of $\tilde{d}$. Using the distributions of the same variables, similarly defined regions are also used from the $\tau_{\text{lep}}\tau_{\text{lep}}$ SF, $\tau_{\text{lep}}\tau_{\text{lep}}$ DF and $\tau_{\text{lep}}\tau_{\text{had}}$ channels. Since top-quark backgrounds are an important background in the $\tau_{\text{lep}}\tau_{\text{lep}}$ channels, top-quark control regions defined by requiring the presence of b-tagged jets are included in these channels. In the $\tau_{\text{lep}}\tau_{\text{lep}}$ SF channel, the $Z \to \ell\ell$ process also contributes significantly. Therefore, a dedicated control region is defined by requiring $80\ \text{GeV} < m_{\ell\ell} < 100\ \text{GeV}$ for the invariant mass $m_{\ell\ell}$ of the two leptons. Only the total event yield is considered in the top-quark and $Z \to \ell\ell$ CRs. The regions included in the fit are summarized in Fig. 7.12.

A statistical model is introduced to fit the estimated signal contribution s and background contribution b to the observed data distributions. These contributions make up the total expected contribution n^{exp}, which, in each bin i of the

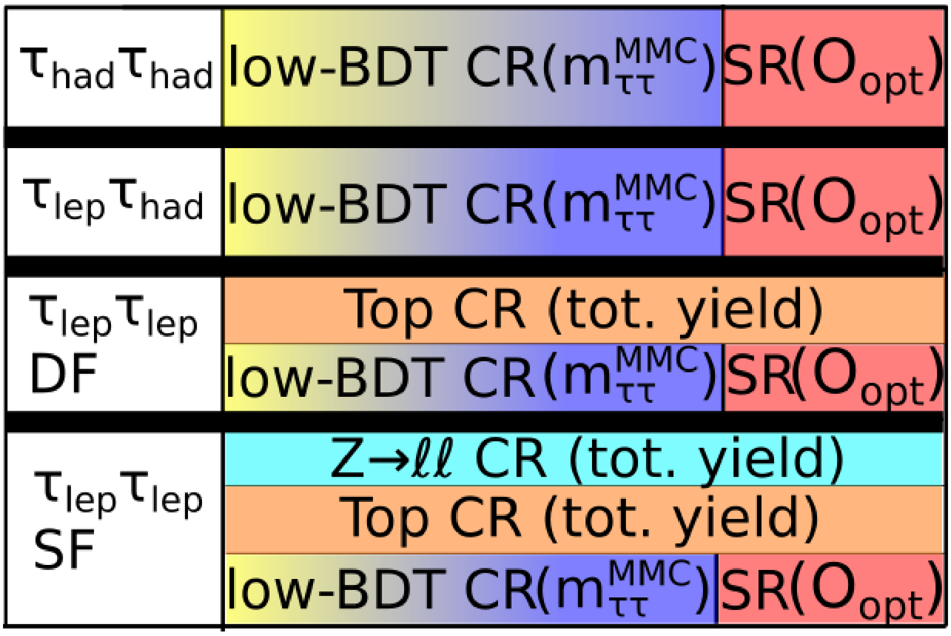

Figure 7.12: Sketch of all analysis regions included in the likelihood fit. Apart from a low-BDT CR and a high-BDT SR, the $\tau_{\text{lep}}\tau_{\text{lep}}$ channels also include CRs to better constrain the normalization of the Top and $Z \to \ell\ell$ backgrounds. The variable included in the fit in each region is given in parantheses.

distributions entering the fit, can be expressed as

$$n_i^{\text{exp}} = \mu s_i(\boldsymbol{\theta}) + b_i(\boldsymbol{\theta}) \; .$$

The symbol $\boldsymbol{\theta}$ describes a set of parameters θ_k describing the considered sources of uncertainty on the measurement. These θ_k are called “nuisance parameters” (NPs). The factor μ scaling the signal contribution is called signal strength, and it is introduced in order not to be biased by the SM expectation on the total production cross-section of the signal process $\sigma_{\text{SM}}^{\text{VBF}}$. The signal strength can be expressed as

$$\mu = \frac{\sigma_{\text{obs}}^{\text{VBF}}}{\sigma_{\text{SM}}^{\text{VBF}}}$$

with the observed production cross-section $\sigma_{\text{obs}}^{\text{VBF}}$, and it is a free parameter to be determined by the fit.

Using these quantities, a simple likelihood function L for a comparison of a predicted binned distribution to the data distribution $(n_1, n_2, ..., n_N)$ can be written as [150]:

$$L(\mu, \boldsymbol{\theta}) = \prod_{j=1}^{N} \frac{(\mu s_j(\boldsymbol{\theta}) + b_j(\boldsymbol{\theta}))^{n_j}}{n_j} e^{-(\mu s_j(\boldsymbol{\theta}) + b_j(\boldsymbol{\theta}))} \, .$$

The likelihood is constructed by multiplying the probabilities to observe n_j events in bin j for all N bins included in the measurement, given a specific value of μ and the NPs $\boldsymbol{\theta}$. The probability in each bin is described by a Poisson distribution, which leads to the given functional form of L. The best-fit result is defined when L is maximal, or equivalently, when n_i^{exp} is as close as possible to n_i in all bins. The likelihood function is constructed using “HistFactory” [151] and “RooStats” [152], while the maximization and uncertainty estimation are conducted using “RooFit” [146] and “Minuit” [153].

The uncertainty on the best-fit value $\hat{\theta}_k$ of a specific parameter θ_k obtained from likelihood maximization can be estimated using a Taylor expansion. For convenience, the expansion is conducted on the logarithm of the likelihood, which, due to being monotonic, is maximal for the same set of fit parameter values as the likelihood itself:

$$\begin{aligned} \ln(L(\theta_k)) = \ln(L(\hat{\theta}_k)) &+ \left(\frac{\partial \ln(L(\theta_k))}{\partial \theta_k} \right)_{\theta_k = \hat{\theta}_k} (\theta_k - \hat{\theta}_k) \\ &+ \left(\frac{\partial^2 \ln(L(\theta_k))}{\partial^2 \theta_k} \right)_{\theta_k = \hat{\theta}_k} (\theta_k - \hat{\theta}_k)^2 + \mathcal{O}((\theta_k - \hat{\theta}_k)^3) \, . \end{aligned} \tag{7.1}$$

The derivative in the second term vanishes, since it is evaluated at the maximum of L. For evaluating the last term, it is assumed that $\ln(L(\theta_k))$ has a parabolic dependence on θ_k around its maximum, as in the limit of large sample sizes, the likelihood has a Gaussian dependence on θ_k. This leads to:

$$\sigma_{\theta_k}^2 = - \left(\frac{\partial^2 \ln(L(\theta_k))}{\partial^2 \theta_k} \right)^{-1} \, .$$

With this, Eq. (7.1) reduces to:

$$\ln(L(\theta_k)) = \ln(L(\hat{\theta}_k)) - \frac{(\theta_k - \hat{\theta}_k)^2}{2\sigma_{\theta_k}^2} \, ,$$

and thus:

$$\ln(L(\theta_k \pm N\sigma_{\theta_k})) = \ln(L(\hat{\theta}_k)) - \frac{N^2}{2} \, . \tag{7.2}$$

Therefore, the 1σ confidence level (CL) interval on $\hat{\theta}_k$ can be constructed by identifying the value of θ_k where the logarithm of the likelihood is reduced by $1/2$. The CLs used throughout this chapter are 68% ($N = 0.99$) and 95% ($N = 1.96$), constructed by determining a difference to the maximum of $\ln(L)$ of 0.49 and 1.92, respectively. The assumption of a parabolic dependence is fulfilled in the limit of very large sample sizes. In the VBF $H \to \tau\tau$ CP analysis, however, the sample sizes are not large. A study to estimate the error introduced by this assumption is presented in Sec. 7.8.

It is possible to improve the accuracy of the fit by incorporating external knowledge on the sources of systematic uncertainty. An example for this is the measurement of the τ-trigger SF measured in Chap. 6. The SF, measured along with its uncertainty, is included in the likelihood function by extending it with a Gaussian constraint term for the NP θ_t related to the trigger SF:

$$G(\theta_t) = \frac{1}{\sqrt{2\pi}} \exp\left(\theta_t^2/2\right) \ .$$

The nominal SF is represented by θ_t being equal to zero. The upward and downward variations of the SF are set to $\theta_t = +1$ and $\theta_t = -1$, respectively. A combination of linear and exponential interpolations is used to estimate which $m_{\tau\tau}^{\mathrm{MMC}}$ and O_{opt} distributions are expected for other SF values, i.e. when θ_t is neither -1, 0 nor $+1$. Including $G(\theta_t)$ in the likelihood function correlates the per-bin agreement between data and prediction, described by L, with the result of the SF measurement in Chap. 6.

Following this procedure, NPs are introduced for all considered sources of uncertainty. To include statistical uncertainties on the predicted number of entries in a specific bin, the constraint term of the associated NP is not Gaussian distributed. Instead, a Poissonian distribution of the effective number $m_i = (b_i/\delta_i)^2$ of simulated events is included using the total statistical uncertainty δ_i on the background contribution [151]:

$$P(m_i|\gamma_i m_i) = \frac{(\gamma_i m_i)^{m_i}}{m_i!} e^{-\gamma_i m_i} \ .$$

The nominal value of the associated NP γ_i of bin i is 1. Since statistical fluctuations are independent from bin to bin, an NP γ_i is introduced for each bin i of the distributions included in the fit.

In addition to the nuisance parameters associated to specific sources of uncertainty, normalization factors (NFs) are included in the fit. Apart from the NF μ that scales the signal contribution, NFs for the $Z \to \tau\tau$ background and the Fake background are introduced. These have no dedicated constraint terms, and in combined fits including all decay channels, the $Z \to \tau\tau$ NF is correlated across all channels, while the Fake NF is only applied in the $\tau_{\text{had}}\tau_{\text{had}}$ channel. This setup reflects the property that the $Z \rightarrow \tau\tau$ production cross-section does not depend on the subsequent τ-lepton decay mode and that the probed phase-space is very similar in all decay channels. Moreover, a top-quark background NF is applied in the two $\tau_{\text{lep}}\tau_{\text{lep}}$ channels. The $\tau_{\text{lep}}\tau_{\text{lep}}$ SF channel also applies an NF to the $Z \rightarrow \ell\ell$ background.

In order to measure the best-fit value of $\tilde{d}$, the described fit is performed multiple times. The only parameter varied in the input distributions of the fits is the assumed value of $\tilde{d}$, which changes the shape of the signal distribution. For each assumed $\tilde{d}$ value, the initial yield of VBF $H \rightarrow \tau\tau$ events is set to the SM prediction.

By comparing the minimized values of the negative logarithmic likelihood NLL $= -\ln(L)$ between these fits, a dependence of NLL on $\tilde{d}$ can be measured. The best estimate of $\tilde{d}$ is the one with the lowest associated NLL value. For convenience, the value of $\Delta\text{NLL} = \text{NLL} - \text{NLL}_{\text{min}}$, where NLL_{min} is the minimal NLL value obtained from all fits, are shown instead of the NLL values themselves. The advantage is that the difference from the minimum of the function $\text{NLL}(\tilde{d})$ can be read off directly, which simplifies the construction of CL intervals according to Eq. (7.2).

7.6.2 Statistical Model Implementation

An iterative algorithm was developed to construct a binning of these distributions that maximizes the amount of bins while keeping the background and signal prediction stable from statistical fluctuations. The algorithm was applied to the SR O_{opt} distribution shown in Fig. 7.9b based on a pre-binning of width 0.05 from -15 to 15, with a pre-set final bin border at $O_{\text{opt}} = 0$. Pre-bins are added up in positive and negative O_{opt} directions until the expected yields of all considered groups of processes are positive for all considered variations. The groups of processes are VBF $H \rightarrow \tau\tau$, non-VBF $H \rightarrow \tau\tau$, $Z \rightarrow \tau\tau$, Fake background and “Others”, combining di-boson, W+jets, $Z \rightarrow \ell\ell$ and top-quark production events. After two symmetric bins are constructed, the procedure is repeated starting where the last bins ended, until the full range of the O_{opt} distribution is covered. The resulting binning for the O_{opt} distribution in the $\tau_{\text{had}}\tau_{\text{had}}$ channel is: $[15, 4.95, 2.4, 0, 2.4, 4.95, 15]$, giving six bins in the SR.

For the $m_{\tau\tau}^{\text{MMC}}$ binning in the $\tau_{\text{had}}\tau_{\text{had}}$ CR, shown in Fig. 7.8a, the algorithm was adjusted to start from $m_{\tau\tau}^{\text{MMC}} = 0$ and only construct bins in positive direction, while functioning in the same way otherwise. The pre-bin width was 10 GeV, from which the algorithm constructed the binning (in GeV):
$[0, 60, 80, 90, 100, 110, 120, 130, 140, 200]$.

A number of simplifications are applied to the distributions entering the fit. This is done in order to reduce the number of degrees of freedom of the fit and thus increase its stability. For this, the variations of the input distributions with negligible impact are identified and removed before conducting the fit, which is named "pruning." Additionally, the effect of statistical fluctuations on the measurement is reduced by applying smoothing and symmetrization algorithms.

As a first step, the effect of all systematic variations is separated into two correlated effects. One affects the normalization of the considered histogram, and one affects the shape. The following steps are applied sequentially to assess the importance of the shape variations:

- A symmetrization is applied to all variations that are defined only in one direction, such as the JER variations. It is also applied in cases where the upward and downward variation both change the expected contribution in the same direction, which is known as one-sided variations. In such cases, the larger deviation from the nominal bin content is symmetrized. In case this procedure leads to negative bin contents, these are set to 10^{-6} instead. The same is done for negative bins in all input distributions.

- If the statistical uncertainty on the total yield of a histogram is greater than 10%, all shape variations are pruned. This is done since these shape variations are expected to be dominated by statistical fluctuations.

- A χ^2 test is conducted between both the upward variation and the nominal distribution and the downward variation and the nominal distribution. If the reduced χ^2 is below 0.1 in both cases, the shapes are considered compatible and the variation is pruned. This step is not applied to variations obtained from changes in event weights, such as the τ-trigger SFs.

- The "353QH twice" smoothing algorithm [154] implemented in ROOT [155] is applied to reduce statistical fluctuations in the varied distribution. This algorithm first flattens peaks and valleys, then applies a quadratic interpolation in resulting flat regions and as a last step replaces each bin content with the mean value of it and its two neighbouring bins. It is applied twice to the ratio of variation and nominal histogram, which is multiplied to the nominal histogram after the smoothing to obtain the smoothed variation.

- As a last step, the significance $S_i = |n_i^{\text{up}} - n_i^{\text{down}}|/n_i^{\text{tot}}$ of the variation of a single process group with respect to the total background prediction is computed in each bin i. If $S_i < 0.1$ for all bins i, the shape variation is pruned.

Additionally, normalization variations are only considered in the fit if either the upward or the downward fluctuation changes the total integral of a histogram by more than 0.5% and by more than the statistical uncertainty on the integral.

7.7 Fit Results

The result of the likelihood scan for $\tilde{d}$ is shown in Fig. 7.13a. Four different types of fits are conducted. In pre-fit expected fits, the dataset to approximate with the input distributions is the expected distribution for the SM expectation of $\tilde{d} = 0$ and $\mu = 1$, which is named the Asimov dataset. Therefore, the agreement is perfect in the fit using the VBF $H \to \tau\tau$ distribution with $\tilde{d} = 0$, and the minimum of the ΔNLL curve is at $\tilde{d} = 0$ by construction. Also, the best-fit μ in the $\tilde{d} = 0$ fit has to be equal to 1 by construction, which is verified in Fig. 7.13b, where the signal strength is shown in dependence of the $\tilde{d}$ value. It shows that, since the SR O_{opt} histogram that is approximated with the signal and background templates has the highest entries around zero, the best-fit μ is low when using a strongly asymmetric signal template corresponding to a large $|\tilde{d}|$.

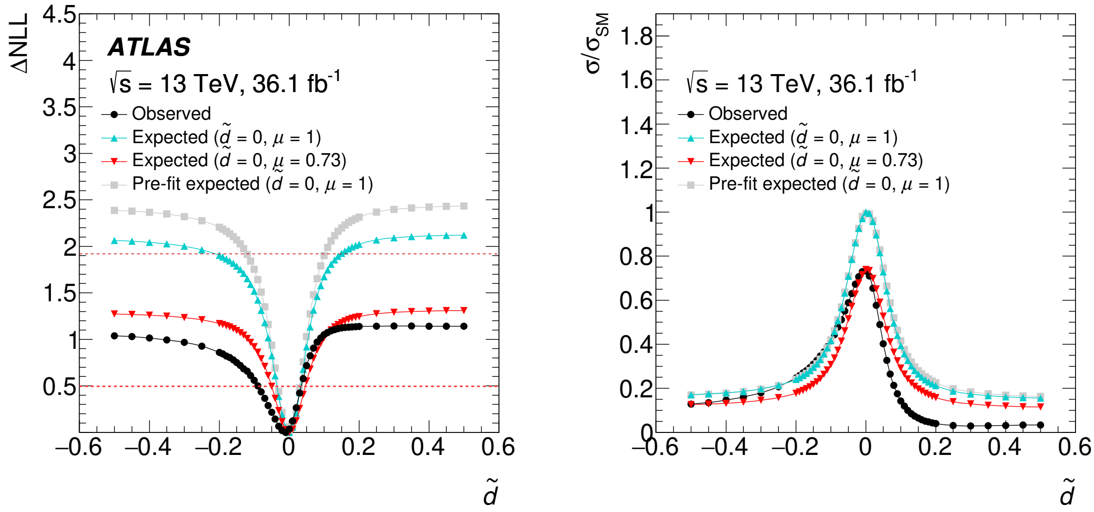

(a) (b)

Figure 7.13: Dependence of (a) the minimized NLL and (b) the VBF signal strength μ on the assumed $\tilde{d}$ value. The pre-fit expected, expected and observed results are shown. The horizontal red lines in (a) mark the 68% and 95% CL thresholds in ΔNLL according to Eq. (7.2) [11].

However, the agreement of the pre-fit expectation to the data is not very good around the peak at 90 GeV in $m_{\tau\tau}^{\text{MMC}}$ in the low-BDT CR. This has been traced back to the measurement of the scale factors related to the efficiency of the BDT-based $\tau_{\text{had-vis}}$ ID algorithm. The recommended correction factors are 1.074 ± 0.06 for 1-prong and 1.11 ± 0.07 for 3-prong $\tau_{\text{had-vis}}$ candidates. Tests conducted for the $H \to \tau\tau$ production cross-section measurement documented in Ref. [120] suggested that the 1-prong correction factor was slightly overestimated in the phase-space of the VBF $H \to \tau\tau$ CP analysis, leading to an overestimation of the contribution from the $Z \to \tau\tau$ process. For this reason, the observed NF for the $Z \to \tau\tau$ process is slightly below unity. The measured values of all NFs are listed in Tab. 7.6. Apart from the $\tau_{\text{lep}}\tau_{\text{lep}}$ NF for top-quark backgrounds, all are compatible with the SM expectation of 1 within 1σ.

Table 7.6: Measured NF values in the combined fit assuming $\tilde{d} = 0$ with total uncertainties.

Process	VBFH	$Z \to \tau\tau$	$Z \to \ell\ell$ ($\tau_{\text{lep}}\tau_{\text{lep}}$ SF)	Top ($\tau_{\text{lep}}\tau_{\text{lep}}$)	Fake ($\tau_{\text{had}}\tau_{\text{had}}$)
NF	0.73 ± 0.47	0.93 ± 0.08	1.0 ± 0.4	1.16 ± 0.06	0.99 ± 0.09

In order to incorporate corrections to the $\tau_{\text{had-vis}}$ ID SF into the estimation of the expected sensitivity, the blue curve "Expected ($\tilde{d} = 0$, $\mu = 1$)" and the red curve "Expected ($\tilde{d} = 0$, $\mu = 0.73$)" in Fig. 7.13a are constructed in two steps. At first, a fit to the observed data distribution is conducted, but only in the CRs. After this, the obtained best-fit values θ^c of all fit parameters except μ, to which the CRs do not give any sensitivity, are used in the creation of the Asimov dataset to reflect the knowledge on the data distribution in the CRs. In order to base the expected result fully on the CR fit and not be biased towards the pre-fit expectation, the likelihood function is also adjusted for obtaining the expected result. The constraint term of each NP θ_i is changed such that the central value represents the best-fit value θ_i^c from the CR fit. For NPs with a Gaussian distribution, the constraint term is changed to

$$G^c(\theta_i) = \frac{1}{\sqrt{2\pi}} \exp\left((\theta_i - \theta_i^c)^2/2\right) .$$

The Poisson distributions of an NP γ_i associated with the statistical uncertainty on the background estimate in bin i is changed to

$$P^c(m_i|\gamma_i m_i) = \frac{(\gamma_i m_i)^{m_i}}{m_i!(\gamma_i^c)^{m_i}} e^{-\frac{\gamma_i m_i}{\gamma_i^c}} ,$$

to shift the mean value of γ_i from 1 to γ_i^c. Normalization factors remain free parameters of the expected fit, and the constraint terms for NPs that are present in the complete fit but not the CR-only fit, e.g. due to pruning, are left unchanged.

As the sensitivity is clearly lower than the pre-fit expected, two different expected ΔNLL curves were constructed to identify the origin of this behaviour. In both cases, the described procedure is followed, to base the expectation on the combined CR-only fit. In the case of the cyan curve, the Asimov dataset was constructed assuming $\mu = 1$, while for the red curve $\mu = 0.73$, the best-fit value in the observed $\tilde{d} = 0$ fit, was used. Fig. 7.13b shows that the observed signal strength was lower than expected in all conducted fits, reducing the sensitivity to the signal process and thus to $\tilde{d}$. Thus, the difference between the grey curve and the cyan curve shows the impact of best-fit NP values that deviate from the pre-fit expectation. The difference between the cyan and the red curve shows the loss in sensitivity due to a smaller than expected observed signal strength. The difference between the red and black curves is due to additional shifts in best-fit NP values due to the SR data distributions as well as slightly asymmetric data O_{opt} distributions. This shows that the low observed signal strength of $\mu = 0.73 \pm 0.47$ is the main reason for the lower than expected sensitivity to $\tilde{d}$.

The observed results are obtained in the same way as the pre-fit expected ones. The only difference is that, instead of the Asimov dataset, the measured data distribution is used. The best-fit value of $\tilde{d}$ obtained is -0.01, with the 68% CL interval $\tilde{d} \in [-0.089, 0.035]$. As this covers the SM expectation of $\tilde{d} = 0$, no sign of CPV was found. The resulting observed and expected 68% and 95% CL intervals on $\tilde{d}$ are summarized in Tab. 7.7.

Table 7.7: Measured 68% and 95% CL intervals for the combined fit of all decay channels.

CL	Pre-fit expected	Expected, $\mu = 1$	Expected, $\mu = 0.73$	Observed
68%	$[-0.032, 0.031]$	$[-0.035, 0.033]$	$[-0.050, 0.046]$	$[-0.089, 0.035]$
95%	$[-0.121, 0.102]$	$[-0.212, 0.149]$	–	–

The post-fit distributions for the $\tilde{d} = -0.01$ fit in all four SRs are shown in Fig. 7.14, and the mean values of the data distributions are listed in Tab. 7.8. These mean values can be used for a simpler, less model-dependent test of CPV, since no assumption on the contribution to the data from specific processes is made. Assuming no rescattering effects, a significant deviation of the mean values from zero would mean CP violation. The conclusion for this test is the same as for the $\tilde{d}$ scan: The measured values are consistent with the SM expectation and CP conservation in HVV couplings.

To estimate how the individual channels contribute to the sensitivity of the combined fit to $\tilde{d}$, modified fits are conducted. In these fits, only yield information is used in the SR distributions of three channels, while the O_{opt} distribution is still

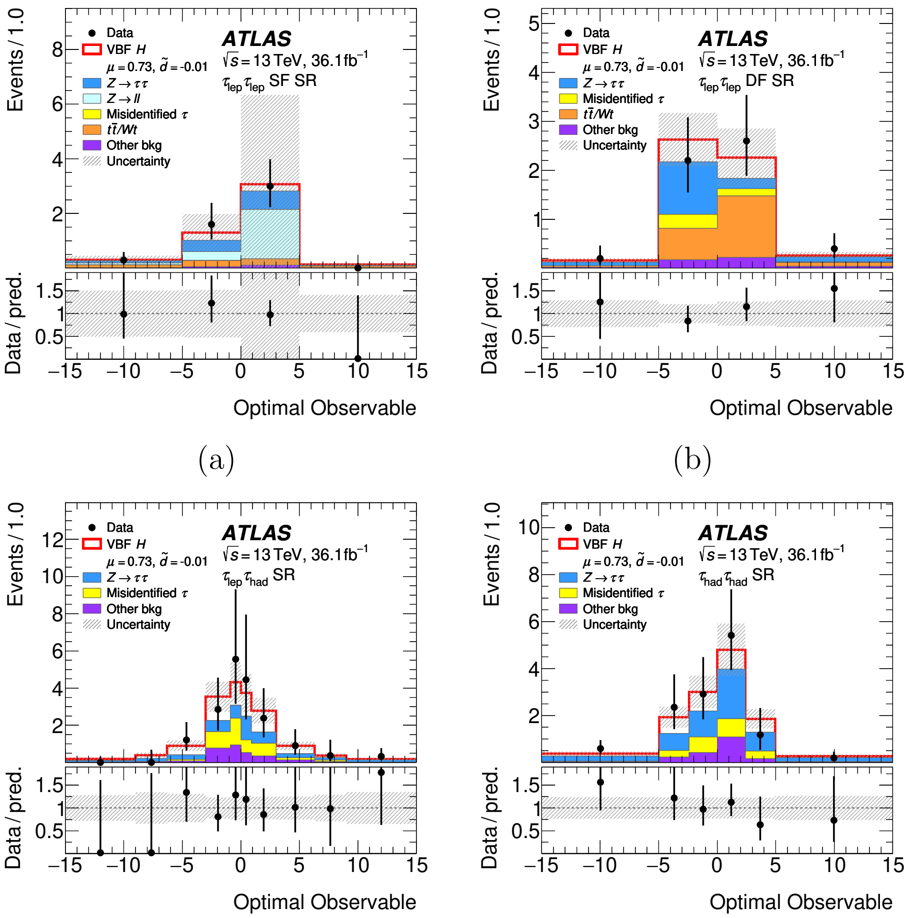

(a) (b)

(c) (d)

Figure 7.14: Post-fit O_{opt} distributions in the SR of (a) the $\tau_{\mathrm{lep}}\tau_{\mathrm{lep}}$ SF channel, (b) the $\tau_{\mathrm{lep}}\tau_{\mathrm{lep}}$ DF channel, (c) the $\tau_{\mathrm{lep}}\tau_{\mathrm{had}}$ channel, (d) the $\tau_{\mathrm{had}}\tau_{\mathrm{had}}$ channel for the combined fit with $\tilde{d} = -0.01$. The number of entries in each bin is divided by the width of the respective bin. The best-fit value $\mu = 0.73$ is used to scale the signal [11].

used in the fourth SR. This is done to keep the yield information from all channels and thus have a setup as close to the default combined fit as possible, but only exploit the sensitivity to $\tilde{d}$ through a single channel. The resulting ΔNLL curves are shown in Fig. 7.15.

The deviations of the best-fit $\tilde{d}$ values from zero in these fits are correlated with the mean values of O_{opt} observed in the SRs of the different decay channels. The negative mean O_{opt} value in the $\tau_{\mathrm{had}}\tau_{\mathrm{had}}$ leads to a best-fit $\tilde{d}$ of -0.13 and a 68%

Table 7.8: Observed mean values of the O_{opt} distributions in the SRs of the four decay channels with statistical uncertainties [11].

Channel	$\langle O_{\text{opt}} \rangle$
$\tau_{\text{lep}}\tau_{\text{lep}}$ SF	-0.54 ± 0.72
$\tau_{\text{lep}}\tau_{\text{lep}}$ DF	0.71 ± 0.81
$\tau_{\text{lep}}\tau_{\text{had}}$	0.74 ± 0.78
$\tau_{\text{had}}\tau_{\text{had}}$	-1.13 ± 0.65

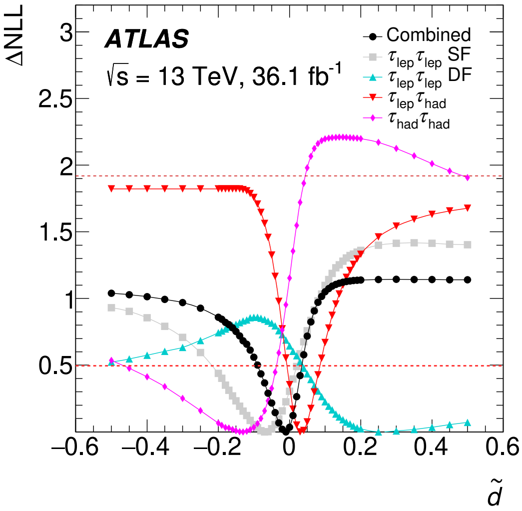

Figure 7.15: Curves of ΔNLL obtained from the fits to estimate the contribution of individual decay channels. Only information on the total yield is included in the SRs of all channels but the considered one [11].

CL interval of $\tilde{d} \in [-0.47, 0.037]$.

To study the effect of the NPs on the sensitivity to $\tilde{d}$, a number of fits to the Asimov dataset has been conducted. In these fits, the groups of NPs associated to jets, MC sample sizes, $\tau_{\text{had-vis}}$ or simply all NPs are fixed to their pre-fit value, so that they do not affect the minimization of the NLL. The results in Fig. 7.16 show that the jet-related uncertainties are the most important for this measurement. The statistical uncertainty on the background estimate and the $\tau_{\text{had-vis}}$-related uncertainties also have a visible impact on the ΔNLL curve. Other uncertainty sources, such as those related to muons or electrons or the theoretical predictions on the modelling of physics processes, have a smaller impact and are not shown.

To conclude, the obtained 68% CL interval $\tilde{d} \in [-0.089, 0.035]$ covers the SM

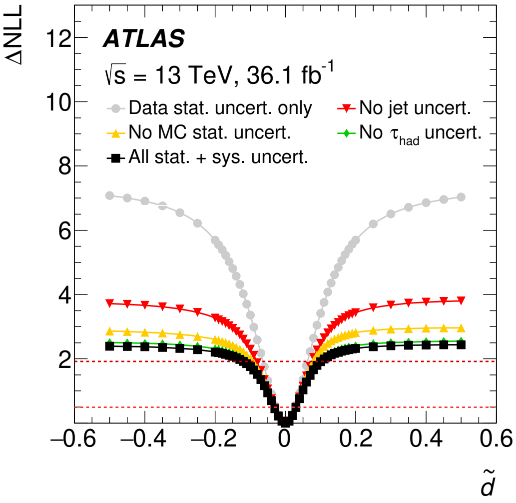

Figure 7.16: Comparison of pre-fit expected ΔNLL curves for the combination of all decay channels in the absence of different sources of uncertainty [11].

prediction of $\tilde{d} = 0$, and thus no sign of CPV (or rescattering) has been found.

7.8 Coverage Probability Study

As mentioned in Sec. 7.6, the correspondence between ΔNLL values and CL intervals described in Eq. (7.2) is only exact in regions where the NLL curve shows a parabolic dependence in the considered parameter θ_i. As evidenced by the ΔNLL curves shown in Sec. 7.7, this assumption holds around the minimum, but the curve becomes flatter at high values of $|\tilde{d}|$. This behaviour is a consequence of using the $\mathcal{O}_{\text{opt}}$ distribution in the SR. As described in Sec. 3.4, it allows for a clear distinction between the cases $\tilde{d} = 0$ and $\tilde{d} \neq 0$, but different values of high $|\tilde{d}|$ produce similar $\mathcal{O}_{\text{opt}}$ distribution, which causes the ΔNLL curve to flatten out.

As the assumption for Eq. (7.2) does not hold over the total range of $\tilde{d}$ that was investigated, a test was performed to directly study the coverage probability of the derived 68% and 95% CL intervals assuming $\tilde{d} = 0$. The test aims at the expected intervals assuming $\mu = 1$ for the combined fit, i.e. the ones obtained from the cyan curve in Fig. 7.13.

The method involves two steps. At first, pseudo-data are generated to obtain representative datasets on which to perform the study, always assuming $\tilde{d} = 0$. In the second step, fits to the datasets generated in step one are performed to find the $\tilde{d}$ value that best fits the pseudo-dataset generated with $\tilde{d} = 0$. The fits are conducted for numerous datasets and the distribution of best-fit $\tilde{d}$ values is compared to the expected 68% an 95% CL intervals obtained in Sec. 7.7.

7.8.1 Generation of Pseudo-Data

The goal at the generation stage is to produce pseudo-datasets in which the average content of each contribution in every bin is the same as in the post-fit expected $\tilde{d} = 0$ distribution. The utilized pseudo-datasets are Asimov datasets generated with parameters that are varied according to pre-defined probability density functions for each dataset. For the normalization factors, including μ, a Gaussian distribution was chosen, centred around their respective post-fit values and with the width according to their post-fit uncertainty. The NPs associated to statistical uncertainties in individual bins are Poisson-distributed, such that the mean value of the NP is the post-fit value obtained in the expected $\tilde{d} = 0$ result. All other NPs are sampled from Gaussian distributions of unit width around the expected post-fit value.

The unit width is chosen to reflect that pre-fit uncertainties are used to sample the fit parameters. Since no pre-fit uncertainties are defined for the free NFs, the post-fit uncertainties are used instead. To correct for this inconsistency, Gaussian constraint terms are included in the likelihood for this study. The ΔNLL curve obtained with the thus changed likelihood function is displayed in Fig. 7.17. The difference is small since the normalization factors are not the leading sources of uncertainty in the fit. Therefore, the expected sensitivity to $\tilde{d}$ is largely unchanged.

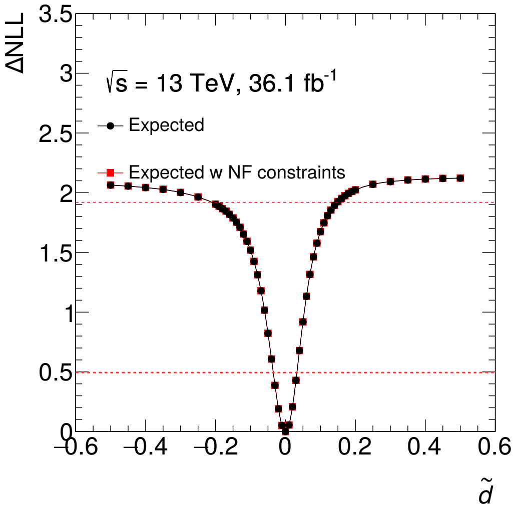

Figure 7.17: Comparison of expected ΔNLL curves obtained from combined fits with and without the inclusion of constraint terms on the NFs including μ.

7.8.2 Coverage Probability Measurement

Fits are conducted to all pseudo-datasets. After scanning the whole considered $\tilde{d}$ range, a best-fit value is determined for each of the 854 generated pseudo-datasets. Since the scan in $\tilde{d}$ is discrete but the expected limits are not, an interpolation is applied to more accurately determine the best-fit $\tilde{d}$ value. An example of the procedure is shown in Fig. 7.18a. The three neighbouring points in each direction of the minimum of the NLL curve are considered. A parabola is fitted to these six points and the minimum of the best-fit parabola is taken as best-fit $\tilde{d}$ value.

The distribution of best-fit $\tilde{d}$ values of the pseudo-datasets is shown in Fig. 7.18b. To test the validity of the expected 68% and 95% CL intervals on $\tilde{d}$ obtained using Eq. (7.2), the fraction of pseudo-datasets with a best-fit $\tilde{d}$ covered by these intervals is calculated.

The obtained fractions are 77.9% for the 68% CL interval and 95.7% for the 95% CL interval. The deviation from the expected coverage is found to be greater for the 68% CL interval despite the expected ΔNLL curve being approximately parabolic in that region, unlike the region around $|\tilde{d}| = 0.1$ which is included in the 95% CL interval. An explanation for this has not been found. But in both cases, the deviation is towards higher coverage, i.e. the uncertainty on $\tilde{d}$ is overestimated.

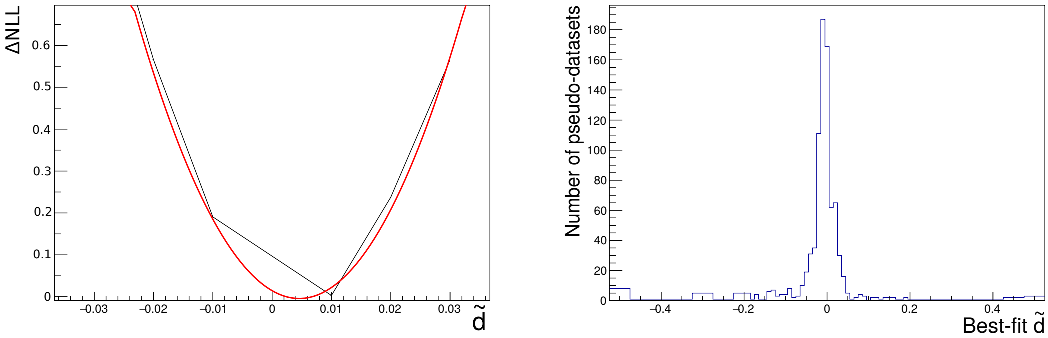

Figure 7.18: (a) Example interpolation of an NLL curve to mitigate the limitations of the discrete scan of $\tilde{d}$ values. (b) Distribution of best-fit $\tilde{d}$ values measured for the generated pseudo-datasets.

Therefore, the study shows that using Eq. (7.2) to obtain limits on $\tilde{d}$ may not be optimal, but is safe.

CHAPTER 8

Measurement of the $H \to \tau\tau$ Production Cross-Section with the Full Run-2 Dataset

A measurement of Higgs-boson production cross-sections for different production mechanisms using $H \to \tau\tau$ events in the full Run-2 dataset is currently being prepared. Instead of including the data taken in 2017 and 2018 and repeating the analysis presented in Ref. [120], many aspects of the analysis have been redesigned. As the analysis is still ongoing, no final results can be shown in this chapter. Instead, the focus is put on the developments in the $\tau_{\text{had}}\tau_{\text{had}}$ channel.

8.1 Analysis Overview

To a large extent, the simulated event samples used for the full Run-2 $H \to \tau\tau$ coupling analysis are produced in the same way as in the VBF $H \to \tau\tau$ CP measurement, which is described in Sec. 7.1. This applies to the simulation of ggF, VBF and VH $H \to \tau\tau$ events as well as V+jets and di-boson events. For the simulation of processes including top quarks, the method has changed.

The production of ttH, $t\bar{t}$ and single-top events is modelled using Powheg [105–107, 156–159] at NLO with the NNPDF2.3nlo [114] PDF set. The events are interfaced to Pythia 8 [113] using the A14 tune [116] and the NNPDF2.3nlo PDF set. Additionally, this analysis includes samples of ttV, 4-top and 3-top production events. These events are generated using MadGraph5_aMC@NLO [66] at NLO with the NNPDF3.1nlo PDF [114]. The events are interfaced with Pythia 8 [113] using the A14 tune and the NNPDF2.3lo [114] PDF set. The decays of bottom and charm hadrons in all samples are performed by EvtGen [117].

The goal of the analysis is to measure the ggF, VBF and VH Higgs-boson production cross-section. Additionally, a signal region aimed to measure the ttH cross-section is included only in the $\tau_{\text{had}}\tau_{\text{had}}$ channel. The event pre-selection in the $\tau_{\text{had}}\tau_{\text{had}}$ channel is summarized in Tab. 8.1.

Table 8.1: Summary of the event selection for the $\tau_{\text{had}}\tau_{\text{had}}$ channel. The selection in the Boost, VBF and VH regions is applied in addition to the preselection. The jet requirements of the ttH region replace the orthogonal requirements in the preselection definition.

Preselection	$N_{\text{leptons}} = 0$, $N_{\tau_{\text{had-vis}}} = 2$ $\tau_{\text{had-vis}}$ with medium RNN ID and OS $p_{\text{T}}(\tau_{\text{had-vis}}) > 40, 30$ GeV $\tau_{\text{had-vis}}$ candidates with 1 or 3 prongs leading jet $p_T > 70$ GeV, $\lvert\eta\rvert < 3.2$ $E_{\text{T}}^{\text{miss}} > 20$ GeV $0.6 < \Delta R(\tau, \tau) < 2.5$ $\Delta\eta(\tau, \tau) < 1.5$ $0.1 < x_1 < 1.4$, $0.1 < x_2 < 1.4$ Not ($N_{\text{jets}} \geq 5$ and $N_{b\text{-jets}} \geq 2$) and not ($N_{\text{jets}} \geq 6$ and $N_{b\text{-jets}} \geq 1$)
ttH category	($N_{\text{jets}} \geq 5$ and $N_{b\text{-jets}} \geq 2$) or ($N_{\text{jets}} \geq 6$ and $N_{b\text{-jets}} \geq 1$)
VBF inclusive	$m_{jj} > 350$ GeV, $\lvert\Delta\eta(j, j)\rvert > 3$ $\eta(j_1) \cdot \eta(j_2) < 0$ sub-leading jet $p_T > 30$ GeV $\eta(\tau_{\text{had-vis}})$ between η values of leading two jets
VH inclusive	60 GeV $< m_{jj} <$ 120 GeV sub-leading jet $p_T > 30$ GeV
Boost inclusive	Not VBF inclusive Not VH inclusive $p_{\text{T}}(\tau_1, \tau_2, E_{\text{T}}^{\text{miss}}) > 100$ GeV

The definition of the variables x_1 and x_2 is based on the collinear approximation for τ-lepton decays. With the notation $[\vec{p}(a) \times \vec{p}(b)]_z = p_x(a)p_y(b) - p_y(a)p_x(b)$ for the momenta of the objects a and b, they can be written as:

$$x_{1/2} = \frac{[\vec{p}(\tau_1) \times \vec{p}(\tau_2)]_z}{[\vec{p}(\tau_1) \times \vec{p}(\tau_2)]_z + [\vec{p}(E_{\text{T}}^{\text{miss}}) \times \vec{p}(\tau_{2/1})]_z} .$$

They describe the fraction of the p_{T} of the decaying τ lepton carried by the produced neutrino, under the assumptions that both the neutrino and the $\tau_{\text{had-vis}}$

object propagate in the same direction as the τ lepton that produced them and that the measured $E_{\mathrm{T}}^{\mathrm{miss}}$ only originates from the neutrinos produced in τ-lepton decays. As very low values or values of x greater than 1 indicate that the $E_{\mathrm{T}}^{\mathrm{miss}}$ does not originate from neutrinos produced in $\tau_{\text{had-vis}}$ decays, events with such values are rejected.

The trigger selection is listed in Tab. 8.2. In all years apart from 2015, the presence of a J25 object is required at L1. The expression "03dR30" in the names of the chains used in 2017 and 2018 describes a requirement on both $\tau_{\text{had-vis}}$ candidates at HLT to have $0.3 < \Delta R < 3.0$, which is introduced to further reduce the trigger rates without losing many $H \to \tau\tau$ signal events. Similarly, the expression "L1DR" specifies that the cut $(\Delta R(\text{TAU, J}))^2 > 2.0$ for both L1 $\tau_{\text{had-vis}}$ candidates with respect to the L1 jet candidate. This requirement is used to select events in which the mother particle of the two $\tau_{\text{had-vis}}$ candidates is produced in association with a QCD jet, which often leads to a large angular separation between the jet and the $\tau_{\text{had-vis}}$ candidates to cancel the p_{T} of the total final state. The RNN-based triggers are not used in 2018 despite slightly better efficiency on true $\tau_{\text{had-vis}}$ objects. This decision is made to ensure a uniform identification of $\tau_{\text{had-vis}}$ candidates, which simplifies the estimation of the Fake background described in Sec. 8.3.

Table 8.2: Trigger selection in the $\tau_{\text{had}}\tau_{\text{had}}$ channel.

Year	Trigger chain name
2015	tau35_medium1_tracktwo_tau25_medium1_tracktwo _L1TAU20IM_2TAU12IM
2016	tau35_medium1_tracktwo_tau25_medium1_tracktwo
2017	tau35_medium1_tracktwo_tau25_medium1_tracktwo _03dR30_L1DR_TAU20ITAU12I_J25
2018	tau35_medium1_tracktwoEF_tau25_medium1_tracktwoEF _03dR30_L1DR_TAU20ITAU12I_J25

The three inclusive signal regions Boost, VBF and VH each target different Higgs-boson production mechanisms. The Boost selection targets ggF Higgs-boson production in association with at least one jet. The increased p_{T} of the Higgs boson due to it recoiling against jets in the production helps separate it from background sources. Selecting an additional jet is also a necessity due to the trigger selection, which includes the presence of a jet candidate at L1. But the expected loss in sensitivity related to the absence of ggF events without any QCD jets is small.

The VBF inclusive selection is similar to how it was defined in Sec. 7.2. The VH inclusive selection targets VH events in which the vector boson decays hadronically and produces two jets, which leads to the applied cut on m_{jj} to cover both the Z-boson and W-boson mass windows. Events of VH production with leptonic decays of the vector bosons are not covered by the event selection of this analysis.

Additionally, a ttH region is defined with almost the same cuts as the preselection. The only difference is that a requirement on the number of b-tagged jet is applied using the 70% efficient working point of the DL1r b-jet tagger:

$$(N_{\text{jets}} \geq 5 \text{ and } N_{b\text{-jets}} \geq 2) \text{ or } (N_{\text{jets}} \geq 6 \text{ and } N_{b\text{-jets}} \geq 1) \,.$$

To avoid overlap, the inverse requirement is applied in the $\tau_{\text{had}}\tau_{\text{had}}$ preselection. The event distribution in dependence of $m_{\tau\tau}^{\text{MMC}}$ at preselection is shown in Fig. 8.1. As no estimation of the contribution from quark- or gluon-initiated jets misidentified as $\tau_{\text{had-vis}}$ objects is included, an underestimation of data is expected.

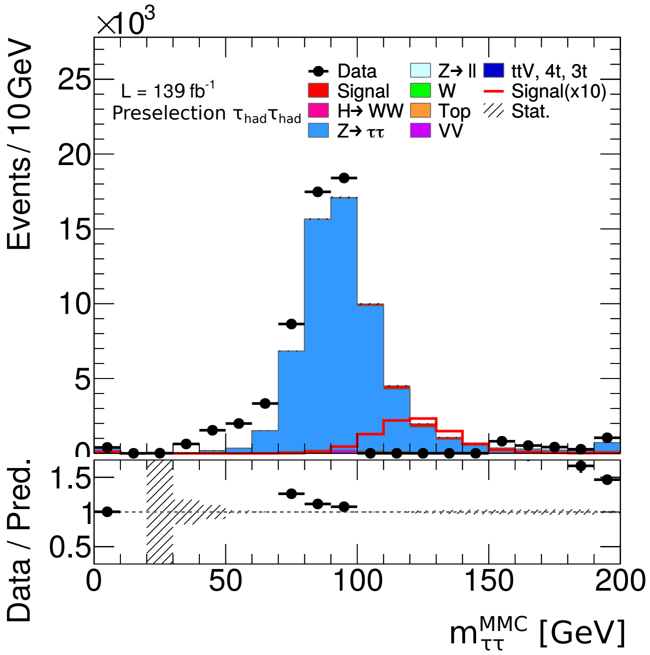

Figure 8.1: Event distribution in dependence of $m_{\tau\tau}^{\text{MMC}}$ at the $\tau_{\text{had}}\tau_{\text{had}}$ preselection. The data in the range 100 GeV $< m_{\tau\tau}^{\text{MMC}} <$ 150 GeV have been blinded. The contribution from misidentified $\tau_{\text{had-vis}}$ candidates has not been taken into account.

8.2 L1 Jet-Trigger Efficiency Measurement

As mentioned before, the di-τ triggers utilized in the $\tau_{\text{had}}\tau_{\text{had}}$ channel require the presence of a jet in addition to the two $\tau_{\text{had-vis}}$ candidates at L1. This is done to reduce the amount of candidate events passing the L1 threshold of the di-τ trigger chains without strongly reducing the efficiency on SM $H \to \tau\tau$ events. The modelling of jet energies at L1 is, however, not well-modeled. Therefore, a cut of 70 GeV has been applied on the p_{T} of the leading jet in Chap. 7, to remove the kinematic region in which the L1 jet trigger is not very efficient. As a first estimate, this cut value has been kept, but its validity has to be verified on the full Run-2 dataset and with varying trigger chains. This section describes the method employed to achieve this goal.

For practical reasons, the study of L1 jet-trigger efficiencies is based on the analysis presented in Chap. 6. For this, $\mu + \tau$ triggers with the same L1 jet requirement as the di-τ triggers used in the $\tau_{\text{had}}\tau_{\text{had}}$ channel of the $H \to \tau\tau$ analysis are investigated. The trigger chains used in the $\tau_{\text{had}}\tau_{\text{had}}$ channel in 2016, 2017 and 2018 have the same L1_J25 requirement as the $\mu + \tau$ chain

HLT_mu14_ivarloose_tau25_medium1_tracktwo_L1DR-MU10TAU12I_TAU12I-J25.

Using the $\mu+\tau$ chain to probe the efficiency of the J25 requirement allows to re-use the infrastructure of the $Z \to \tau\tau$ analysis described in Chap. 6. These chains were only introduced in 2016, to counteract the rising instantaneous luminosities and reduce the rates of events passing the trigger chains. Therefore, 2015 data are not included in this study.

The event selection from Sec. 6.2 is slightly modified to allow for a measurement of jets instead of $\tau_{\text{had-vis}}$ candidates. The adjustments to the selection are summarized in Tab. 8.3. Only events passing the HLT_tau25_medium1_tracktwo trigger as well as the already utilized combination of the HLT_mu26_ivarmedium and HLT_mu50 triggers are considered. Only the loose RNN-based τ-trigger ID working point is used, which increases the available event sample sizes without biasing the jet properties. Additionally, the offline $\tau_{\text{had-vis}}$ candidate is required to be geometrically matched to the HLT $\tau_{\text{had-vis}}$ object that fulfills the trigger requirements. The last change is that the presence of a jet with $p_{\text{T}} > 30$ GeV is required.

The background estimation is not changed with respect to that described in Sec. 6.3. The only change in the measurement of the efficiency ϵ is that it is calculated with respect to jets in this study:

$$\epsilon = \frac{N_{\text{jets}}(p_{\text{T}} > 30\text{ GeV, matched to L1\_J25 ROI})}{N_{\text{jets}}(p_{\text{T}} > 30\text{ GeV})}\,.$$

Table 8.3: List of adjustments made to the event selection described in Sec. 6.2 in order to conduct a measurement of the L1_J25 trigger leg. The symbol "-" is used when an additional requirement is placed for the L1_J25 efficiency measurement, since no cut had been replaced previously.

τ-trigger efficiency measurement	L1 jet-trigger efficiency measurement
Varying $\tau_{\text{had-vis}}$ ID criteria	Loose RNN ID
-	HLT_tau25_medium1_tracktwo(EF)
-	$p_{\text{T}}(j_1) > 30$ GeV

The true-τ MC is still treated as signal, while other contributions are subtracted from the data before calculating the efficiency of the trigger on data. This background subtraction is motivated by the original purpose of the analysis framework, which is to measure τ-trigger efficiencies, and likely not necessary for the estimation of jet efficiencies. It is, however, not expected that this procedure introduces a bias to the measurement.

The regions used for the numerator and denominator of the efficiency calculation are shown in Fig. 8.2, for events containing 1-prong $\tau_{\text{had-vis}}$ candidates. Given the good agreement between data and expectation in the denominator region shown in Fig. 8.2a, the sizable discrepancy between the yields in data and expectation at low jet p_{T} in Fig. 8.2b shows that the efficiency of the L1_J25 requirement is not modelled accurately.

As the efficiency of the L1_25 leg should not depend on the number of associated tracks of the $\tau_{\text{had-vis}}$ candidate, the event yields in both of these cases are combined. The background estimation is still conducted separately for 1- and 3-prong events, as described in Sec. 6.3, but the resulting yields are added up before calculating the jet efficiencies. As a dependence on the p_{T} as well as the η of the jet candidate is expected, the efficiencies are estimated as a function of both these quantities. The results are shown in Fig. 8.3. Subfigure (a) shows a strong dependence on the offline jet p_{T}, including a slow turn-on. Due to the poor energy resolution at L1, where no energy calibration can be applied, the efficiency does not reach 90% for p_{T} values below 80 GeV. Moreover, the deviation of the L1_J25 scale factor shown in the bottom panel of Fig. 8.3a from unity shows that the simulation does not reproduce the efficiencies measured in data events at low jet p_{T}. Subfigure (b) shows the dependence of the L1_J25 efficiency on the η value of the jet candidate, which is not as strong. The efficiency decreases for $|\eta| > 3.0$, which is due to the $|\eta| < 3.2$ requirement at L1 introduced by the L1_J25 leg.

The goal of the study is not to provide scale factors for the L1 leg of the $\mu + \tau$

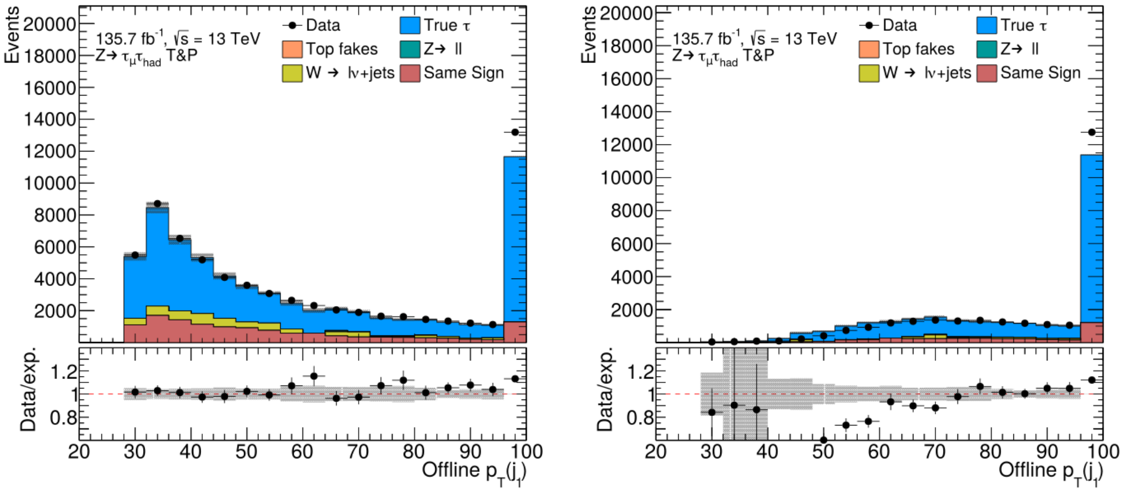

(a)

(b)

Figure 8.2: Event distribution as a function of p_{T} of the leading reconstructed jet measured in the study of L1 jet-trigger efficiencies, for events containing 1-prong $\tau_{\text{had-vis}}$ events. The distribution in (a) shows the distribution after requiring single-object muon and τ-lepton triggers, while the events shown in (b) are additionally required to pass the multi-leg $\mu + \tau$ trigger with the J25 requirement at L1. The distributions in these regions are used to calculate the efficiency of the jet leg of the trigger.

and di-τ chains, which would require the evaluation of systematic uncertainties on the measurement. Instead, only the estimation of plateau cuts to recommend to analyses using such triggers is intended. These cuts on p_{T} and η are introduced to avoid the regions where the efficiencies measured in data and simulation diverge strongly.

Since the efficiencies in p_{T} and η are correlated, the plateau cuts need to be determined iteratively by applying a cut on the first variable and determining an appropriate cut on the other. The final efficiency estimates from which the plateau cuts are obtained are shown in Fig. 8.4.

Based on these efficiencies, the final plateau cuts of $p_{\mathrm{T}} > 70$ GeV and $|\eta| < 3.2$ are derived. Despite not being fully efficient in the remaining phase-space, the deviation between the L1_J25 efficiencies in data and MC simulation is considered sufficiently small. This confirms the plateau cuts found for the previous iteration of the analysis documented in Ref. [120].

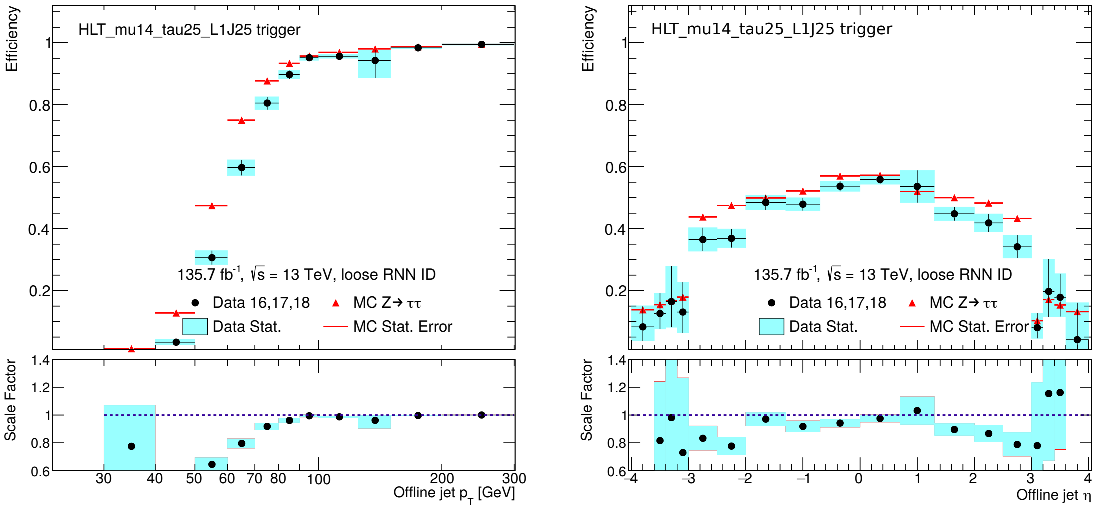

(a)

(b)

Figure 8.3: Measured L1_J25 trigger leg efficiencies in dependence of (a) the p_{T} and (b) the η value of the leading reconstructed offline jet. The lower panels show the ratio of efficiencies measured in data and simulation.

8.3 Background Estimation in the $\tau_{\text{had}}\tau_{\text{had}}$ Channel

With the event selection confirmed, an estimation method for the Fake background contribution can be developed. As a baseline, the nOS method used in Chap. 7 is implemented, with slight modifications. In order to improve upon this method, the usage of a fake-factor method is investigated. This section details the two methods and compares them with each other.

8.3.1 nOS Method

As described in Sec. 7.3, the nOS method is based on scaling a template for the distribution of fake events in dependence of the investigated variable. This template is obtained from a region with $q(\tau_1) \cdot q(\tau_2) \neq -1$. Additionally, the requirement on the number n of associated tracks is loosened with respect to the SR selection to $n \in \{1, 2, 3\}$. The construction of the Fake template for the MMC distribution in the nOS preselection region is illustrated in Fig. 8.5. All MC-estimated contributions, excluding $H \to \tau\tau$ processes, are subtracted from the data. This is done in order not to bias the cross-section measurement for the Higgs-boson production by inserting the SM assumption into the measurement. However, due to the small signal cross-sections, the omission of these processes is

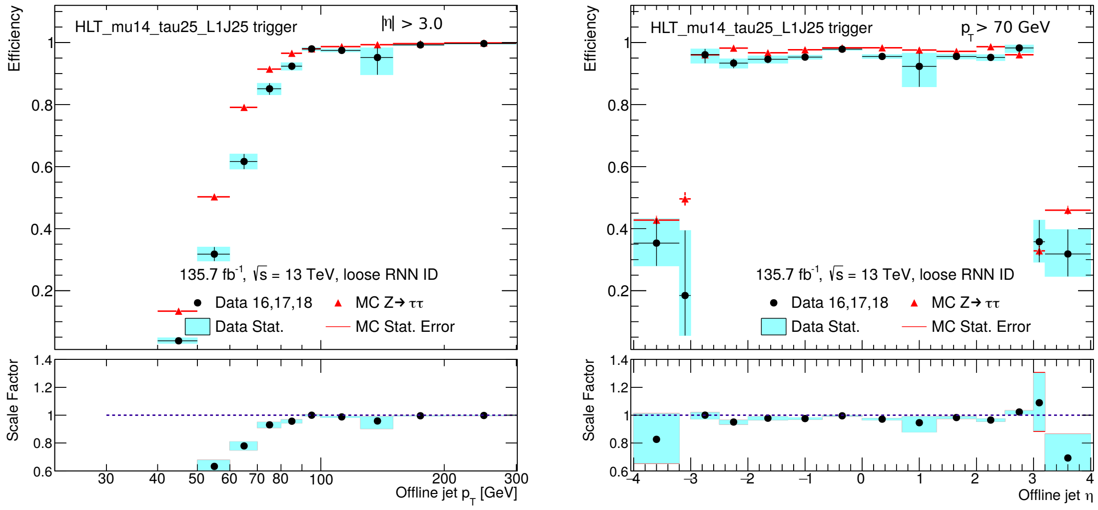

(a) (b)

Figure 8.4: Measured L1_J25 trigger leg efficiencies in dependence of (a) the p_{T} and (b) the η value of the leading reconstructed offline jet. The lower panels show the ratio of efficiencies measured in data and simulation.

not expected to strongly affect the Fake background estimation.

This method is used to estimate the contribution from events where both $\tau_{\text{had-vis}}$ candidates are misidentified quark- or gluon-initiated jets, also named “double-fake” events. This contribution is attributed mainly to QCD multi-jet events, but other processes such as $W \to qq'$+jets production can also give a minor contribution. In the nOS method, the contribution from processes with a true and a fake $\tau_{\text{had-vis}}$ object, named “single-fake” events, are estimated together with the events containing two true $\tau_{\text{had-vis}}$ objects using the MC simulation. Such events can be produced, for instance, from the $W \to \tau\nu_\tau$ process with radiation of additional jets or processes involving top-quark production.

In order to find an appropriate scaling factor, named r_{QCD}, to estimate the absolute number of Fake events in the SR, the SR cut $\Delta\eta(\tau,\tau) < 1.5$ is loosened to $\Delta\eta(\tau,\tau) < 2$, which increases the relative contribution of double-fake events. In this selection, the scaling factor is determined to be

$$r_{\mathrm{QCD}} = \frac{(N_{\mathrm{Data}} - N_{\mathrm{MC}})_{\mathrm{OS}}}{(N_{\mathrm{Data}} - N_{\mathrm{MC}})_{\mathrm{nOS}}} = \frac{89032 - 68172.8}{41689 - 8101.8} = 0.62\,.$$

The comparison of the distribution of $m_{\tau\tau}^{\mathrm{MMC}}$ values in data and expectation based on the nOS method is shown in Fig. 8.6. As the analysis is still ongoing, the distribution of data in the window $m_{\tau\tau}^{\mathrm{MMC}}$ [GeV] $\in [100, 150]$ are not shown.

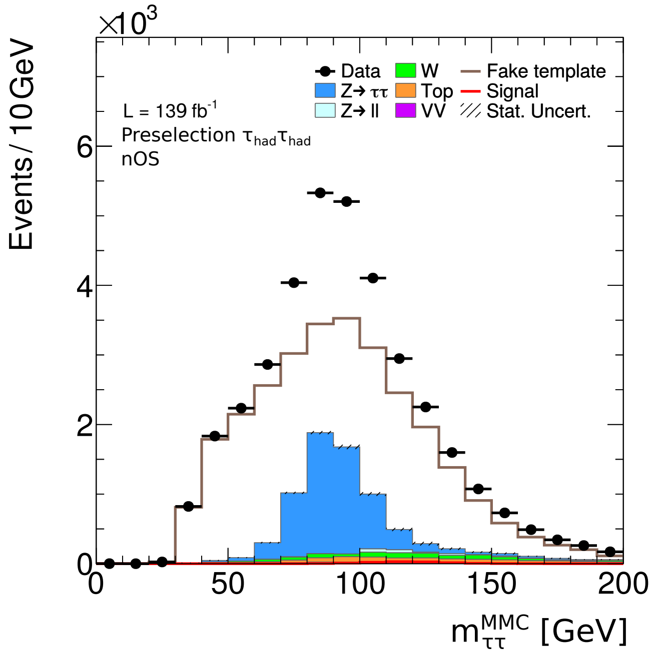

Figure 8.5: Event distribution in the nOS preselection in dependence of the $m_{\tau\tau}^{\mathrm{MMC}}$ mass estimate. The Fake template is constructed by subtracting the contribution from events containing at least one true $\tau_{\text{had-vis}}$ object as estimated by MC simulation from the measured data distribution. In order to better visualize the shape of the resulting Fake template histogram, it is not stacked on top of the contributions from the simulated event samples.

This procedure, named “blinding,” is introduced to avoid biasing the definition of analysis regions. The modelling in $m_{\tau\tau}^{\mathrm{MMC}}$ is mostly good, apart from the region $m_{\tau\tau}^{\mathrm{MMC}} < 70$ GeV, where the data yield is underestimated. For these low $m_{\tau\tau}^{\mathrm{MMC}}$ values, the relative Fake contribution is the largest, which suggests that the deviation is caused by an imperfect Fake estimation.

8.3.2 Fake-Factor Method

Several shortcomings of the nOS method have been observed in this analysis.

- Mismodelling at low $m_{\tau\tau}^{\mathrm{MMC}}$ values at preselection.
- The template for the Fake background is constructed inclusively for 1-prong and 3-prong $\tau_{\text{had-vis}}$ candidates from the nOS region, and cannot be split into

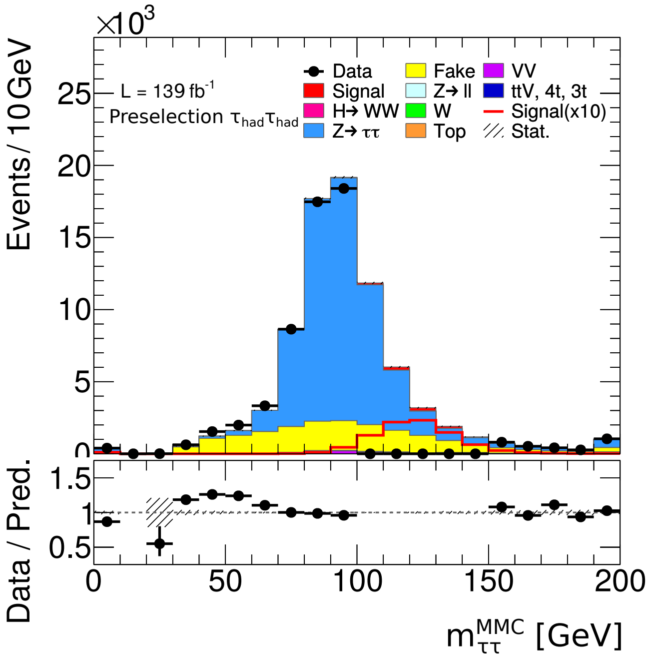

Figure 8.6: Event distribution in the SR preselection in dependence of the $m_{\tau\tau}^{\text{MMC}}$ mass estimate with the Fake contribution estimated with the nOS method. The data with $m_{\tau\tau}^{\text{MMC}}$ values in the range $[100, 150]$ have been blinded.

1-prong and 3-prong contributions due to the presence of 2-prong candidates in the nOS region.

- Sizable contamination of true $\tau_{\text{had-vis}}$ objects in the nOS selection.
- No standardized measurements of the performance of simulated samples for 2-prong $\tau_{\text{had-vis}}$ candidates with results provided for all ATLAS analyses, which complicates the treatment of systematic uncertainties on the method.
- Small sample size in the nOS selection, leading to statistical fluctuations in the bin contents of the template constructed to estimate event distributions of the Fake contribution in the SRs.

In order to improve on as many of these shortcomings as possible, the usage of a method based on fake-factors has been investigated.

Introduction to Fake-Factors

The main feature of a fake-factor method is the usage of a region with inverted $\tau_{\text{had-vis}}$-candidate ID to construct a template of the event distribution of the Fake background in dependence of different variables in the SR. By scaling the events in this region with the appropriate fake-factors, the Fake contribution is estimated.

The ID requirement in the SR is the medium RNN-based working point, which is applied to both $\tau_{\text{had-vis}}$ candidates. This requirement is inverted by requiring one of the two $\tau_{\text{had-vis}}$ candidates to fail the medium ID requirement, which defines the "anti-ID" region. Due to a central pre-processing step of the available samples provided by ATLAS, no events are available in which both $\tau_{\text{had-vis}}$ candidates fail both the BDT-based and the RNN-based loose ID criteria. Therefore, in order not to rely on the obsolete BDT-based ID criteria, the minimal cut of at least one of the $\tau_{\text{had-vis}}$ candidates passing the loose RNN ID is added to the definition of the anti-ID region. The $m_{\tau\tau}^{\text{MMC}}$ distribution in the anti-ID region is shown in Fig. 8.7.

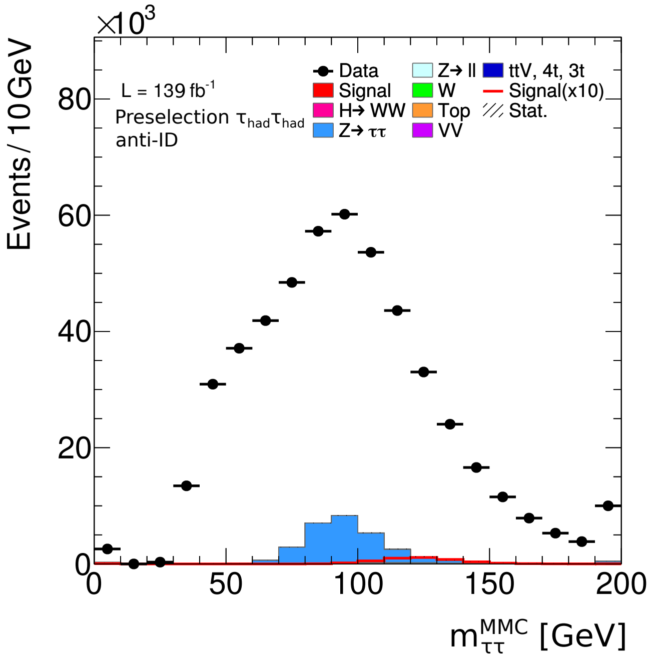

Figure 8.7: Event distribution in the anti-ID preselection region in dependence of the $m_{\tau\tau}^{\text{MMC}}$ mass estimate.

For a comparison with the nOS region, the value corresponding to r_{QCD} using the anti-ID region is calculated at preselection with the loosened cut $\Delta\eta < 2.0$, to be consistent with the previous calculation of r_{QCD}:

$$r_{\text{QCD}}^{\text{anti-ID}} = \frac{(N_{\text{Data}} - N_{\text{MC}})_{\text{SR}}}{(N_{\text{Data}} - N_{\text{MC}})_{\text{anti-ID}}} = \frac{89032 - 68172.8}{571657 - 30702.1} = 0.039\ .$$

This comparison shows that the fraction of true $\tau_{\text{had-vis}}$ objects in the anti-ID region is smaller than in nOS, and that the available number of events is much larger. Additionally, no 2-prong $\tau_{\text{had-vis}}$ candidates are included in the anti-ID region, making this region a promising candidate for usage in the Fake estimate.

However, the $\tau_{\text{had-vis}}$ ID is known to bias the p_{T} distribution of rejected $\tau_{\text{had-vis}}$ candidates. This is demonstrated in Fig. 8.8, where the ratio of rejected over accepted fake-$\tau_{\text{had-vis}}$ candidates by the medium BDT and RNN ID requirement is shown in dependence of p_{T}. As the ratio increases with p_{T}, a template of the p_{T} distribution of fake-$\tau_{\text{had-vis}}$ candidates obtained from the anti-ID region will have a lower mean than the fake-$\tau_{\text{had-vis}}$ distribution to be estimated in the SR. In order to counteract this bias, the scaling factors applied to the anti-ID template to construct the SR Fake-background estimate must be dependent on p_{T}.

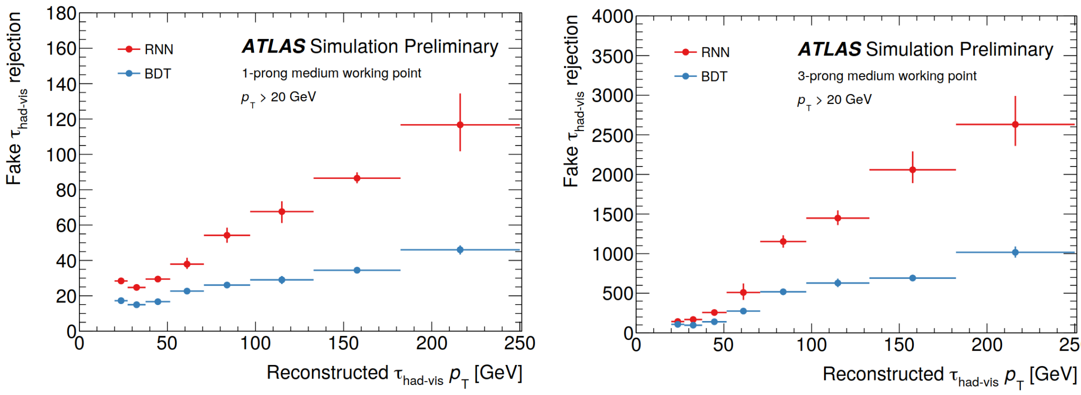

Figure 8.8: Number of rejected fake-$\tau_{\text{had-vis}}$ candidates with 1 or 3 associated tracks per fake-$\tau_{\text{had-vis}}$ candidate passing the medium working point of either the BDT-based or RNN-based ID algorithm, in dependence of the p_{T} of the candidate. The higher the p_{T} value is, the higher the rejection power is. This effect is enhanced for the RNN-based ID [100].

Fake-Factor Measurement

The fake-factors are derived in a region enriched in W+jets events, named $\tau_{\text{lep}}\tau_{\text{had}}$ W+jets CR. For practical reasons, the dataset used in Sec. 8.2 is re-used for the fake-factor measurement. Thus, only events with a muon and a $\tau_{\text{had-vis}}$ candidates in the final state are included. The event selection is given in Tab. 8.4. The cut that enhances the relative contribution of W+jets events is $m_{\mathrm{T}} > 70$ GeV, as for the W+jets CR in the $Z \to \tau\tau$ trigger efficiency measurement in Sec. 6.2.

Table 8.4: Summary of the event selection for the W+jets CR in the $\tau_{\mathrm{lep}}\tau_{\mathrm{had}}$ channel used for the measurement of fake-factors applied in the $\tau_{\mathrm{had}}\tau_{\mathrm{had}}$ channel.

W+jets CR	$N_{\mu} = 1, N_{\tau_{\text{had-vis}}} = 1,\ q(\mu) \cdot q(\tau_{\text{had-vis}}) = -1$
	$\tau_{\text{had-vis}}$ ID: medium RNN
	μ ID: medium
	$p_{\mathrm{T}}(\mu) > 21$ GeV, threshold depending on year
	$p_{\mathrm{T}}(\tau_{\text{had-vis}}) > 30$ GeV
	$m_{\mathrm{T}} > 70$ GeV
	$\tau_{\text{had-vis}}$ candidates with 1 or 3 prongs
	leading jet $p_T > 40$ GeV
	$N_{b\text{-jets}} = 0$
	$E_{\mathrm{T}}^{\mathrm{miss}} > 20$ GeV
	$0.6 < \Delta R_{\mu\tau} < 2.5$
	$\Delta\eta_{\mu\tau} < 1.5$
	$0.1 < x_1 < 1.4$, $0.1 < x_2 < 1.2$

Single-muon triggers are utilized in this region. As the HLT p_{T} thresholds of these have changed throughout Run 2, the offline p_{T} cut on the muon is also adjusted. In 2015, the HLT threshold was at 20 GeV, while for the rest of the Run-2 dataset, it was at 26 GeV. Therefore, the offline plateau cuts are at 21 GeV in 2015 and at 27.3 GeV in 2016 through 2018. In addition, the single-τ trigger requirement HLT_tau25_medium1_tracktwo is applied for 2015, 2016 and 2017 events, while the HLT_tau25_medium1_tracktwoEF trigger is applied for 2018 events. This is done in order to make the selection of $\tau_{\text{had-vis}}$ candidates more similar to that in the SR of the $\tau_{\mathrm{had}}\tau_{\mathrm{had}}$ channel.

To increase the sample size in the control regions, the leading jet p_{T} cut in the $\tau_{\mathrm{lep}}\tau_{\mathrm{had}}$ channel was kept at 40 GeV despite being at 70 GeV in the $\tau_{\mathrm{had}}\tau_{\mathrm{had}}$ channel. The $|\eta| < 3.2$ cut on the leading jet was applied and later removed for the same reason. This was only done after verifying that it does not bias the fake-factor calculation, which was done by calculating fake-factors with and without applying the additional p_{T} and $|\eta|$ cuts and confirming the compatibility of the results.

For deriving the fake-factors, different $\tau_{\text{had-vis}}$ ID criteria are applied to the W+jets CR. The two types of fake-factors used for the $\tau_{\mathrm{had}}\tau_{\mathrm{had}}$ channel Fake-background estimation are named "not-medium" (nm) fake-factor F^{nm} and "loose-not-medium" (lnm) fake-factor F^{lnm}. They are defined as follows:

$$F^{\text{nm}} = (N_{\text{Data}} - N_{\text{MC}})^{W\ \text{CR}}_{\text{medium}\ \tau} / (N_{\text{Data}} - N_{\text{MC}})^{W\ \text{CR}}_{\text{not-medium}\ \tau}$$

$$F^{\text{lnm}} = (N_{\text{Data}} - N_{\text{MC}})^{W\ \text{CR}}_{\text{medium}\ \tau} / (N_{\text{Data}} - N_{\text{MC}})^{W\ \text{CR}}_{\text{loose-not-medium}\ \tau}\ .$$

The symbol N_{MC} represents the contribution from simulated processes that include a $\tau_{\text{had-vis}}$ candidate that has been matched to a truth-level $\tau_{\text{had-vis}}$ object, again with the exception of $H \to \tau\tau$ events. In order to derive the fake-factors, the medium working point is applied in the numerator. For the denominator of F^{nm}, the ID requirement is inverted, while for the denominator of F^{lnm}, it is also inverted but an additional minimum requirement of the $\tau_{\text{had-vis}}$ candidate passing the loose working point is applied. The $p_{\text{T}}(\tau_{\text{had-vis}})$ distributions in these three regions are shown in Fig. 8.9. The two types of fake-factors are necessary due to the aforementioned minimum ID cut in the $\tau_{\text{had}}\tau_{\text{had}}$ anti-ID region, as will be further detailed later on in this section.

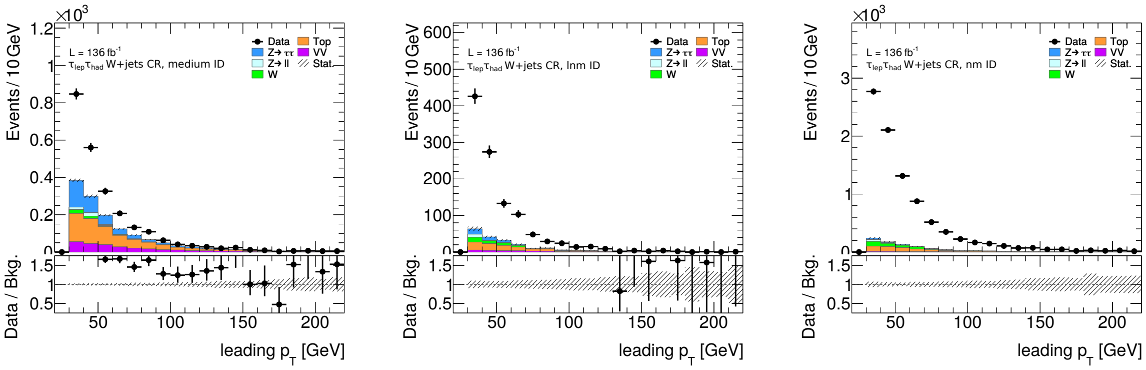

(a) (b) (c)

Figure 8.9: Event distributions in dependence of $p_{\text{T}}(\tau_{\text{had-vis}})$ in the W+jets CR of the $\tau_{\text{lep}}\tau_{\text{had}}$ channel. The RNN-based ID requirement applied to the $\tau_{\text{had-vis}}$ candidate is (a) medium, (b) loose-not-medium and (c) not-medium.

By calculating the ratios of event yields in the W+jets CR with different ID criteria applied, the fake-factors are determined. The fake-factors are separated between 1-prong and 3-prong $\tau_{\text{had-vis}}$ candidates. A dependence on the p_{T} of the $\tau_{\text{had-vis}}$ candidate is expected based on Fig. 8.8, but an additional dependence on the absolute value of its pseudorapidity $|\eta|$ has been observed. Therefore, a two-dimensional parametrization is employed, with three bins in $p_{\text{T}}(\tau_{\text{had-vis}})$ and two in $|\eta(\tau_{\text{had-vis}})|$. The resulting fake-factors are shown in Fig. 8.10. The falling trend of F^{nm} with p_{T} shown in Fig. 8.10a counteracts the rise in rejection power of the medium ID working point shown in Fig. 8.8.

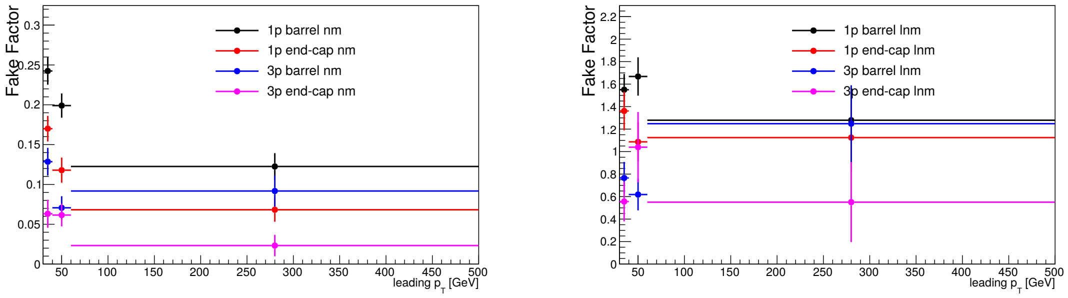

(a) (b)

Figure 8.10: Fake-factors measured in the $\tau_{\text{lep}}\tau_{\text{had}}$ W+jets CR, with (a) not-medium (nm) or (b) loose-not-medium (lnm) ID requirement in the denominator region. The calculation is separated in fake-factors for $\tau_{\text{had-vis}}$ candidates in the barrel of the detector ($|\eta| < 1.37$) and fake-factors for end-cap ($|\eta| > 1.52$) $\tau_{\text{had-vis}}$ candidates.

Fake-Factor Application

The fake-factors can be applied to estimate the number of fake $\tau_{\text{had-vis}}$ candidates passing the SR selection in the $\tau_{\text{had}}\tau_{\text{had}}$ channel. For this, the number of events passing (P) the $\tau_{\text{had-vis}}$ candidate selection in the SR is decomposed into all possible combinations of true (T) and fake (F) $\tau_{\text{had-vis}}$ candidates:

$$\tau_1^P \tau_2^P = \tau_1^T \tau_2^T + \tau_1^T \tau_2^F + \tau_1^F \tau_2^T + \tau_1^F \tau_2^F \,. \tag{8.1}$$

Here, the indices 1 and 2 specify the leading and sub-leading $\tau_{\text{had-vis}}$ candidates in p_{T}. The nOS method covers only the last contribution $\tau_1^F \tau_2^F$ from double-fake events, while the single-fake contributions are estimated from simulation.

In order to estimate the double-fake contribution with fake-factors, candidates failing the medium ID working point (anti-ID, A) are used. Given the definition of the fake-factor F^i associated with the $\tau_{\text{had-vis}}$ candidate i, the quantity τ_i^F can be estimated from the anti-ID selection by applying the appropriate fake-factor, i.e. $\tau_i^F = F^i \tau_i^A$. This leads to

$$\tau_1^F \tau_2^F = F^1 F^2 \tau_1^A \tau_2^A \,.$$

Analogously, fake-factors also allow for the estimation of the single-fake contribution:

$$\begin{aligned}
F^1\tau_1^A\tau_2^P &= \tau_1^F\tau_2^F + \tau_1^T\tau_2^F \\
F^2\tau_1^A\tau_2^P &= \tau_1^F\tau_2^F + \tau_1^F\tau_2^T \\
\Rightarrow \tau_1^T\tau_2^F + \tau_1^F\tau_2^T &= F^2\tau_1^P\tau_2^A + F^1\tau_1^A\tau_2^P - 2\tau_1^F\tau_2^F \\
&= F^2\tau_1^P\tau_2^A + F^1\tau_1^A\tau_2^P - 2F^1F^2\tau_1^A\tau_2^A\ .
\end{aligned}$$

With these expressions, Eq. (8.1) can be rewritten as:

$$\tau_1^P\tau_2^P = \tau_1^T\tau_2^T + F^2\tau_1^P\tau_2^A + F^1\tau_1^A\tau_2^P - F^1F^2\tau_1^A\tau_2^A\ . \tag{8.2}$$

The contribution to the SR from events containing two true $\tau_{\text{had-vis}}$ objects, $\tau_1^T\tau_2^T$, is estimated using the simulated event samples described in Sec. 8.1. To avoid double-counting between the samples and the data-driven fake-factor estimate, both $\tau_{\text{had-vis}}$ candidates in simulated events are required to be geometrically matched to a truth-level $\tau_{\text{had-vis}}$ object. The application of fake-factors based on Eq. (8.2) is visualized in Fig. 8.11.

Due to the removal of events with two $\tau_{\text{had-vis}}$ candidates failing the loose ID working point, the region for the estimation of the term $\tau_1^A\tau_2^A$ has to be divided into two subregions in which either the leading or the sub-leading $\tau_{\text{had-vis}}$ satisfies the loose RNN ID working point. The events in these subregions are then scaled by either $F^{\text{lnm}}(\tau_1)\cdot F^{\text{nm}}(\tau_2)$ if they are part of the region marked in orange in Fig. 8.11 or $F^{\text{nm}}(\tau_1)\cdot F^{\text{lnm}}(\tau_2)$ if they are part of the subregion marked in green. Given their definition, however, the product $F^{\text{lnm}}(\tau_1)\cdot F^{\text{nm}}(\tau_2)$ will scale the region with loose-not-medium leading and not-medium sub-leading $\tau_{\text{had-vis}}$ candidates, marked in orange in Fig. 8.11, to the full expected fake yield in the SR, while the product $F^{\text{nm}}(\tau_1)\cdot F^{\text{lnm}}(\tau_2)$ will do the same for the region marked in green. This would result in an overestimation of this part of the Fake contribution by a factor of two, which is resolved by multiplying the applied product of two fake-factors by $\frac{1}{2}$. Events from the anti-ID region where both $\tau_{\text{had-vis}}$ candidates fulfill the loose ID criterion are scaled by $\frac{1}{2}(F^{\text{lnm}}(\tau_1)\cdot F^{\text{nm}}(\tau_2) + F^{\text{nm}}(\tau_1)\cdot F^{\text{lnm}}(\tau_2))$ to account for these events being part of two template regions: the ones marked in green and orange in Fig. 8.11.

The modelling of $m_{\tau\tau}^{\text{MMC}}$ in the SR preselection based on the fake-factor method is displayed in the event distribution shown in Fig. 8.12. Comparing it to the analogous Fig. 8.6 obtained with the nOS method shows that the mismodelling at low $m_{\tau\tau}^{\text{MMC}}$ values is reduced. Moreover, the statistical uncertainty on the prediction of the Fake background is also reduced. This shows that all weaknesses of the nOS method listed at the start of this section are improved upon with the fake-factor method.

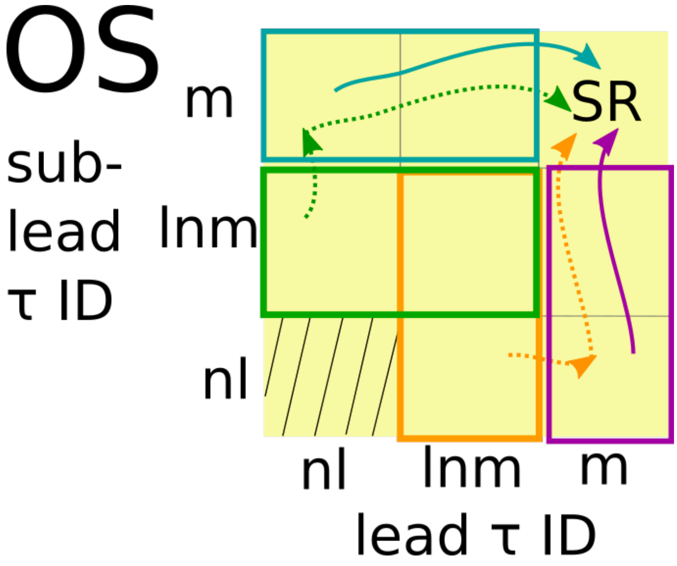

Figure 8.11: Pictorial representation of the fake-factor application for the Fake background estimate in the $\tau_{\text{had}}\tau_{\text{had}}$ channel. The opposite-sign events are separated into four subregions based on whether the leading and sub-leading $\tau_{\text{had-vis}}$ candidate in an event passes the medium (m), the loose but not the medium (lnm) or not the loose (nl) ID working point. Short arrows represent F^{lnm}, while long arrows represent F^{nm}. Positive contributions to the SR are represented by solid arrows, while negative contributions are represented by dotted arrows.

8.4 Systematic Uncertainties on the Method

Three sources of uncertainty are considered for the fake-factor estimation: the statistical uncertainty on the measured fake-factors, the effect of the choice of parametrization and possible differences in composition of the Fake background in the SR and the CR used to derive the fake-factors. This section describes how the impact of these sources on the final Fake estimate is assessed.

8.4.1 Statistical Uncertainty on the Fake-Factors

The first type of uncertainty covers the statistical uncertainties on the fake-factors calculated in the W+jets CR. They are implemented by varying the fake-factors by one standard deviation of the statistical uncertainty originating from the limited sample size in the W+jets CRs. The F_{nm} and F_{lnm} are varied separately, as well as the fake-factors for 1-prong and 3-prong $\tau_{\text{had-vis}}$ candidates, so there are four systematic variations in total to cover for statistical uncertainties from the W+jets

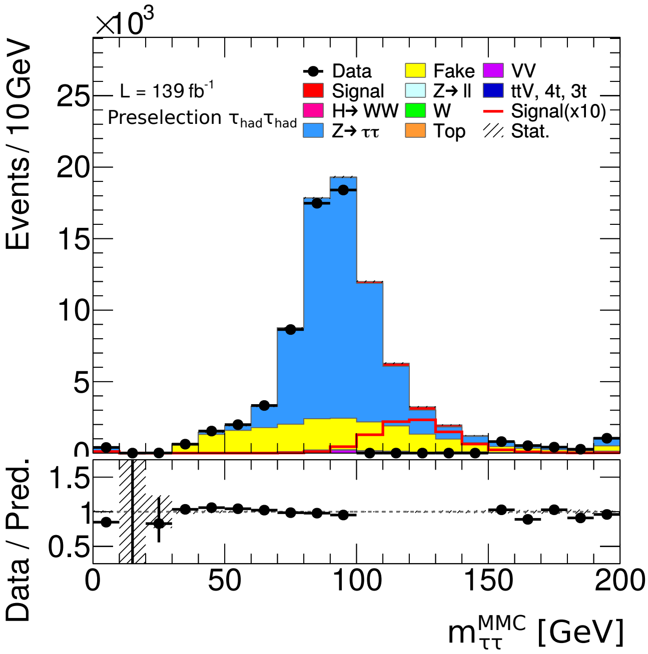

Figure 8.12: Event distribution in the SR preselection in dependence of the $m_{\tau\tau}^{\mathrm{MMC}}$ mass estimate with the Fake contribution estimated with the fake-factor method.

CRs. They are named "hh_fake_ff_stat_(1p/3p)_(nm/lnm)" depending on the event selection in the calculation region, and their impact on the predicted fake-$\tau_{\text{had-vis}}$ contribution is shown in Fig. 8.13, only containing the impact of increasing the fake-factor by its uncertainty. The evaluations of the various sources of uncertainty are based on the $m_{\tau\tau}^{\mathrm{MMC}}$ distribution, which is also planned to be included in the likelihood fit for the cross-section measurement As for the estimation of the other uncertainties, the impact of the opposite variation is obtained by symmetrizing the variation with respect to the nominal estimate. Since the F_{lnm} are only applied in the part of the template that is subtracted in the fake estimation according to Eq. (8.2), increasing them leads to a decrease in the estimated fake contribution. The impact is around 10% for the 1-prong and 5% for the 3-prong fake-factors.

8.4.2 Parametrization Uncertainty

The second type of uncertainty covers the limitations of the parametrization of the fake-factors. The first step to quantify these limitations is using the same coarse binning applied in the W+jets CR to derive fake-factors in the same-sign

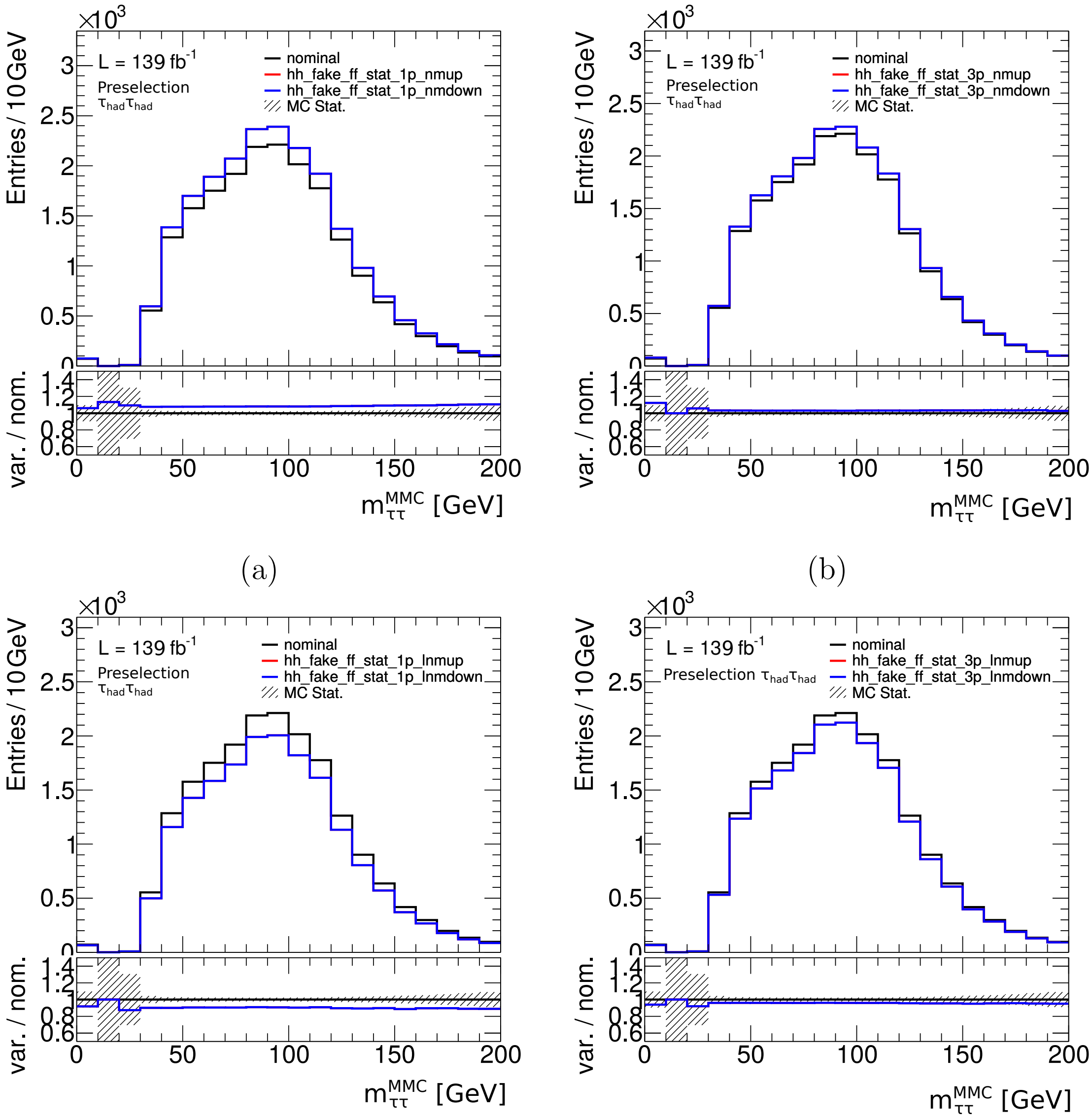

(a) (b)

(c) (d)

Figure 8.13: Impact of the statistical uncertainty of the fake-factor measurement on the estimated $m_{\tau\tau}^{\text{MMC}}$ distribution of the Fake contribution in the SR preselection. The statistical variations are evaluated separately for (a) 1-prong F_{nm}, (b) 3-prong F_{nm}, (c) 1-prong F_{lnm} and (d) 3-prong F_{lnm}.

signal region, which is chosen due to its large sample size. These fake-factors are calculated in control regions with one $\tau_{\text{had-vis}}$ candidate passing and the other failing the medium ID working point. The following calculations are made to obtain separate fake-factors for the leading and sub-leading $\tau_{\text{had-vis}}$ candidate in an event from the same-sign region:

$$\begin{aligned}
F_1^{\text{nm}} &= (N_{\text{Data}} - N_{\text{MC}})^{\text{SS}}_{\text{medium }\tau_1} / (N_{\text{Data}} - N_{\text{MC}})^{\text{SS}}_{\text{not}-\text{medium }\tau_1}\Big|_{\text{medium }\tau_2} \\
F_2^{\text{nm}} &= (N_{\text{Data}} - N_{\text{MC}})^{\text{SS}}_{\text{medium }\tau_2} / (N_{\text{Data}} - N_{\text{MC}})^{\text{SS}}_{\text{not}-\text{medium }\tau_2}\Big|_{\text{medium }\tau_1} \\
F_1^{\text{lnm}} &= (N_{\text{Data}} - N_{\text{MC}})^{\text{SS}}_{\text{medium }\tau_1} / (N_{\text{Data}} - N_{\text{MC}})^{\text{SS}}_{\text{loose}-\text{not}-\text{medium }\tau_1}\Big|_{\text{medium }\tau_2} \\
F_2^{\text{lnm}} &= (N_{\text{Data}} - N_{\text{MC}})^{\text{SS}}_{\text{medium }\tau_2} / (N_{\text{Data}} - N_{\text{MC}})^{\text{SS}}_{\text{loose}-\text{not}-\text{medium }\tau_2}\Big|_{\text{medium }\tau_1} .
\end{aligned} \tag{8.3}$$

Since the parametrization of the fake-factors from the $\tau_{\text{lep}}\tau_{\text{had}}$ W+jets CR cannot distinguish between leading and sub-leading $\tau_{\text{had-vis}}$ candidate, F_1 and F_2 are combined by adding up the numerator and denominator events of the leading and sub-leading $\tau_{\text{had-vis}}$ CR before calculating the ratio. This is done to emulate the parametrization of the nominal fake-factors as accurately as possible.

The same-sign CR fake-factors are then applied to the same-sign anti-ID region using the same binning as the $\tau_{\text{lep}}\tau_{\text{had}}$ W+jets CR fake-factors. These fake-factors are shown in Fig. 8.14, and they are used to produce a fake estimate in the same-sign region and test the closure of the $m_{\tau\tau}^{\text{MMC}}$ distribution in the same-sign region.

Again, the $m_{\tau\tau}^{\text{MMC}}$ distribution is chosen, and the ratio of data over prediction is applied as an additional weight for the fake events to construct the parametrization uncertainty variation. This is meant to cover the uncertainty of the fake-factor method that arises from limitations in the fake-factor parametrization. The weight distribution and the resulting variation ("hh_fake_ff_param") are shown in Fig. 8.15. The impact is small, showing that the six bins used in the default parametrization take most of the dependence of the fake-factors on the properties of an event and its objects into account.

8.4.3 Composition of the Fake Background

The last type of systematic variation aims at covering the uncertainty that stems from differences in the background composition between the regions where the fake-factors are measured and applied. Since the fake-factors vary for $\tau_{\text{had-vis}}$ candidates faked by light quarks (u, d, s), gluons and heavier quarks (c, b), a different background composition in the control regions can lead to over- or underestimation of the Fake background in the signal region. To account for this, fake-factors are derived in three different fake-enriched regions: the $\tau_{\text{lep}}\tau_{\text{had}}$ W+jets CR and the $\tau_{\text{had}}\tau_{\text{had}}$ high-$\Delta\eta(\tau_{\text{had-vis}}, \tau_{\text{had-vis}})$ and same-sign regions. The high-$\Delta\eta$ region

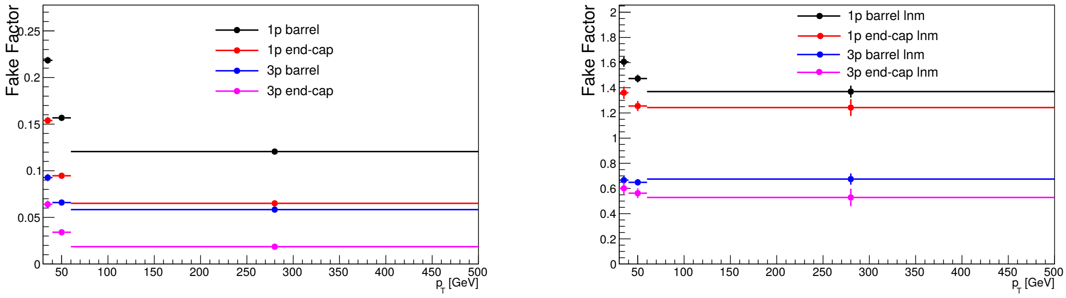

(a) (b)

Figure 8.14: Fake-factors measured in the $\tau_{\text{had}}\tau_{\text{had}}$ same-sign preselection CR, with (a) not-medium and (b) loose-not-medium ID requirement in the denominator, using the same parametrization as the nominal fake-factors. The calculation is separated in fake-factors for $\tau_{\text{had-vis}}$ candidates in the barrel of the detector ($|\eta| < 1.37$) and fake-factors for end-cap ($|\eta| > 1.52$) $\tau_{\text{had-vis}}$ candidates.

is constructed by requiring $1.5 < \Delta\eta(\tau,\tau) < 2.0$, while the same-sign region is defined with $q(\tau_1)q(\tau_2) = +1$. Apart from these cuts, the event selection for these regions is the same as for the signal region.

Since all these regions have different sample sizes, each set of fake-factors is parametrized differently. The W+jets CR parametrization has been shown before. The fake-factors from the $\tau_{\text{had}}\tau_{\text{had}}$ channel are derived using Eq. (8.3). In the same-sign case, F^1_{nm} and F^2_{nm} for the leading and sub-leading $\tau_{\text{had-vis}}$ candidate were found to be compatible and thus combined. This was not the case for F_{lnm}, but the dependence on p_T was found to be small, so a 1D binning in $|\eta|$ is applied for these. None of the fake-factors measured in the high-$\Delta\eta$ region were combined and they are all parametrized in p_T as well as $|\eta|$. The resulting fake-factors can be seen in Fig. 8.16.

These fake-factors are applied in the same way as in the nominal case, except that in the cases where leading and sub-leading $\tau_{\text{had-vis}}$ fake-factors are not combined, which are applied then only to the appropriate candidates. The impact of changing the fake-factor source region from the $\tau_{\text{lep}}\tau_{\text{had}}$ W+jets CR to either the $\tau_{\text{had}}\tau_{\text{had}}$ same-sign (“hh_fake_ff_composition_ss”) or high-$\Delta\eta$ region (“hh_fake_ff_composition_highdeta”) at preselection is shown in Fig. 8.17.

The usage of fake-factors from the high-$\Delta\eta$ region instead of the $\tau_{\text{lep}}\tau_{\text{had}}$ W+jets CR does not impact the estimated $m^{\text{MMC}}_{\tau\tau}$ distribution strongly, showing that the composition of Fake backgrounds is similar in these two regions. Using the same-

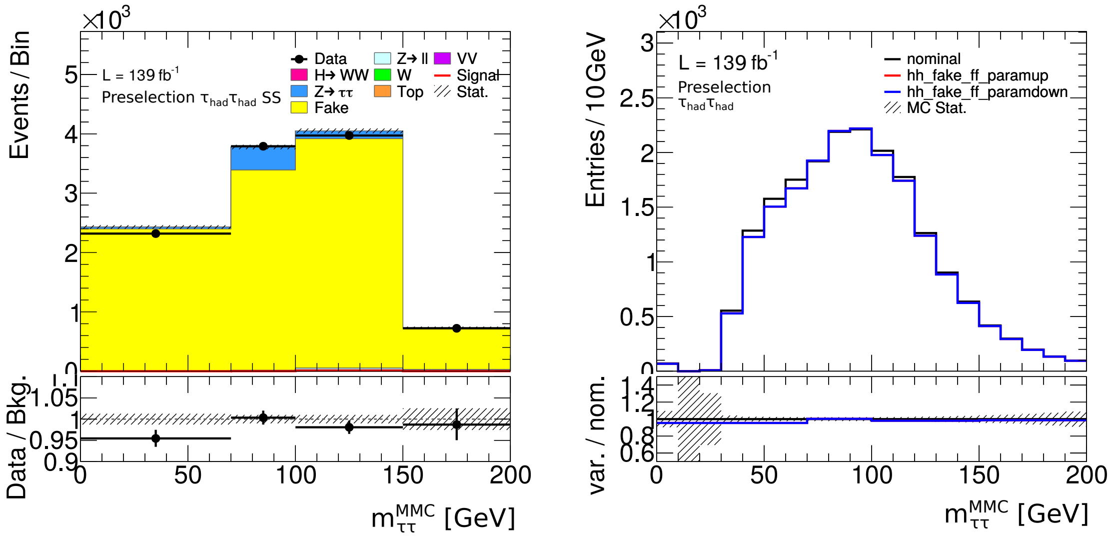

(a)

(b)

Figure 8.15: (a) Same-sign $m_{\tau\tau}^{\mathrm{MMC}}$ distribution at preselection, estimated with same-sign fake-factors in the same parametrization as the nominal ones from the $\tau_{\mathrm{lep}}\tau_{\mathrm{had}}$ W+jets CR. The values of the "Data/Bkg." ratio in the lower panel are applied as event weights to the Fake background to construct the parametrization uncertainty variation. (b) Impact of the parametrization uncertainty on the predicted MMC distribution of the Fake contribution in the SR preselection.

sign region, however, leads to a strongly reduced predicted overall yield for the Fake contribution. This shows that the effect of changing the fake-factor source region is larger than the effect of switching between the nOS and fake-factor method, which is also evidenced by Fig. 8.18, where the same-sign fake-factors were used to estimate the Fake contribution in the SR preselection. The main improvement in the lower part of the $m_{\tau\tau}^{\mathrm{MMC}}$ spectrum comes from the fake-factors being higher in the $\tau_{\mathrm{lep}}\tau_{\mathrm{had}}$ W+jets CR due to a different composition of the Fake background in that region. This difference is presumably related to the presence of processes such as $W \to qq'$ production with additional jets, where the two jets produced from the W-boson decay are more likely to be reconstructed with the same charge than jets in QCD multi-jet events. The fraction of such processes is different in the same-sign and opposite-sign selection, which changes the composition of objects faking $\tau_{\mathrm{had\text{-}vis}}$ candidates and thus the fake-factors themselves.

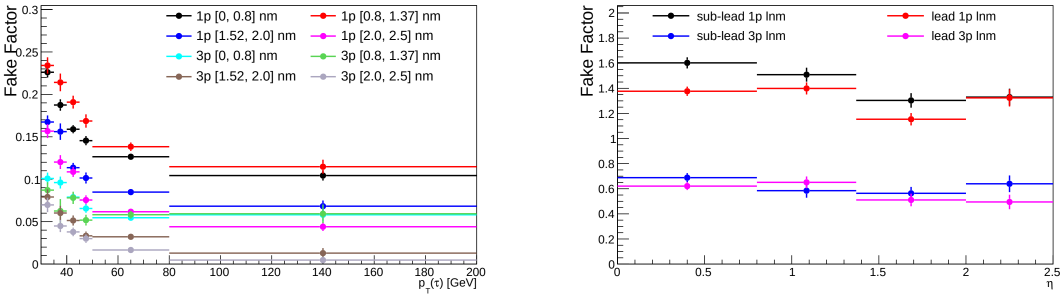

(a) Same-sign F_{nm} (b) Same-sign F_{lnm}

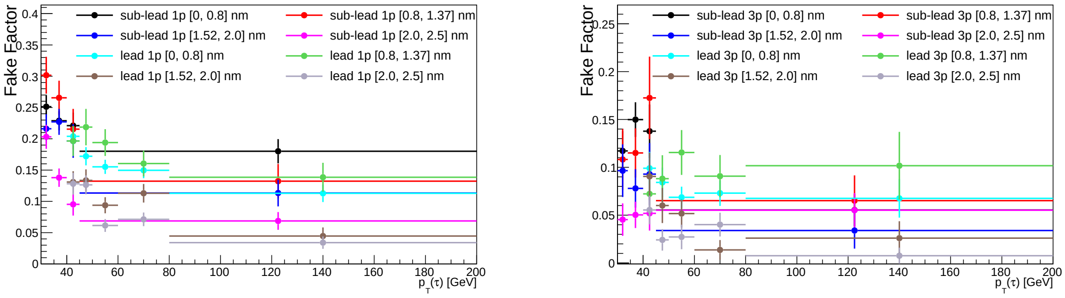

(c) High-$\Delta\eta$ F_{nm} 1p (d) High-$\Delta\eta$ F_{nm} 3p

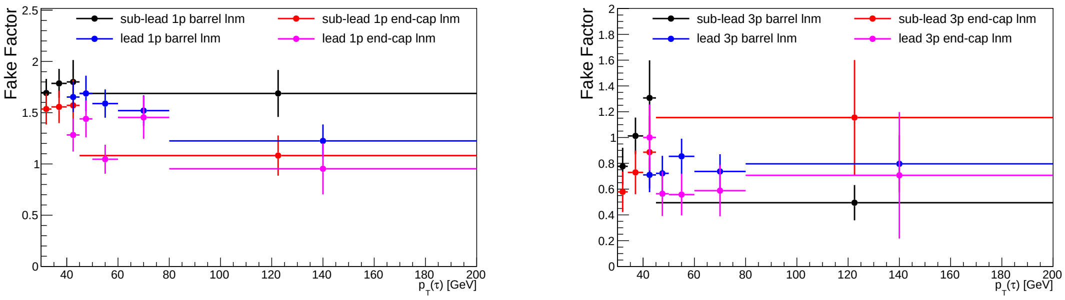

(e) High-$\Delta\eta$ F_{lnm} 1p (f) High-$\Delta\eta$ F_{lnm} 3p

Figure 8.16: Fake-factors used for evaluating the composition uncertainty, measured in the same-sign and the high-$\Delta\eta$ region at preselection. The only fake-factors with a one-dimensional parametrization are the same-sign F_{lnm} shown in (b). The legend entries for the other of fake-factors give the $|\eta|$ range in which they were measured.

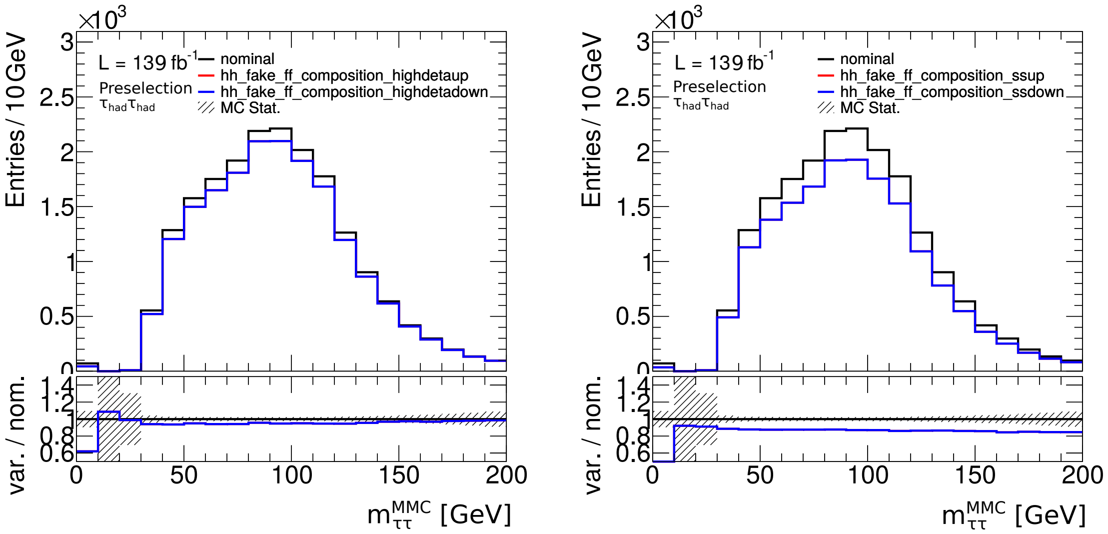

(a)

(b)

Figure 8.17: Impact of the composition uncertainty of the fake-factors on the predicted MMC distribution of the fake contribution in the SR preselection.

8.5 Analysis Outlook

The Higgs-boson production cross-section measurement in the $H \to \tau\tau$ channel based on the full Run-2 dataset follows the “Simplified Template Cross-Section” (STXS) scheme. It has been developed to provide a more detailed measurement of Higgs-boson production cross-sections while decorrelating systematic uncertainties that are most impactful in different phase-space regions. The STXS scheme entails a splitting of the $H \to \tau\tau$ signal into different production modes and phase-space regions independent of the decay channel. A splitting into nine signal categories based on the production mechanism and truth-level event features, named “STXS bins,” is planned. These STXS bins are named:

1. EWHqq, ≥ 2 jet, 60 GeV $\leq m_{jj} <$ 120 GeV
2. EWHqq, ≥ 2 jet, $m_{jj} \geq$ 350 GeV
3. ttH
4. ggF, ≥ 2 jet, $m_{jj} \geq$ 350 GeV
5. ggF, (1 jet, 60 GeV $\leq p_{\mathrm{T}}^{H} <$ 120 GeV) or (≥ 2 jet, $m_{jj} <$ 350 GeV)

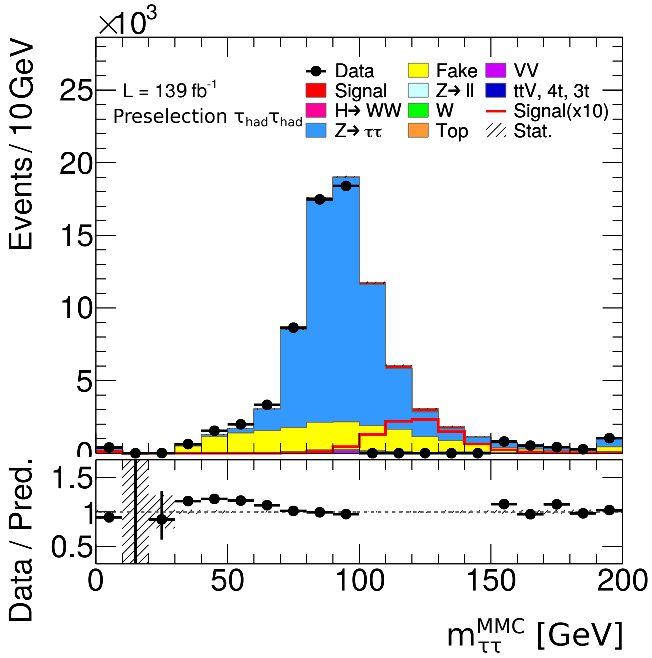

Figure 8.18: Event distribution in the SR preselection in dependence of the $m_{\tau\tau}^{\text{MMC}}$ value. The Fake contribution is estimated with the fake-factor method, using the fake-factors measured in the same-sign region shown in Fig. 8.16 (a) and (b).

6. ggF, 1 jet, 120 GeV $\leq p_{\text{T}}^{H} < 200$ GeV
7. ggF, ≥ 2 jet, 120 GeV $\leq p_{\text{T}}^{H} < 200$ GeV, $m_{jj} < 350$ GeV
8. ggF, 200 GeV $\leq p_{\text{T}}^{H} < 300$ GeV
9. ggF, $p_{\text{T}}^{H} \geq 300$ GeV .

The events in each STXS bin are assigned a free normalization factor in the likelihood fit that determines the production cross-sections. Thus, each bin represents a parameter of interest (POI) of the fit, which is measured separately from the others. Higgs-boson production events that are not covered by these STXS bins are not assigned a normalization factor, and are treated as background for this fit.

The first bin targets electroweak production of a Higgs boson in association with two quarks. Given the range of m_{jj}, which covers the masses of W and Z bosons, this bin contains mainly VH production events with hadronically-decaying vector bosons. The second bin contains mostly VBF events, since the jets produced in these often reach very high invariant masses. The ttH process is not split, since the estimated sensitivity to this process is not high. Splitting it into different subprocesses would further reduce the significance of each of them.

For the ggF process, six bins are introduced based on the number of jets that are produced in association with the Higgs boson, the p_T of the Higgs boson and the invariant mass m_{jj} of the two leading jets. This splitting is based on the STXS binning scheme for the ggF process, which is shown in Fig. 8.19.

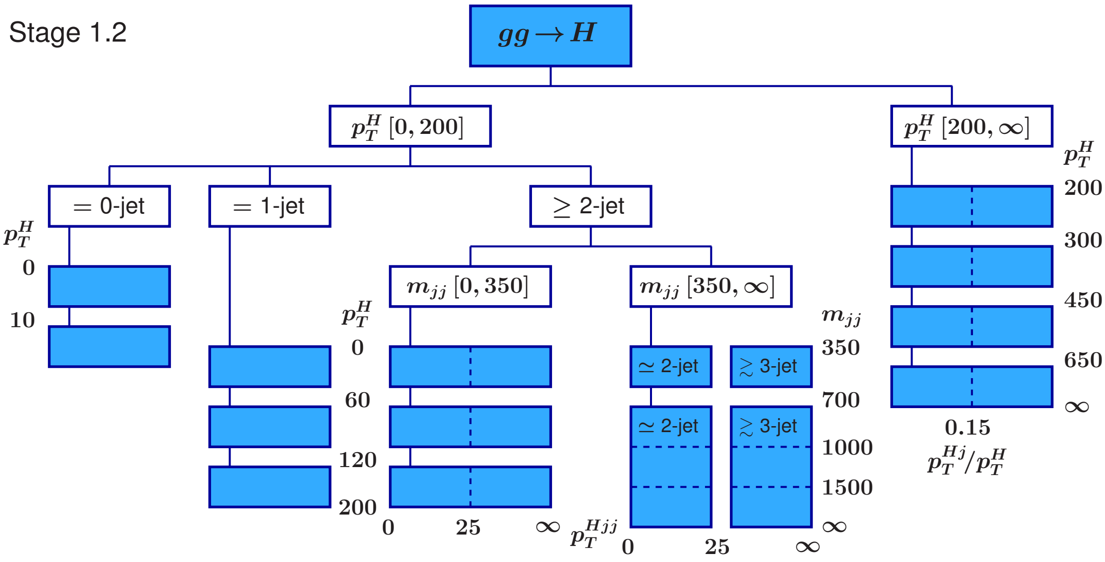

Figure 8.19: Splitting of ggF Higgs-boson production events recommended by the latest version of the STXS framework, named STXS stage 1.2. Each of the blue boxes represent a proposed truth-level split of the ggF process. The numbers around the blue boxes together with the numbers in the white boxes specify the STXS bin definitions. The dashed lines within the blue boxes represent a suggestion for a finer splitting if the sensitivity of the analysis allows for it.

While the analysis is highly sensitive to ggF, the sensitivity does not suffice to split this process into the 16 bins proposed in Fig. 8.19. Instead, bins are merged where it was found that the estimated sensitivity is too low.

To minimize the correlation between the nine POIs, the truth-level splitting must be closely matched with the reconstruction-level SR definitions. Therefore, the Boost region is split into eight SRs. To approximate the truth-level cut on p_T^H, the p_T of the combined system of the τ-lepton decay products and the $E_\mathrm{T}^\mathrm{miss}$ is used. The subregions are named Boost 0 (100 GeV $\leq p_\mathrm{T}^H <$ 120 GeV), Boost 1 (120 GeV $\leq p_\mathrm{T}^H <$ 200 GeV), Boost 2 (200 GeV $\leq p_\mathrm{T}^H <$ 300 GeV) and Boost 3 (300 GeV $\leq p_\mathrm{T}^H$). Moreover, a splitting in the jet multiplicity N_jets is conducted, to separate events with exactly one jet (1J) from events with at least two jets (ge2J). Only jets with $p_{\mathrm{T}} > 30$ GeV are taken into account. The construction of the eight $\tau_{\mathrm{had}}\tau_{\mathrm{had}}$ Boost SRs is visualized in Fig. 8.20.

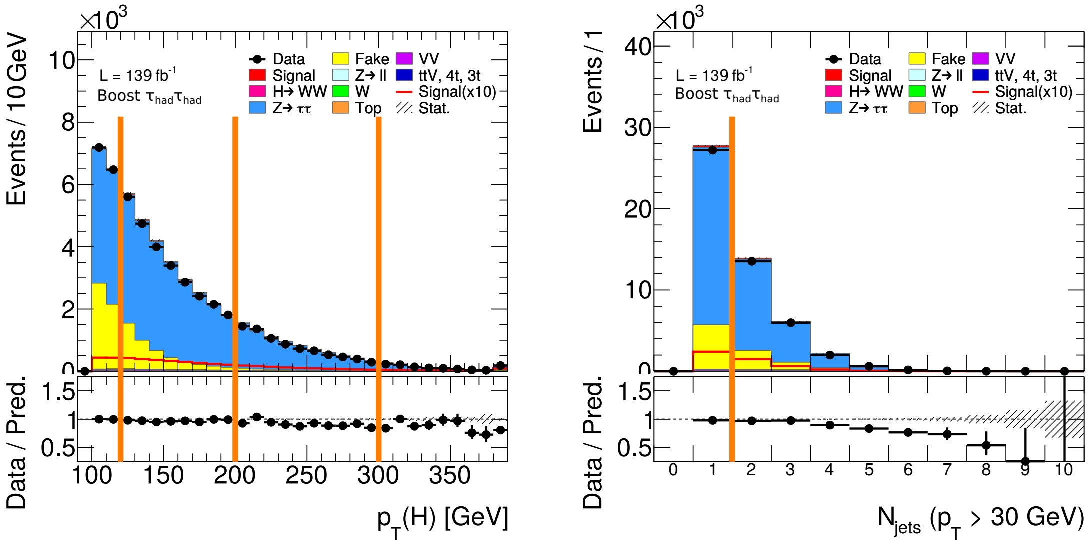

(a) (b)

Figure 8.20: Event distribution in the $\tau_{\mathrm{had}}\tau_{\mathrm{had}}$ Boost region in dependence of (a) p_{T}^{H} and (b) N_{jets}. The vertical orange lines indicate the SR splitting.

The resulting $m_{\tau\tau}^{\mathrm{MMC}}$ distributions are shown in Fig. 8.21 for the SRs with only one jet and Fig. 8.22 for those with at least two jets. The relative contribution of Fake events is very low in the regions with $p_T^H > 200$ GeV. This is due to a softer p_{T} spectrum of the jets in QCD multi-jet production events and low angular correlation between the jets. This makes it rare for a system of two jets that fake $\tau_{\mathrm{had\text{-}vis}}$ candidates and the $E_{\mathrm{T}}^{\mathrm{miss}}$ to reach such high p_{T} values.

While the signal purity in the VBF SR is very high, the total number of events is not. Moreover, the theoretical uncertainties on the VBF production cross-section are significantly lower than those on the ggF production. For these reasons, the sensitivity to the VBF cross-section is limited more strongly by statistical uncertainties than in the case of ggF. Therefore, no splitting of the VBF process into STXS bins is performed. Instead, it is treated in a similar way as the VH and ttH regions. The plan for these regions is to design BDTs in order to construct a highly sensitive subregion in each of the VBF, VH and ttH regions, following a similar event categorization strategy as the one described in Sec. 7.4 for the VBF inclusive region. The $m_{\tau\tau}^{\mathrm{MMC}}$ distributions in the ttH and VH regions are shown in Fig. 8.23, while the $m_{\tau\tau}^{\mathrm{MMC}}$ distribution in the VBF region is shown in Fig. 8.24.

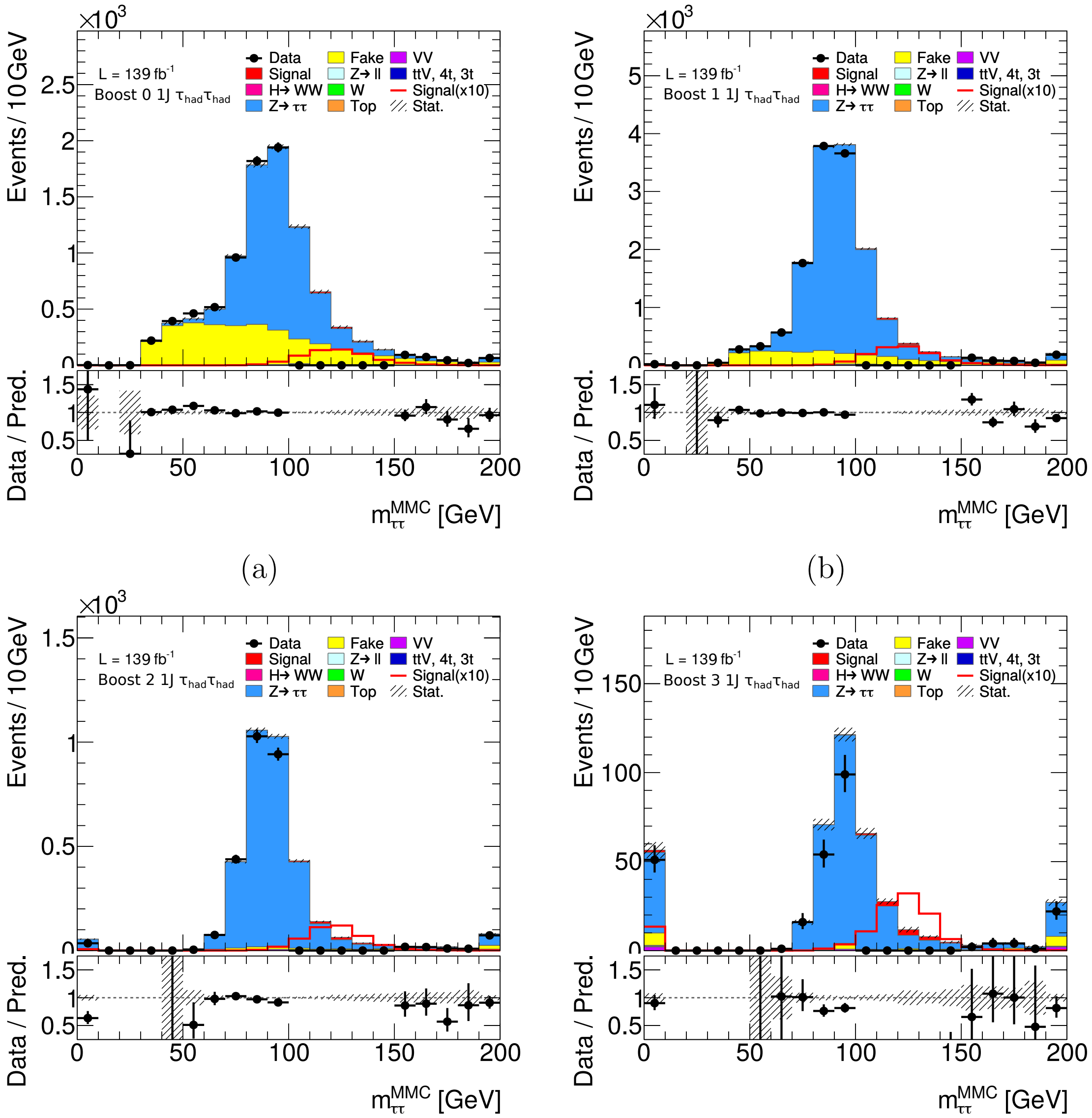

(a) (b)

(c) (d)

Figure 8.21: Event distributions in the $\tau_{\text{had}}\tau_{\text{had}}$ Boost 1J SRs in dependence of $m_{\tau\tau}^{\text{MMC}}$. The data in the range 100 GeV $< m_{\tau\tau}^{\text{MMC}} <$ 150 GeV have been blinded.

The agreement of data and prediction is good in the unblinded parts of all SRs, showing that the fake-factor method is applicable in each SR despite the fake-factors being derived inclusively at preselection.

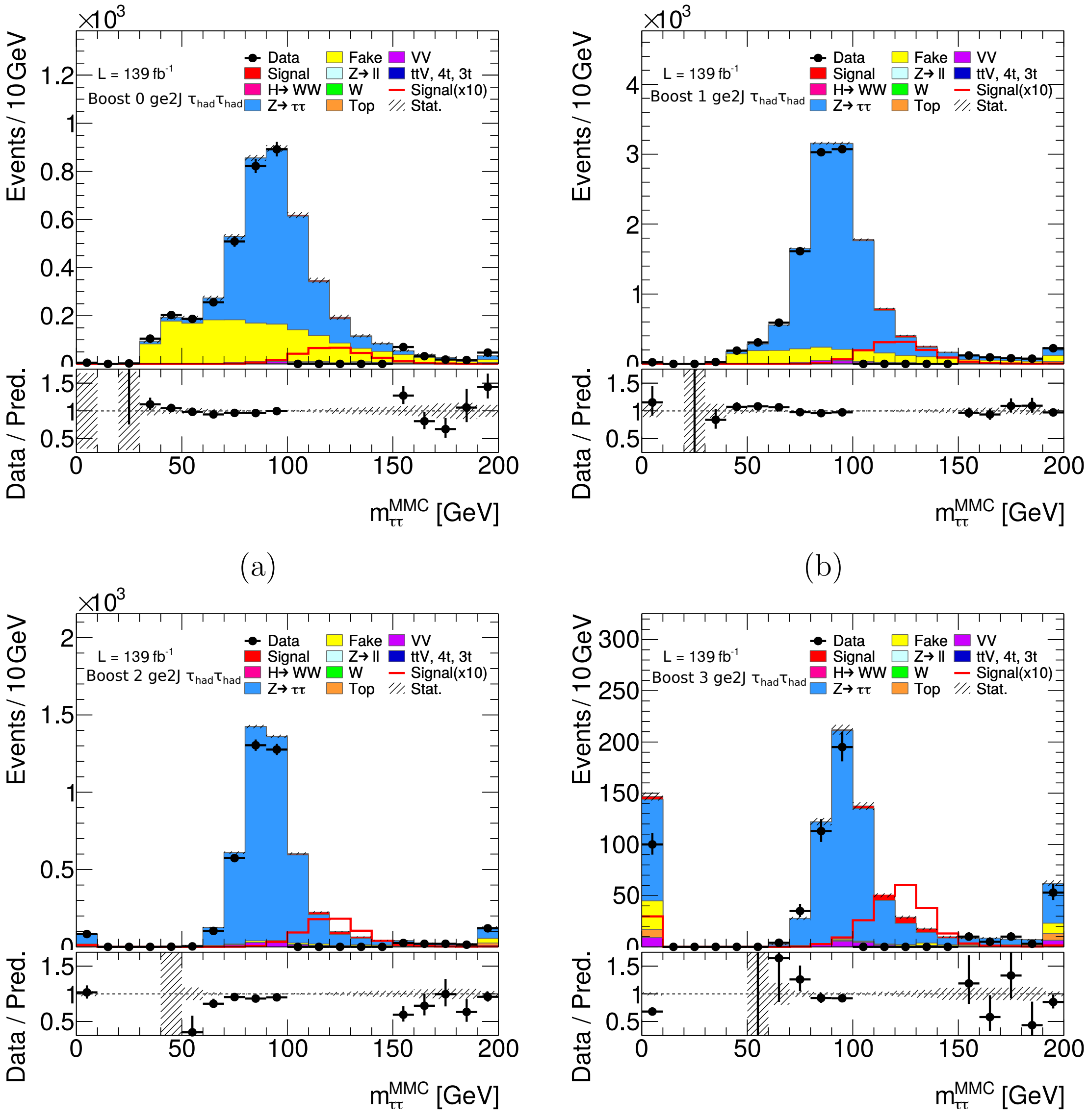

(a)

(b)

(c)

(d)

Figure 8.22: Event distributions in the $\tau_{\text{had}}\tau_{\text{had}}$ Boost ge2J SRs in dependence of $m_{\tau\tau}^{\text{MMC}}$. The data in the range 100 GeV $< m_{\tau\tau}^{\text{MMC}} <$ 150 GeV have been blinded.

After the measurement of the Higgs-boson production cross-sections is concluded, the VBF SR can be used as a baseline for a new test of CPV in HVV couplings. Since the same couplings also appear in VH events, it is possible to include the VH SR as well, although it will likely not increase the sensitivity to $\tilde{d}$

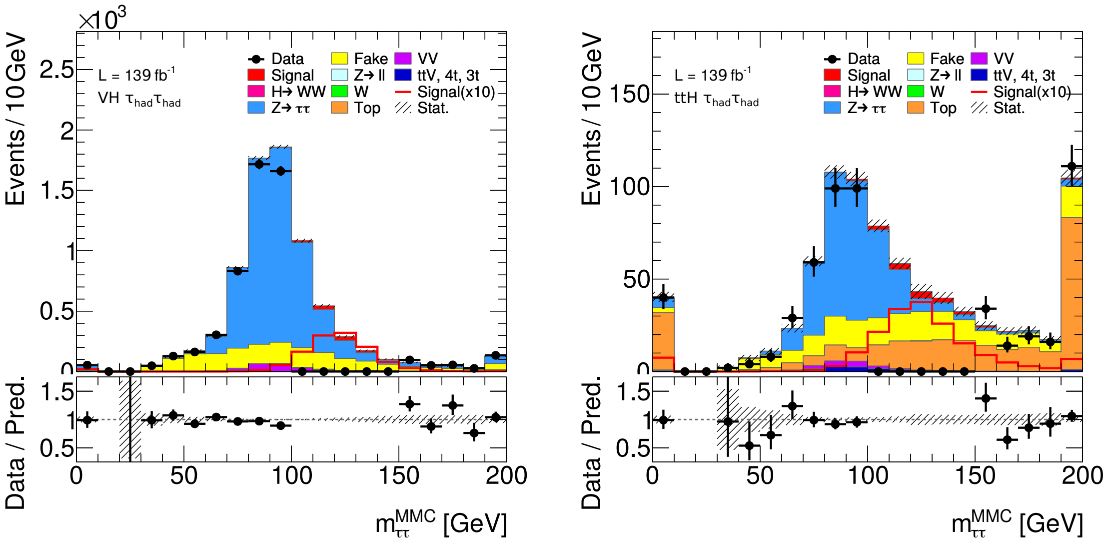

(a) (b)

Figure 8.23: Event distributions in the $\tau_{\text{had}}\tau_{\text{had}}$ (a) VH and (b) ttH SRs in dependence of $m_{\tau\tau}^{\text{MMC}}$. The data in the range 100 GeV $< m_{\tau\tau}^{\text{MMC}} <$ 150 GeV have been blinded.

in such a measurement very much.

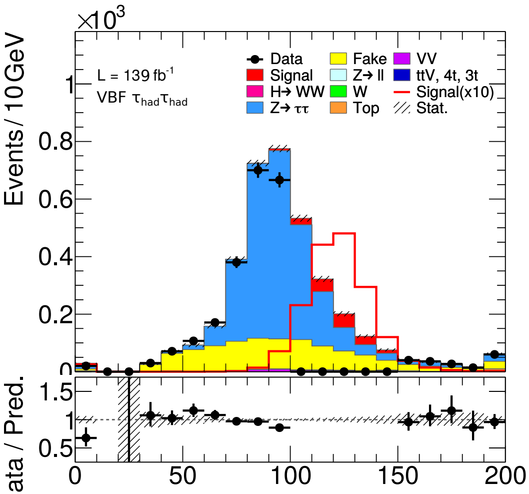

Figure 8.24: Event distributions in the $\tau_{\text{had}}\tau_{\text{had}}$ VBF SRs in dependence of $m_{\tau\tau}^{\text{MMC}}$. The data in the range 100 GeV $< m_{\tau\tau}^{\text{MMC}} <$ 150 GeV have been blinded.

CHAPTER 9

Conclusion

In this thesis, three measurements were presented, which all build upon each other. The measurement of τ-trigger efficiencies is needed to reliably predict data distributions in the $\tau_{\text{had}}\tau_{\text{had}}$ channel of $H \to \tau\tau$ events. Such events can be investigated to measure the Higgs-boson production cross-section. Once an analysis with sensitivity to Higgs-boson production events is set up, other analyses such as the presented test of CPV in VBF production can also be conducted.

The τ-lepton triggers are, among many measurements, necessary for the analysis of the fully hadronic channel of $H \to \tau\tau$ decays, when no electrons or muons are available for triggering. Therefore, identifying what leads to data loss is important for a large part of the ATLAS physics program. By developing a selection to utilize $Z \to \tau\tau$ events, the efficiencies as well as the related correction factors for simulated samples could be measured. Moreover, the main source of the mismodelling in simulation has been identified as the sum of energies in ECal and HCal deposited by a $\tau_{\text{had-vis}}$ candidate measured at L1. While the results of the efficiency measurement shown in Sec. 6.5 are final for Run 2, the analysis could be improved in the future by conducting a likelihood fit instead of the simpler subtraction of background processes to obtain the efficiencies in data, which would allow for constraining overestimated systematic uncertainties. Regarding the trigger algorithm itself, substantial improvements have been made on the L1 processing of events, which is the main limitation of the trigger chains. At the same time, the RNN-based identification is optimized to be less susceptible to pile-up effects. Therefore, despite the increase in instantaneous luminosity planned for Run 3, it can be expected that τ-lepton triggers will be able to improve in performance.

The measurement of the CP properties of HVV couplings covered in Chap. 7 can give insights on the mechanisms that led to the observed baryon asymmetry in the universe. The presented analysis used BDTs to isolate the signal process and the distribution of the Optimal Observable in VBF $H \to \tau\tau$ events was investigated to measure the parameter $\tilde{d}$ that introduces CPV in HVV couplings.

Its observed best-fit value is

$$\tilde{d} = -0.013^{+0.048}_{-0.077} ,$$

which is consistent with the SM expectation of $\tilde{d} = 0$ and CP conservation in HVV couplings. No 95% CL interval could be set on $\tilde{d}$ due to the observed signal strength $\mu = 0.73 \pm 0.47$ being lower than expected. The expected 68% CL interval on $\tilde{d}$ is $[-0.035, 0.033]$, which represents the strongest expected 68% limit from a single decay channel. The expected 95% CL interval is $\tilde{d} \in [-0.21, 0.15]$.

While the improvement with respect to the Run-1 68% CL limit [50] of $\tilde{d} \in [-0.11, 0.05]$ is sizable, the goal of setting limits on $\tilde{d}$ at 95% CL has not been reached. A new analysis including the full Run-2 dataset will likely achieve this goal. Apart from the obvious increase in available data, the new $H \to \tau\tau$ cross-section measurement, which the next VBF $H \to \tau\tau$ CP analysis could be based on, already features significant improvements to the analysis techniques. Having access to the fake-factor method for the Fake estimation will greatly benefit the $\tau_{\mathrm{had}}\tau_{\mathrm{had}}$ channel, since the limitations of the nOS method reduced its sensitivity. Due to its statistical limitations, the optimal BDT cut for the definition of the SR was loosened, lowering the signal-to-background ratio in the SR. Moreover, fluctuations of the Fake template were the main limiting factor for the algorithm that determined the SR binning, despite the loosened ID requirement. These problems should be greatly reduced with the fake-factor estimation, allowing for a better signal sensitivity and more bins in the SR for a higher sensitivity to shape variations.

The cross-section measurement also promises great improvements with respect to the latest published result documented in Ref. [120]. This is best evidenced by the increase of resolvable STXS bins from three to nine. In addition to the more accurate measurement of production cross-sections, the increased sensitivity will allow for setting stronger constraints on the τ-lepton Yukawa coupling.

The STXS analysis can serve as a baseline for several measurements of Higgs-boson properties, such as a test of CPV in HVV couplings and a complementary test of CPV in $H\tau\tau$ couplings, a test of lepton-flavour violation in Higgs-boson decays, and possibly a differential cross-section measurement in $p_{\mathrm{T}}(H)$ or a CP-odd variable. This ties in with the overall plans of the ATLAS collaboration of how to solidify our knowledge of the Higgs boson. To conclude the Run-2 studies, a combined measurement of CPV in HVV couplings using different Higgs-boson decay channels, such as $H \to \gamma\gamma$, $H \to VV$ or $H \to bb$ in addition to $H \to \tau\tau$, has been proposed. This measurement would offer new possibilities and might be able to simultaneously measure two of the three dimensions of the EFT parameter space of CP-violating HVV couplings, instead of simplifying the model to one dimension, and would bring us one step closer to an explanation of the baryon asymmetry of the universe and to understanding the full nature of the Higgs boson itself.

Acknowledgements

“Academia is not for everyone.”

Sent on my journey towards a Ph.D. with these inspiring words of encouragement, I knew I could not fail. But even with this big advantage, a Ph.D. in particle physics is not something that can be achieved alone. This section is dedicated to a small selection of the people who helped me make this thesis a reality.

My biggest thanks go to my supervisor, the voice of reason, Stan Lai, who without a doubt made the biggest contribution to my efforts to become one of “not everyone.” I’ve always appreciated your proactive and direct way of supervising students, even if this sometimes entails a bit of micro-management. And thanks as well for being able to handle a joke, even if that joke is a Master student who starts his involvement in the group by getting the day of the first meeting wrong.

And in better times, there was also Michel Janus. I really cannot imagine a better person to help a student get started in ATLAS. Always helpful, (much) more than willing to share his expertise, laid-back about everything but questions of coding style. I wish you the best for the future, and Godspeed on your side projects.

A warm thank you also to Jason Veatch for proof-reading this mess of a thesis, and for helping me find the best croissants in the world. Many thanks to Timo (who still owes me a euro) and Kira (who has been in group Lai for almost as long as me), for covering up my lack of professionalism on many occasions. But unfortunately not while writing these acknowledgements.

To Lino and Petar, probably the most cultured individuals I had the honour to work with: thancc.

I also want to thank my “second working group” in Freiburg, especially Markus Schumacher, for being an expert at seemingly everything. Many thanks to Kathrin

and Alena, for showing me week after week what can be accomplished with the right mindset. Bug catcher Dirk and code critic David, thanks for all your help. Special thanks to Benjamin for letting me borrow his smoothie blender, and to Katharina and Fabian for sharing my pain. Big thanks to Bertrand for making performance work interesting. My thanks also go to the non-Freiburg part of the VBF CP team: to Christian for always being available during HAPPy little emergencies, and to the omnipresent Alessia Murrone.

I am also grateful for the support from the $H \to \tau\tau$ team. Thanks to Eric for helping me get started, to Antonio for never sleeping, and to Quentin and PO for keeping the bigger picture in mind.

Ji dê û bavê min re, spas ji bo her tiştî. Û kû ûn hîn jî bixwazin zanibin min bi salan çi kir, min li vir ji we re nivîsand.

Bibliography

[1] ATLAS Collaboration, *Observation of a new particle in the search for the Standard Model Higgs boson with the ATLAS detector at the LHC*, Phys. Lett. B **716** (2012) 1–29.

[2] CMS Collaboration, *Observation of a new boson at a mass of 125 GeV with the CMS experiment at the LHC*, Phys. Lett. B **716** (2012) 30.

[3] P. Huet and E. Sather, *Electroweak baryogenesis and standard model CP violation*, Phys. Rev. D **51** (1995) 379.

[4] M. B. Gavela, P. Hernandez, J. Orloff, and O. Pene, *Standard Model CP-violation and Baryon asymmetry*, Mod. Phys. Lett. A **9** (1994) 795–810.

[5] A. G. Cohen, D. B. Kaplan, and A. E. Nelson, *Progress in Electroweak Baryogenesis*, Ann. Rev. Nucl. Part. Sci. **43** (1993) 795–810.

[6] A. Riotto and M. Trodden, *Recent Progress in Baryogenesis*, Ann. Rev. Nucl. Part. Sci. **49** (1999) 35–75.

[7] W.-S. Hou, *Source of CP Violation for the Baryon Asymmetry of the Universe*, Chin. J. Phys. **47** (2009) 134.

[8] A. D. Sakharov, *Violation of CP invariance, C asymmetry, and baryon asymmetry of the universe*, Pisma Zh. Eksp. Teor. Fiz. **5** (1967) 32–35.

[9] N. Cabibbo, *Unitary Symmetry and Leptonic Decays*, Phys. Rev. Lett. **10** (1963) 531–533.

[10] M. Kobayashi and T. Maskawa, *CP-Violation in the Renormalizable Theory of Weak Interaction*, Prog. Theor. Phys. **49** (1973) 652–657.

[11] ATLAS Collaboration, *Test of CP invariance in vector-boson fusion production of the Higgs boson in the $H \rightarrow \tau\tau$ channel in proton–proton collisions at $\sqrt{s} = 13$ TeV with the ATLAS detector*, Phys. Lett. B **805** (2020) 135426.

[12] S. Glashow, *Partial Symmetries of Weak Interactions*, Nucl. Phys. **22** (1961) 579.

[13] A. Salam, *Weak and Electromagnetic Interactions*, Nobel Symposium **8** (1968) 367–377.

[14] S. Weinberg, *A model of Leptons*, Phys. Rev. Lett. **19** (1967) 1264.

[15] UA2 Collaboration, *Observation of single isolated electrons of high transverse momentum in events with missing transverse energy at the CERN $\bar{p}p$ Collider*, Phys. Lett. B **122** (1983) 476–485.

[16] UA1 Collaboration, *Experimental observation of isolated large transverse energy electrons with associated missing energy at $\sqrt{s} = 540$ GeV*, Phys. Lett. B **122** (1983) 103–116.

[17] UA2 Collaboration, *Evidence for $Z^0 \rightarrow e^+e^-$ at the CERN $\bar{p}p$ Collider*, Phys. Lett. B **129** (1983) 130–140.

[18] UA1 Collaboration, *Experimental observation of lepton pairs of invariant mass around 95 GeV/c^2 at the CERN SPS collider*, Phys. Lett. B **126** (1983) 398–410.

[19] G. S. Guralnik, C. R. Hagen, and T. W. B. Kibble, *Global Conservation Laws and Massless Particles*, Phys. Rev. Lett. **13** (1964) 585–587.

[20] F. Englert and R. Brout, *Broken Symmetry and the Mass of Gauge Vector Mesons*, Phys. Rev. Lett. **13** (1964) 321–323.

[21] P. W. Higgs, *Broken Symmetries and the Masses of Gauge Bosons*, Phys. Rev. Lett. **13** (1964) 508–509.

[22] Particle Data Group, *Review of Particle Physics*, Prog. Theor. Exp. Phys. **083C01** (2020) 1–2092.

[23] D. de Florian et al., *Handbook of LHC Higgs Cross Sections: 4. Deciphering the Nature of the Higgs Sector*, CERN–2017–002-M, 2017, `https://cds.cern.ch/record/2227475`.

[24] A. Djouadi, J. Kalinowski, and M. Spira, *HDECAY: A Program for Higgs boson decays in the standard model and its supersymmetric extension*, Comput. Phys. Commun. **108** (1998) 56–74.

[25] A. Bredenstein, A. Denner, S. Dittmaier, A. Mück, and M. M. Weber, *Prophecy4f: A Monte Carlo generator for a proper description of the Higgs decay into 4 fermions*, `http://prophecy4f.hepforge.org/`.

[26] C. Anastasiou et al., *Higgs boson gluon-fusion production at threshold in* N^3LO *QCD*, Phys. Lett. B **737** (2014) 325.

[27] C. Anastasiou et al., *Higgs boson gluon-fusion production beyond threshold in* N^3LO *QCD*, JHEP **03** (2015) 091.

[28] C. Anastasiou, C. Duhr, F. Dulat, E. Furlan, and T. Gehrmann, *Higgs Boson Gluon-Fusion Production in QCD at Three Loops*, Phys. Rev. Lett. **114** (2015) 212001.

[29] U. Aglietti, R. Bonciani, G. Degrassi, and A. Vicini, *Two loop light fermion contribution to Higgs production and decays*, Phys. Lett. B **595** (2004) 432–441.

[30] S. Actis, G. Passarino, C. Sturm, and S. Uccirati, *NLO Electroweak Corrections to Higgs Boson Production at Hadron Colliders*, Phys. Lett. B **670** (2008) 12–17.

[31] S. Actis, G. Passarino, C. Sturm, and S. Uccirati, *NNLO Computational Techniques: The Cases* $H \to \gamma\gamma$ *and* $H \to gg$, Nucl. Phys. B **811** (2009) 182–273.

[32] M. Cacciari, F. A. Dreyer, A. Karlberg, G. P. Salam, and G. Zanderighi, *Fully Differential Vector-Boson-Fusion Higgs Production at Next-to-Next-to-Leading Order*, Phys. Rev. Lett. **115** (2015) 082002.

[33] A. Denner, S. Dittmaier, S. Kallweit, and A. Mück, *HAWK 2.0: A Monte Carlo program for Higgs production in vector-boson fusion and Higgs strahlung at hadron colliders*, Comput. Phys. Commun. **195** (2015) 161–171.

[34] M. Ciccolini, A. Denner, and S. Dittmaier, *Strong and electroweak corrections to the production of Higgs + 2jets via weak interactions at the LHC*, Phys. Rev. Lett. **99** (2007) 161803.

[35] M. Ciccolini, A. Denner, and S. Dittmaier, *Electroweak and QCD corrections to Higgs production via vector-boson fusion at the LHC*, Phys. Rev. D **77** (2008) 013002.

[36] P. Bolzoni, F. Maltoni, S.-O. Moch, and M. Zaro, *Higgs production via vector-boson fusion at NNLO in QCD*, Phys. Rev. Lett. **105** (2010) 011801.

[37] M. Ciccolini, S. Dittmaier, and M. Krmer, *Electroweak radiative corrections to associated WH and ZH production at hadron colliders*, Phys. Rev. D **68** (2003) 073003.

[38] O. Brein, R. V. Harlander, and T. J. E. Zirke, *vh@nnlo - Higgs Strahlung at hadron colliders*, Comput. Phys. Commun. **184** (2013) 998–1003.

[39] R. V. Harlander, S. Liebler, and T. J. E. Zirke, *Higgs Strahlung at the Large Hadron Collider in the 2-Higgs-Doublet Model*, JHEP **02** (2014) 023.

[40] O. Brein, A. Djouadi, and R. V. Harlander, *NNLO QCD corrections to the Higgs-strahlung processes at hadron colliders*, Phys. Lett. B **579** (2004) 149–156.

[41] W. Beenakker, et al., *Higgs radiation off top quarks at the Tevatron and the LHC*, Phys. Rev. Lett. **87** (2001) 201805.

[42] W. Beenakker, et al., *NLO QCD corrections to $t\bar{t}H$ production in hadron collisions*, Nucl. Phys. B **653** (2003) 151–203.

[43] S. Dawson, L. H. Orr, L. Reina, and D. Wackeroth, *Associated top quark Higgs boson production at the LHC*, Phys. Rev. D **67** (2003) 071503.

[44] S. Dawson, C. Jackson, L. H. Orr, L. Reina, and D. Wackeroth, *Associated Higgs production with top quarks at the large hadron collider: NLO QCD corrections*, Phys. Rev. D **68** (2003) 034022.

[45] Y. Zhang, W.-G. Ma, R.-Y. Zhang, C. Chen, and L. Guo, *QCD NLO and EW NLO corrections to ttH production with top quark decays at hadron collider*, Phys. Lett. B **738** (2014) 1–5.

[46] S. Frixione, V. Hirschi, D. Pagani, H. S. Shao, and M. Zaro, *Electroweak and QCD corrections to top-pair hadroproduction in association with heavy bosons*, JHEP **06** (2015) 184.

[47] L. Landau, *On the angular momentum of a system of two photons*, Dokl. Akad. Nauk. SSSR **60** (1948) 471–473.

[48] C.-N. Yang, *Selection Rules for the Dematerialization of a Particle into Two Photons*, Phys. Rev. **77** (1950) 242.

[49] ATLAS Collaboration, *Study of the spin and parity of the Higgs boson in diboson decays with the ATLAS detector*, Eur. Phys. J. C **75** (2015) 476.

[50] ATLAS Collaboration, *Test of CP Invariance in vector-boson fusion production of the Higgs boson using the Optimal Observable method in the ditau decay channel with the ATLAS detector*, Eur. Phys. J. C **76** (2016) 658.

[51] C. D. Anderson, *The Apparent Existence of Easily Deflectable Positives*, Science **76** (1932) 238–239.

[52] P. A. M. Dirac, *The quantum theory of the electron*, Proceedings of the Royal Society A **117** (1928) 778.

[53] J. H. Christenson, J. W. Cronin, V. L. Fitch, and R. Turlay, *Evidence for the 2π Decay of the K_2^0 Meson*, Phys. Rev. Lett. **13** (1964) 138.

[54] L. Wolfenstein, *Parametrization of the Kobayashi-Maskawa Matrix*, Phys. Rev. Lett. **51** (1983) 1945–1947.

[55] WMAP Collaboration, *First-Year Wilkinson Microwave Anisotropy Probe (WMAP) Observations: Preliminary Maps and Basic Results*, Astrophys. J. Suppl. **148** (2003) 97.

[56] W. Buchmuller and D. Wyler, *Effective Lagrangian Analysis of New Interactions and Flavor Conservation*, Nucl. Phys. B **268** (1986) 621–653.

[57] V. Hankele, G. Klamke, D. Zeppenfeld, and T. Figy, *Anomalous Higgs boson couplings in vector boson fusion at the CERN LHC*, Phys. Rev. D **74** (2006) 095001.

[58] L3 Collaboration, *Search for anomalous couplings in the Higgs sector at LEP*, Phys. Lett. B **589** (2004) 89–102.

[59] OPAL Collaboration, *Measurement of charged current triple gauge boson couplings using W pairs at LEP*, Eur. Phys. J. C **33** (2004) 463–476.

[60] D. Atwood and A. Soni, *Analysis for magnetic moment and electric dipole moment form-factors of the top quark via $e^+e^- \to t\bar{t}$*, Phys. Rev. D **45** (1992) 2405–2413.

[61] M. Davier, L. Duflot, F. Le Diberder, and A. Rouge, *The Optimal method for the measurement of tau polarization*, Phys. Lett. B **306** (1993) 411–417.

[62] M. Diehl and O. Nachtmann, *Optimal observables for the measurement of three gauge boson couplings in $e^+e^- \to W^+W^-$*, Z. Phys. C **62** (1994) 397–412.

[63] M. Diehl, O. Nachtmann, and F. Nagel, *Triple gauge couplings in polarized $e^+e^- \to W^+W^-$ and their measurement using optimal observables*, Eur. Phys. J. C **27** (2003) 375–397.

[64] A. Elagin, P. Murat, A. Pranko, and A. Safonov, *A new mass reconstruction technique for resonances decaying to di-tau*, Nucl. Instrum. Meth. A **654** (2011) 481.

[65] H.-L. Lai et al., *New parton distributions for collider physics*, Phys. Rev. D **82** (2010) 074024.

[66] J. Alwall et al., *The automated computation of tree-level and next-to-leading order differential cross sections, and their matching to parton shower simulations*, JHEP **07** (2014) 079.

[67] J. Brehmer, F. Kling, T. Plehn, and T. M. P. Tait, *Better Higgs-CP Tests Through Information Geometry*, Phys. Rev. D **97** (2018) 095017.

[68] D. Atwood, S. Bar-Shalom, G. Eilam, and A. Soni, *CP Violation in Top Physics*, Phys. Rept **347** (2001) 1–222.

[69] L. R. Evans and P. Bryant, *LHC Machine*, JINST **3** (2008) S08001.

[70] ATLAS Collaboration, *The ATLAS Experiment at the CERN Large Hadron Collider*, JINST **3** (2008) S08003.

[71] ATLAS Collaboration, *ATLAS Luminosity Public Results*, 2019. `https://twiki.cern.ch/twiki/bin/view/AtlasPublic/LuminosityPublicResultsRun2`.

[72] ATLAS Collaboration, *ATLAS inner detector : Technical Design Report, 1*, tech. rep., 1997. ATLAS-TDR-4.

[73] ATLAS Collaboration, *ATLAS liquid-argon calorimeter : Technical Design Report*, tech. rep., 1996. ATLAS-TDR-2.

[74] ATLAS Collaboration, *ATLAS tile calorimeter : Technical Design Report*, tech. rep., 1996. ATLAS-TDR-3.

[75] B. Dolgoshein, *Transition radiation detectors*, Nucl. Instrum. Meth. A **326** (1993) 434–469.

[76] ATLAS Collaboration, *2015 start-up trigger menu and initial performance assessment of the ATLAS trigger using Run-2 data*, ATL-DAQ-PUB-2016-001, 2016, `https://cds.cern.ch/record/2136007`.

[77] NNPDF Collaboration, *Parton distributions from high-precision collider data*, CERN-TH-2017-077, 2017, `https://arxiv.org/abs/1706.00428`.

[78] J. C. Collins, D. E. Soper, and G. Sterman, *Factorization of Hard Processes in QCD*, Adv.Ser.Direct.High Energy Phys. **5** (1989) 1–91.

[79] A. Buckley et al., *General-purpose event generators for LHC physics*, Phys. Rep. **504** (2011) 145–233.

[80] T. Gleisberg et al., *Event generation with SHERPA 1.1*, JHEP **0902** (2009) 007.

[81] ATLAS Collaboration, *The ATLAS Simulation Infrastructure*, Eur. Phys. J. C **70** (2010) 823–874.

[82] GEANT4 Collaboration, *GEANT4 – a simulation toolkit*, Nucl. Instrum. Meth. A **506** (2002) 250–303.

[83] ATLAS Collaboration, *Early Inner Detector Tracking Performance in the 2015 data at $\sqrt{s} = 13\ TeV$*, ATL-PHYS-PUB-2015-051, 2015, `https://cds.cern.ch/record/2110140`.

[84] ATLAS Collaboration, *Vertex Reconstruction Performance of the ATLAS Detector at $\sqrt{s} = 13\ TeV$*, ATL-PHYS-PUB-2015-026, 2015, `https://cds.cern.ch/record/2037717`.

[85] ATLAS Collaboration, *Topological cell clustering in the ATLAS calorimeters and its performance in LHC Run 1*, Eur. Phys. J. C **77** (2017) 490.

[86] ATLAS Collaboration, *Electron reconstruction and identification in the ATLAS experiment using the 2015 and 2016 LHC proton-proton collision data at $\sqrt{s} = 13\ TeV$*, Eur. Phys. J. C **79** (2019) 639.

[87] ATLAS Collaboration, *Measurement of the photon identification efficiencies with the ATLAS detector using LHC Run 2 data collected in 2015 and 2016*, Eur. Phys. J. C **79** (2019) 205.

[88] ATLAS Collaboration, *Muon reconstruction performance of the ATLAS detector in proton–proton collision data at* $\sqrt{s} = 13$ *TeV*, Eur. Phys. J. C **76** (2016) 292.

[89] T. Cornelissen et al., *The global* χ^2 *track fitter in ATLAS*, J. Phys. Conf. Ser. **119** (2008) 032013.

[90] M. Cacciari, G. P. Salam, and G. Soyez, *The anti-*k_t *jet clustering algorithm*, JHEP **04** (2008) 063.

[91] M. Cacciari and G. P. Salam, *Dispelling the* N^3 *myth for the* k_t *jet-finder*, Phys. Lett. B **641** (2006) 57–61.

[92] ATLAS Collaboration, *Jet energy scale measurements and their systematic uncertainties in proton-proton collisions at* $\sqrt{s} = 13$ *TeV with the ATLAS detector*, Phys. Rev. D **96** (2017) 072002.

[93] ATLAS Collaboration, *Performance of pile-up mitigation techniques for jets in pp collisions at* $\sqrt{s} = 8$ *TeV using the ATLAS detector*, Eur. Phys. J. C **76** (2016) 581.

[94] ATLAS Collaboration, *Identification and rejection of pile-up jets at high pseudorapidity with the ATLAS detector*, Eur. Phys. J. C **77** (2017) 580.

[95] ATLAS Collaboration, *Performance of b-Jet Identification in the ATLAS Experiment*, JINST **11** (2016) P04008.

[96] ATLAS Collaboration, *Search for new resonances in mass distributions of jet pairs using 139* fb^{-1} *of pp collisions at* $\sqrt{s} = 13$ *TeV with the ATLAS detector*, JHEP **03** (2020) 145.

[97] ATLAS Collaboration, *Measurement of the tau lepton reconstruction and identification performance in the ATLAS experiment using pp collisions at* $\sqrt{s} = 13$ *TeV*, ATLAS-CONF-2017-029, 2017, `https://cds.cern.ch/record/2261772`.

[98] T. Barillari et al., *Local Hadronic Calibration*, ATL-LARG-PUB-2009-001-2, 2008, `https://cds.cern.ch/record/1112035`.

[99] ATLAS Collaboration, *Reconstruction, Energy Calibration, and Identification of Hadronically Decaying Tau Leptons in the ATLAS Experiment for Run-2 of the LHC*, ATL-PHYS-PUB-2015-045, 2015, `https://cds.cern.ch/record/2064383`.

[100] ATLAS Collaboration, *Identification of hadronic tau lepton decays using neural networks in the ATLAS experiment*, ATL-PHYS-PUB-2019-033, 2019, `http://cds.cern.ch/record/2688062`.

[101] ATLAS Collaboration, *Performance of missing transverse momentum reconstruction with the ATLAS detector using proton-proton collisions at $\sqrt{s} = 13$ TeV*, Eur. Phys. J. C **78** (2018) 903.

[102] ATLAS Collaboration, *The ATLAS Tau Trigger in Run 2*, ATLAS-CONF-2017-061, 2017, `https://cds.cern.ch/record/2274201`.

[103] ATLAS Collaboration, *Performance of the ATLAS Trigger System in 2010*, Eur. Phys. J. C **72** (2012) 1849.

[104] R. Chierici and A. Valassi, *Information and treatment of unknown correlations in the combination of measurements using the BLUE method*, Eur. Phys. J. C **74** (2014) 2717.

[105] P. Nason, *A New Method for Combining NLO QCD with Shower Monte Carlo Algorithms*, JHEP **11** (2004) 040.

[106] S. Frixione, P. Nason, and C. Oleari, *Matching NLO QCD computations with Parton Shower simulations: the POWHEG method*, JHEP **11** (2007) 070.

[107] S. Alioli, P. Nason, C. Oleari, and E. Re, *A general framework for implementing NLO calculations in shower Monte Carlo programs: the POWHEG BOX*, JHEP **06** (2010) 043.

[108] S. Alioli, P. Nason, C. Oleari, and E. Re, *NLO vector-boson production matched with shower in POWHEG*, JHEP **07** (2008) 060.

[109] T. Sjöstrand, S. Mrenna, and P. Skands, *A Brief Introduction to PYTHIA 8.1*, Comput. Phys. Commun. **178** (2008) 852–867.

[110] J. Pumplin et al., *New Generation of Parton Distributions with Uncertainties from Global QCD Analysis*, JHEP **07** (2002) 012.

[111] ATLAS Collaboration, *Measurement of the Z/γ^* boson transverse momentum distribution in pp collisions at $\sqrt{s} = 7$ TeV with the ATLAS detector*, JHEP **09** (2014) 145.

[112] S. Frixione, P. Nason, and G. Ridolfi, *A Positive-Weight Next-to-Leading-Order Monte Carlo for Heavy Flavour Hadroproduction*, JHEP **09** (2007) 126.

[113] T. Sjöstrand et al., *An Introduction to PYTHIA 8.2*, Comput. Phys. Commun. **191** (2015) 159–177.

[114] NNPDF Collaboration, *Parton distributions for the LHC Run II*, JHEP **04** (2015) 040.

[115] R. D. Ball et al., *Parton distributions with LHC data*, Nucl. Phys. B **867** (2012) 244–289.

[116] ATLAS Collaboration, *ATLAS Pythia 8 tunes to 7 TeV datas*, ATL-PHYS-PUB-2014-021, 2014, `https://cds.cern.ch/record/1966419`.

[117] D. J. Lange, *The EvtGen particle decay simulation package*, Nucl. Instrum. Meth. A **462** (2001) 152–155.

[118] ATLAS Collaboration, *Performance of the ATLAS muon triggers in Run 2*, JINST **15** (2020) P09015.

[119] ATLAS Collaboration, *Jet energy scale and resolution measured in proton-proton collisions at s=13 TeV with the ATLAS detector*, Submitted to Eur. Phys. J. C, 2020, `https://arxiv.org/abs/2007.02645`.

[120] ATLAS Collaboration, *Cross-section measurements of the Higgs boson decaying into a pair of tau-leptons in proton-proton collisions at* $\sqrt{s} = 13$ *TeV with the ATLAS detector*, Phys. Rev. D **99** (2019) 072001.

[121] K. Hamilton, P. Nason, E. Re, and G. Zanderighi, *NNLOPS simulation of Higgs boson production*, JHEP **10** (2013) 222.

[122] K. Hamilton, P. Nason, and G. Zanderighi, *Finite quark-mass effects in the NNLOPS POWHEG+MiNLO Higgs generator*, JHEP **05** (2015) 140.

[123] K. Hamilton, P. Nason, and G. Zanderighi, *MINLO: Multi-Scale Improved NLO*, JHEP **10** (2012) 155.

[124] J. M. Campbell et al., *NLO Higgs Boson Production Plus One and Two Jets Using the POWHEG BOX, MadGraph4 and MCFM*, JHEP **07** (2012) 092.

[125] K. Hamilton, P. Nason, C. Oleari, and G. Zanderighi, *Merging H/W/Z + 0 and 1 jet at NLO with no merging scale: a path to parton shower + NNLO matching*, JHEP **05** (2013) 082.

[126] S. Catani and M. Grazzini, *An NNLO subtraction formalism in hadron collisions and its application to Higgs boson production at the LHC*, Phys. Rev. Lett. **98** (2007) 222002.

[127] J. Butterworth et al., *PDF4LHC recommendations for LHC Run II*, J. Phys. G **43** (2016) 023001.

[128] P. Nason and C. Oleari, *NLO Higgs boson production via vector-boson fusion matched with shower in POWHEG*, JHEP **02** (2010) 037.

[129] M. Bahr et al., *Herwig++ Physics and Manual*, Eur. Phys. J. C **58** (2008) 639–707.

[130] J. Bellm et al., *Herwig 7.0/Herwig++ 3.0 release note*, Eur. Phys. J. C **76** (2016) 196.

[131] E. Bothmann et al., *Event Generation with Sherpa 2.2*, SciPost Phys. **7** (2019) 034.

[132] T. Gleisberg and S. Höche, *Comix, a new matrix element generator*, JHEP **12** (2008) 039.

[133] F. Buccioni et al., *OpenLoops 2*, Eur. Phys. J. C **79** (2019) 866.

[134] F. Cascioli, P. Maierhöfer, and S. Pozzorini, *Scattering Amplitudes with Open Loops*, Phys. Rev. Lett. **108** (2012) 111601.

[135] A. Denner, S. Dittmaier, and L. Hofer, *Collier: A fortran-based complex one-loop library in extended regularizations*, Comput. Phys. Commun. **212** (2017) 220.

[136] S. Schumann and F. Krauss, *A parton shower algorithm based on CataniSeymour dipole factorisation*, JHEP **03** (2008) 028.

[137] S. Höche, F. Krauss, M. Schönherr, and F. Siegert, *A critical appraisal of NLO+PS matching methods*, JHEP **09** (2012) 049.

[138] S. Catani, F. Krauss, R. Kuhn, and B. R. Webber, *QCD matrix elements + parton showers*, JHEP **11** (2001) 063.

[139] S. Höche, F. Krauss, M. Schönherr, and F. Siegert, *QCD matrix elements + parton showers. The NLO case*, JHEP **04** (2013) 027.

[140] S. Höche, F. Krauss, S. Schumann, and F. Siegert, *QCD matrix elements and truncated showers*, JHEP **05** (2009) 053.

[141] C. Anastasiou, L. J. Dixon, K. Melnikov, and F. Petriello, *High precision QCD at hadron colliders: Electroweak gauge boson rapidity distributions at NNLO*, Phys. Rev. D **69** (2004) 094008.

[142] ATLAS Collaboration, *Measurement of the cross-section for electroweak production of dijets in association with a Z boson in pp collisions at* $\sqrt{s} = 13$ *TeV with the ATLAS detector*, Phys. Lett. B **775** (2017) 206.

[143] T. Sjöstrand, S. Mrenna, and P. Skands, *PYTHIA 6.4 Physics and Manual*, JHEP **05** (2006) 026.

[144] P. Skands, *Tuning Monte Carlo Generators: The Perugia Tunes*, Phys. Rev. D **82** (2010) 074018.

[145] M. Czakon and A. Mitov, *Top++: a program for the calculation of the top-pair cross-section at hadron colliders*, Comput. Phys. Commun. **185** (2014) 2930.

[146] D. Kirkby and W. Verkerke, *The RooFit toolkit for data modeling*, Proceedings of CHEP03, 2003, `https://arxiv.org/abs/physics/0306116`.

[147] E. Drechsler, *Measurement of the* $H \to \tau\tau$ *Production Cross-Section in Hadronic Final States in 13 TeV Proton-Proton Collisions with the ATLAS Detector*, II.Physik-UniG-Diss-2018/02, 2018, `https://ediss.uni-goettingen.de/handle/11858/00-1735-0000-002E-E54A-6`.

[148] A. Höcker et al., *TMVA - Toolkit for Multivariate Data Analysis with ROOT*, CERN-OPEN-2007-007, 2007, `https://cds.cern.ch/record/1019880`.

[149] S. Heinemeyer et al., *Handbook of LHC Higgs Cross Sections: 3. Higgs Properties*, CERN-2013-004, 2013, `https://cds.cern.ch/record/1559921`.

[150] G. Cowan, K. Cranmer, E. Gross, and O. Vitells, *Asymptotic formulae for likelihood-based tests of new physics*, Eur. Phys. J. C **71** (2011) 1554.

[151] K. Cranmer, G. Lewis, L. Moneta, A. Shibata, and W. Verkerke, *HistFactory: A tool for creating statistical models for use with RooFit and RooStats*, CERN-OPEN-2012-016, 2012, `https://cds.cern.ch/record/1456844`.

[152] L. Moneta et al., *The RooStats Project*, PoS ACAT **2010** (2010) 057.

[153] F. James and M. Roos, *A System for Function Minimization and Analysis of the Parameter Errors and Correlations*, Comput. Phys. Commun. **10** (1975) 343–367.

[154] J. H. Friedman, *Data Analysis Techniques for High Energy Particle Physics*, SLAC-176, 1974, `https://cds.cern.ch/record/695770`.

[155] R. Brun and F. Rademakers, *ROOT - An object oriented data analysis framework*, Nucl. Phys. A **389** (1997) 81–86.

[156] S. Frixione, P. Nason, and G. Ridolfi, *A positive-weight next-to-leading-order Monte Carlo for heavy flavour hadroproduction*, JHEP **09** (2007) 126.

[157] H. B. Hartanto, B. Jäger, L. Reina, and D. Wackeroth, *Higgs boson production in association with top quarks in the POWHEG BOX*, Phys. Rev. D **91** (2015) 094003.

[158] S. Alioli, P. Nason, C. Oleari, and E. Re, *NLO single-top production matched with shower in POWHEG: s- and t-channel contributions*, JHEP **09** (2009) 111.

[159] E. Re, *Single-top Wt-channel production matched with parton showers using the POWHEG method*, Eur. Phys. J. C **71** (2011) 1547.